Remote sensing of cloud properties and their effects on shortwave radiation

Vanda Cristina Pires Salgueiro

Tese apresentada à Universidade de Évora
para obtenção do Grau de Doutor em Ciências da Terra e do Espaço.
Especialidade: Física da Atmosfera e do Clima.

ORIENTADOR (A/ES): *Maria João Tavares da Costa*
Ana Maria Almeida e Silva

ÉVORA, FEVEREIRO 2018

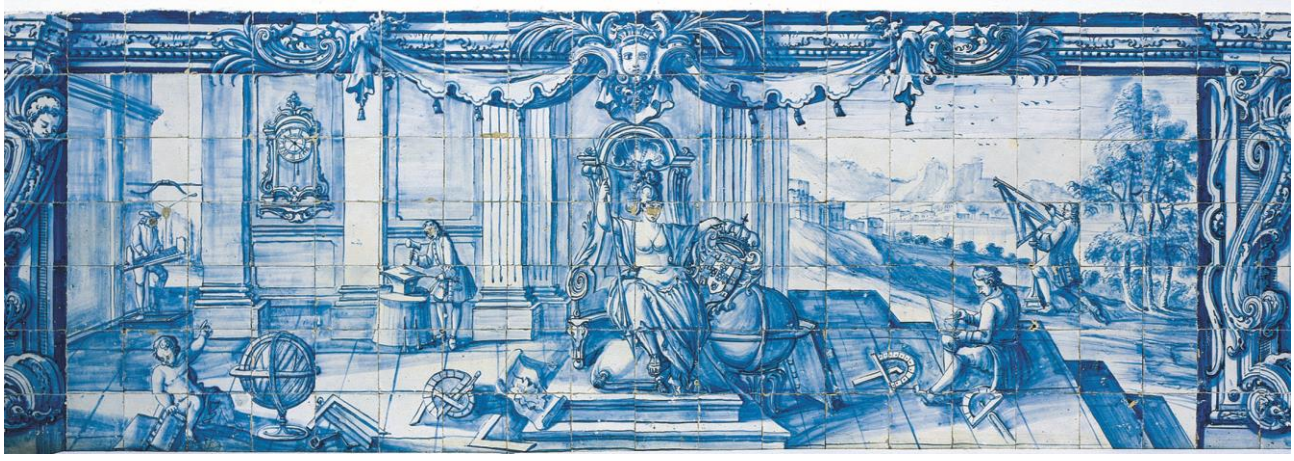

INSTITUTO DE INVESTIGAÇÃO E FORMAÇÃO AVANÇADA

Remote sensing of cloud properties and their effects on shortwave radiation

Vanda Cristina Pires Salgueiro

Tese apresentada à Universidade de Évora
para obtenção do Grau de Doutor em Ciências da Terra e do Espaço.
Especialidade: Física da Atmosfera e do Clima.

ORIENTADOR (A/ES): *Maria João Tavares da Costa*
Ana Maria Almeida e Silva

ÉVORA, FEVEREIRO 2018

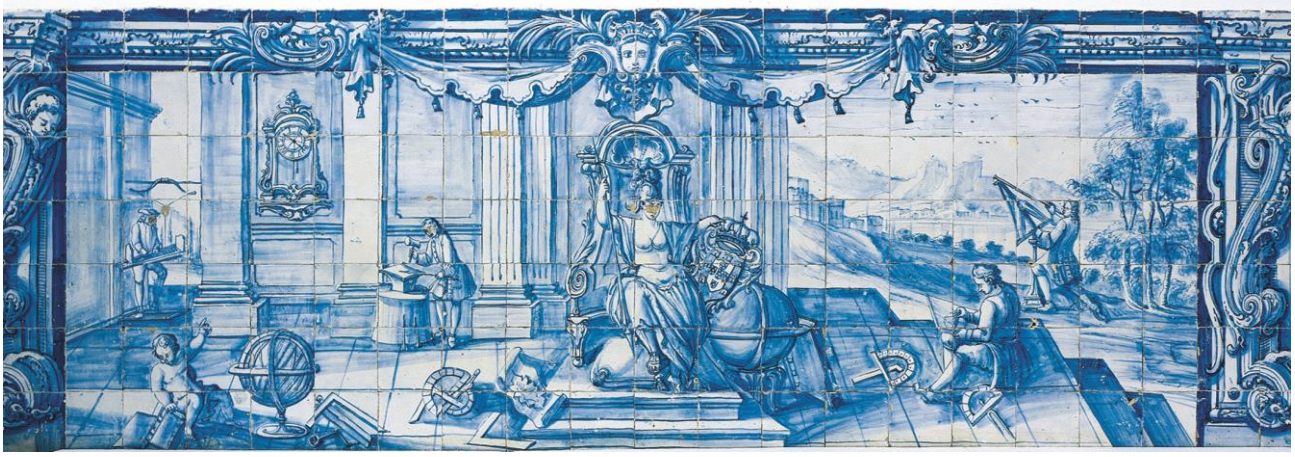

INSTITUTO DE INVESTIGAÇÃO E FORMAÇÃO AVANÇADA

À natureza que todos os dias nos presenteia com elementos tão belos como as nuvens, que nos fazem viajar apelando sempre à nossa imaginação, e a todos aqueles que a respeitam e que ajudam na sua conservação. Daqueles que trazem a natureza no coração, quero dedicar este trabalho especialmente ao meu irmão Hélio. Foi ele que me ensinou a não matar aranhas. Afinal, que mal é que elas nos fizeram?

A todos, desejo sempre dias cheios de sol com o céu salpicado de nuvens para que a monotonia seja uma inconstante na vida.

ACKNOWLEDGMENTS

First, I would like to thank to my supervisors Maria João Costa and Ana Maria Silva. Maria João for her teachings, help and support in doing this thesis during these last four years. She always advised and gave me good opportunities to meet, learn and work with other groups, and for all this I'm thankful to her. Ana Maria Silva was the first teacher that I met at the University of Évora, and was she that introduced me to the atmosphere group and invited me to be part of it. So, thank you to have shown me this path.

I would like to thank to Christine Chiu that welcome me at the University of Reading, for her teachings, given advices, and opportunities to meet other groups during my stay in Reading. I also acknowledge the University of Reading for the provided hosting facilities during my stay there.

My thanks go also to Christian Lanconelli for his contributions for the published paper on the International Journal of Remote Sensing.

I would also to thank to my colleagues of ICT team that contribute for my work. Ana Domingues that encouraged me to take part of ERCA2015, and for this experience I'm thankful to her. Thanks go too for my office colleagues, for their good mood, and for the briefings (hope next winter brings more rain to us and nice weather systems to follow). My thanks go too professor Rui Salgado, for the pressure that he made to finish this thesis by 4 August 2017. With a small delay, I "finished" it by 7 August.

Lastly, I would like to thank to my brother Hélio and my mother for their support and encouragement to finish this work.

I also acknowledge the funding provided by the FCT (the Portuguese Science and Technology Foundation) through the grant SFRH/BD/88669/2012. The work was co-funded by the European Union through the European Regional Development Fund, included in the COMPETE 2020 (Operational Program Competitiveness and Internationalization) through the ICT project (UID / GEO / 04683/2013) with the referencePOCI-01-0145-FEDER-007690**.**

TABLE OF CONTENTS

RESUMO

Deteção remota de propriedades de nuvens e os seus efeitos na radiação solar

As nuvens são os principais reguladores da quantidade de radiação solar que atinge a superfície terrestre, e esta quantidade de radiação depende das suas propriedades tais como o raio efetivo e a espessura ótica. Por outro lado, as propriedades das nuvens podem sofrer alterações devido a variações nas quantidades de aerossóis levando a alterações dos efeitos radiativos das nuvens. Deste modo, o trabalho desenvolvido nesta tese visa o estudo dos efeitos radiativos das nuvens na radiação solar à superfície, e a determinação das propriedades das nuvens e das interações aerossol-nuvem utilizando diferentes métodos de deteção remota. A variabilidade sazonal dos valores médios diários dos efeitos radiativos das nuvens na radiação solar foi analisada para sete anos (2003 – 2010) de dados medidos em Évora, tendo sido encontrada uma maior variabilidade durante a primavera quando a variabilidade dos períodos de nuvens é também maior. Para o mesmo período (2003 – 2010), a espessura ótica das nuvens de água líquida foi determinada a partir de medições feitas à superfície, e foi relacionada com os efeitos radiativos correspondentes. Posteriormente, estabeleceu-se um método para determinar a espessura ótica e o raio efetivo das nuvens, baseado em reflectâncias medidas pelo SEVIRI no visível e no infravermelho próximo. As propriedades das nuvens obtidas a partir do SEVIRI sobre a região de Évora foram também relacionadas com os efeitos radiativos das nuvens à superfície para o ano 2015, e para um caso de estudo de eventos de efeitos radiativos positivos das nuvens na radiação solar. Finalmente, foi aplicado um método baseado em medições de Lidar para determinar a espessura ótica das nuvens, a qual foi utilizada para estimar a concentração de gotículas de nuvem e o raio efetivo. Estas propriedades das nuvens foram usadas para avaliar as interações aerossol-nuvem de nuvens de água líquida não precipitantes nos Açores.

SUMMARY

Clouds are the main controllers of the amount of solar radiation that reaches the Earth's surface, and this amount of radiation depends on cloud properties such as the cloud effective radius and the cloud optical thickness. On the other hand, cloud properties may change due to changes in aerosol amounts leading to changes in cloud radiative effects. Thus, the work developed in this thesis aims to study the shortwave cloud radiative effects at the surface, and to determine the cloud properties and the aerosol-cloud interactions using different remote sensing methods. The seasonal variability of the daily-mean shortwave cloud radiative effects was analysed for seven years (2003 – 2010) of measured data in Évora, and a greater variability of the radiative effects was found for springtime when the variability of cloud periods is larger. For the same period (2003 – 2010), the cloud optical thickness was retrieved from ground-based measurements and it was related to the corresponding cloud radiative effects. After, a method to retrieve the cloud thickness depth and the effective radius was established using SEVIRI measured reflectances at visible and near infrared wavelengths. The satellite retrievals over Évora region were also related to the shortwave cloud radiative effects for year 2015, and for a case study with events of positive shortwave cloud radiative effects. Finally, a method based on Lidar signals was applied to retrieve the cloud optical thickness, which was used to estimate the cloud droplet number concentration and the effective radius. These cloud properties were used to evaluate the aerosol-cloud interactions of non-precipitating water clouds over Azores.

LIST OF PAPERS

This thesis includes the following published papers:

Salgueiro, V., M. J. Costa, A. M. Silva, C. Lanconelli, and D. Bortoli. 2017. "Cloud parameter retrievals from Meteosat and their effects on the shortwave radiation at the surface." *International Journal of Remote Sensing*, 38(4): 1137-1161. doi: 10.1080/01431161.2017.1280630

Salgueiro, V., M. J. Costa, A. M. Silva, and D. Bortoli. 2016. "Effects of clouds on the surface shortwave radiation at a rural inland mid-latitude site." *Atmospheric Research*, 178-179: 95-101. doi: 10.1016/j.atmosres.2016.03.020.

Salgueiro, V., M. J. Costa, A. M. Silva, and D. Bortoli. 2014. "Variability of the daily-mean shortwave cloud radiative forcing at the surface at a midlatitude site in Southwestern Europe." *Journal of Climate*, 27(20): 7769-7780. doi: 10.1175/JCLI-D-13-00696.1.

LIST OF FIGURES

LIST OF TABLES

LIST OF ACRONYMS

Chapter 1 – "Introduction" and chapter 6 – "Conclusions and final remarks":

ACI – Aerosol-cloud interactions;

AERONET – Aerosol Robotic Network;

COT – Cloud optical thickness;

CRE_x – Cloud radiative effects, where *x* may represent SW, LW and NET;

ECOT – Effective cloud optical thickness;

IR – Infrared;

LW – Longwave;

LWP – Liquid water path;

MFRSR – Multifilter Rotating Shadowband Radiometer;

$NCRE_{SW}$ - Normalized Shortwave Cloud Radiative Effects;

NIR – Near infrared

SEVIRI - Spinning Enhanced Visible and Infrared Imager;

SW – Shortwave;

VIS – Visible;

Chapter 2 – "Variability of the daily-mean shortwave cloud radiative forcing at the surface at a midlatitude site in southwestern Europe":

AERONET – Aerosol Robotic Network;

AOT – Aerosol Optical Thickness;

CGE – Geophysics Centre of Évora;

COT – Cloud Optical Thickness;

CRF – Cloud radiative forcing;

CRF_{SW} – Shortwave Cloud Radiative Forcing;

LW – Longwave;

MFRSR – Multifilter Rotating Shadowband Radiometer;

$NCRF_{SW}$ – Normalized Shortwave Cloud Radiative Forcing;

PWV – Precipitable Water Vapor;

SW – Shortwave;

TOA – Top of the atmosphere;

Chapter 3 – "Effects of clouds on the surface shortwave radiation at a rural inland mid-latitude site":

AERONET – Aerosol Robotic Network;

COT – Cloud Optical Thickness;

CRE_{SW} – Shortwave Cloud Radiative Effects;

ECOT – Effective Cloud Optical Thickness;

ICT – Institute of Earth Sciences;

LUTs – Look-Up Tables;

LWC – Liquid Water Content;

MFRSR – Multifilter Rotating Shadowband Radiometer;

$NCRE_{SW}$ - Normalized Shortwave Cloud Radiative Effects;

SW – Shortwave;

Chapter 4 – "Cloud parameter retrievals from Meteosat and their effects on the shortwave radiation at the surface":

CMF –Cloud Modification Factor;

CM-SAF – Climate Monitoring Satellite Application Facility;

COT – Cloud Optical Thickness;

CPP – Cloud Physical Properties;

CPS – Cloud Properties from SEVIRI;

CRE_{SW} – Shortwave Cloud Radiative Effects;

CWP – Cloud Water Path;

F_{sc} – Fractional sky cover;

ICT – Institute of Earth Sciences;

IR – Infrared;

IWP – Ice Water Path;

LWP – Liquid Water Path;

LUTs – Look-Up Tables;

NIR – Near-infrared;

SEVIRI – Spinning Enhanced Visible and Infrared Imager;

SW – Shortwave;

TOA – Top of the Atmosphere

VIS – Visible;

Chapter 5 – "Warm cloud and aerosol properties over Azores":

ACI – Aerosol-cloud interactions;

ARM - Atmospheric Radiation Measurement;

COD_{MPL} – Cloud optical depth from MPL;

COD_{MFRSR} - Cloud optical depth from MFRSR;

ENA - Eastern North Atlantic;

LWP – Liquid water path;

MPL – Micropulse Lidar;

MFRSR – Multifilter rotating shadowband radiometer;

LIST OF SYMBOLS

Chapter 2 – "Variability of the daily-mean shortwave cloud radiative forcing at the surface at a midlatitude site in southwestern Europe":

$F_{\downarrow}^{cs}$ – Downwelling shortwave irradiance for clear-sky;

$F_{\downarrow}^{cld}$ – Downwelling shortwave irradiance for cloudy sky;

$F_{\uparrow}^{cs}$ – Upwelling shortwave irradiance for clear-sky;

$F_{\uparrow}^{cld}$ – Upwelling shortwave irradiance for cloudy sky;

θ – Solar zenith angle;

α – Surface albedo;

Chapter 3 – "Effects of clouds on the surface shortwave radiation at a rural inland mid-latitude site":

$F_{\downarrow}^{cs}$ – Downwelling shortwave irradiance for clear-sky;

$F_{\downarrow}^{cld}$ – Downwelling shortwave irradiance for cloudy sky;

α – Surface albedo;

ρ – Water density;

r_e – Effective radius;

Δz – cloud geometrical thickness;

τ – Cloud optical thickness;

Chapter 4 – "Cloud parameter retrievals from Meteosat and their effects on the shortwave radiation at the surface":

r_e – Cloud effective radius/particle size;

θ – Satellite zenith angle;

θ_0 – Solar zenith angle;

$\Delta\varphi$ – Relative azimuth angle;

$I_{3.9}$ – Total upward radiance at 3.9 μm;

$r_{3.9}$ – Cloud reflectance at 3.9 μm;

F_0 – Extra-terrestrial solar flux;

μ_0 – Cosine of the solar zenith angle;

$B_{3.9}$ – Thermal radiance (Planck function) at 3.9 μm;

T – Temperature;

$\tau_{3.9}^{0}$ - Total transmission of sunlight above the cloud;

$\tau_{3.9}'$ - Upward transmission of thermal radiation above the cloud;

ρ – Water density;

$F_{cs}^{\downarrow}$ – Downwelling shortwave irradiance for clear-sky;

$F_{cld}^{\downarrow}$ – Downwelling shortwave irradiance for cloudy sky;

α – Surface albedo;

Chapter 5 – "Warm cloud and aerosol properties over Azores":

r_e – Cloud effective radius;

σ_s - Aerosol scattering coefficient;

α – Aerosol proxy;

N_d – Cloud droplet number concentration;

N_{CCN} – Cloud condensation nuclei concentration;

ρ_w – Water density;

1 INTRODUCTION

1.1 State-of-the-art

Clouds on a given day cover about two thirds of the planet, playing a main role in the Earth's climate system. They determine the Earth's radiation budget and they are the main controllers of the hydrological cycle. The mid-latitude oceanic storm tracks and tropical precipitation belts are the regions with more clouds, while continental desert regions and central subtropical oceans are relatively cloud-free. Clouds may appear in a cellular appearance (cumuliform) or in sheets (stratiform) in a stable atmosphere, and they may extend from near the surface to the upper troposphere in an unstable atmosphere. Depending on their position in the atmosphere, they may be composed of liquid water, ice, or a mixture of both phases interacting with solar and terrestrial radiation differently. The effects of clouds on solar or shortwave (SW; 0.2 to 5.0 μm) radiation (CRE_{SW}) can be examined by the difference between clear-sky and cloudy-sky radiation fluxes (Ramanathan et al. 1989). Clouds reflect incoming SW radiation, which increases the planetary albedo contributing to cool the earth-atmosphere system. The earth-atmosphere system also accounts with the terrestrial or longwave (LW; 5.0 – 50.0 μm) cloud radiative effects (CRE_{LW}), which are estimated in a similar way as CRE_{SW}. CRE_{LW} produce a heating of the system due to the absorption and emission of LW radiation by clouds, which reduces the amount of LW flux that escapes to space by the system free of clouds. Despite the heating produced by CRE_{LW}, satellite estimates show that clouds exert a net global mean radiative effect ($CRE_{NET} = CRE_{LW} + CRE_{SW}$) at the top of the atmosphere -20 W m^{-2} implying a net cooling effect of clouds on the current climate, and with most negative CRE_{NET} in regions of very extensive low-lying reflective stratus and stratocumulus clouds such as midlatitude and eastern subtropical oceans (Boucher et al. 2013).

The role of clouds on the Earth's radiative balance was recognized a long time ago. Ramanathan et al. (1989) and Harrison et al. (1990) were among the first to estimate the cloud radiative effects (CRE_{SW} and CRE_{LW}) and its seasonal variation from satellite data. Since then, the cloud radiative effects (CRE) have been quantified by different studies (e.g. Dong et al. 2006; Berg et al. 2011; Oreopoulos and Rossow 2011; Allan 2011; Mateos et al. 2013; Salgueiro et al. 2014, 2016; Pyrina et al. 2015). These studies, using satellite observations (Oreopoulos and Rossow 2011), ground-based

measurements (Dong et al., 2006; Berg et al. 2011; Mateos et al. 2013; Salgueiro et al. 2014, 2016), and combining satellite observations with modelling (Allan 2011; Pyrina et al. 2015) allowed to analyse the seasonal and annual variability of CRE from local to global scales, and for different cloud conditions such as the type of clouds and its fractions. For example, Oreopoulos and Rossow (2011) used satellite data from the International Satellite Cloud Climatology Project [ICCP; Schiffer and Rossow (1983)] to investigate the CRE of various cloud regimes for three distinct areas covering most of the Earth's surface. Allan (2011) estimated a net cooling of the climate system of -21 W m^{-2} from data of the Geostationary Earth Radiation Budget (GERB) on-board Meteosat-9 and CERES satellites combined with numerical forecast model reanalysis. Pyrina et al. (2015) computed the CRE of the different cloud types (low, middle, high-level clouds, and total cloud cover) in the Mediterranean basin, concluding that the low-level clouds dominate the CRE_{SW} at the surface. This study by Pyrina et al. (2015) also showed that the CRE_{SW} (-43.7 W m^{-2}) at the surface controls the CRE_{NET} (-15.9 W m^{-2}) for all cloud types, and drives the seasonal variation of the CRE_{NET}. Dong et al. (2006) quantified the seasonal and annual cloud radiative effects (SW, LW and NET) due to the different cloudy conditions (all-sky, total clouds, single-layer low, middle, and high clouds) at a midlatitude site. They showed that low clouds have the largest impact on the CRE at the surface producing the LW warming (55 W m^{-2}) and the SW cooling (-91 W m^{-2}) effects with maximum values in spring season and minimum in summer. Salgueiro et al. (2014) also reported seasonal and annual values of CRE_{SW} for all-sky and total cloud conditions for a midlatitude site, with a larger variability of the CRE for the spring season. These studies show the important contribution of CRE_{SW} component for the net cooling effect produced by clouds.

CRE_{SW} depend on cloud properties such as the cloud optical thickness (COT), which is essential to determine how much incident SW radiation is extinct due to scattering and absorption by cloud particles. Changes in CRE_{SW} due to COT can be quantified by the CRE_{SW} efficiency defined as the CRE_{SW} per unit of COT (Mateos et al. 2014a). Salgueiro et al. (2016) related the CRE_{SW} efficiency for normalized CRE_{SW} with the corresponding COT of non-precipitating water clouds, having shown that the CRE_{SW} efficiency approach the unit for COT values larger than 50. Besides the cloud optical thickness, the CRE_{SW} at the surface are also function of other factors as for example the fractional sky cover. All-sky CRE_{SW} at the surface decreases with

increasing cloud fraction (Dong et al. 2006). Nevertheless, changes in cloud fraction affect the SW radiation at the surface by changing the direct solar beam and the amount of the diffuse radiation due to the multiple scattering. This may lead to enhancement events, which occur when the diffuse irradiance exceeds the corresponding instantaneous clear sky. Berg et al. (2011) evaluated the CRE at the surface for shallow cumulus, and they reported enhancements events responsible for positive CRE_{SW} with instantaneous values reaching 75 W m^{-2} caused by temporal and spatial inhomogeneities of cumulus. Mateos et al. (2013) related the CRE_{SW} with the fractional sky cover, reporting the likelihood of enhancement event occurrence according with the values of the hemispherical fractional sky cover and the fractional sky cover in the octant where the sun is placed. Piedehierro et al. (2014) investigated the enhancement events longer than 5 minutes of total SW irradiance at the surface, reporting an event with a durantion of 74 minutes. Salgueiro et al. (2017) reported values of cloud modification factor (ratio between measured SW irradiance under cloudy conditions and the same quantity estimated for clear-sky conditions) larger than 1 indicating the occurrence of enhancement events for different values of cloud fractions. Although, the enhancement events produce positive CRE_{SW}, they occur at a small temporal scale and the bulk CRE_{SW} leads to a cooling effect.

Changes in CRE_{SW} may also be caused by changes in cloud properties. The aerosol particles can act as cloud condensation nuclei upon which cloud droplets form. Changes in aerosol concentrations have the potential to modify the microphysical and the optical properties of the clouds, affecting the cloud reflectance (Twomey 1977), extension and lifetime (Albrecht 1989). Aerosol-cloud interactions carry the greatest uncertainty of all climate radiative forcing mechanisms as reported by the Intergovernmental Panel on Climate Change (IPCC) in their Fifth Assessment Report (AR5), producing a negative (cooling) effect on climate translated by a global mean effective radiative forcing of -0.45 W m^{-2} (Myhre et al. 2013). For this reason, the aerosol-cloud interactions (ACI) have been a subject of several studies (e.g. Feingold et al. 2001, 2003; McComiskey et al. 2009; Painemal et al. 2015, 2017), which are focused in low-level clouds such as stratus and stratocumulus clouds due to their impact on CRE (Dong et al. 2006; Boucher et al. 2013; Pyrina et al. 2015). ACI are associated with cloud microphysical responses due to changes in aerosol concentrations rather than radiative effects, and are expressed by a set of metrics (Feingold et al. 2001; McComiskey et al. 2009) that relate the cloud

microphysical properties (COT, effective radius, and cloud droplet number concentration) with proxies of the aerosol amounts (e.g. cloud condensation nuclei concentrations). Feingold et al. (2003) was the first that reported ACI results from ground-based remote sensing, analysing the response of the cloud effective radius to aerosols for seven cases study. McComiskey et al. (2009) used ground-based measurements to assess the ACI of non-precipitating coastal stratus clouds based on the response of the cloud optical thickness, effective radius, and cloud droplet number concentration to aerosols using different proxies (cloud condensation nuclei concentration, aerosol light scattering and aerosol index). They found ACI values of 0.48 with a R^2 of 0.14 suggesting that changes in aerosol amounts account for 14 % of the variability observed in the cloud droplet number concentration. This study by McComiskey et al. (2009) also addressed the ACI variability as a function of its natural drivers (e.g. aerosol size distribution and updraft velocity) and observational conditions. Studies like Painemal et al. (2015, 2017) also contribute to understand the ACI variability. Painemal et al. (2015) investigated the circulation patterns that modulate the synoptic and monthly variability of cloud condensation nuclei in boundary layer, and Painemal et al. (2017) estimate the ACI of marine low clouds for spring-summer season.

Remote sensing techniques are crucial to infer the properties and parameters that characterize the cloud field, and therefore to explain the radiative effects produced by clouds. Satellites constitute essential tools for clouds studies because they provide us a clear picture of the Earth, allowing to follow the cloud evolution over large areas. On the other hand, remote sensing techniques from ground-based measurements are capable to capture larger temporal variations in the cloud features than satellites, but at local scales where the instruments are installed. Thus, satellite and ground-based cloud remote sensing complement themselves. Remote sensing methods to infer the cloud properties (e.g. cloud optical thickness, effective radius/particle size, cloud water path and thermodynamic phase) from satellite imagers tend to rely on infrared (IR) or on a combination of visible (VIS) and near-infrared (NIR) measurements. The methods that use measurements at IR wavelengths are based on information from thermal emission of the clouds, whereas VIS/NIR methods are based on reflection of solar radiation by clouds. The Spinning Enhanced Visible and Infrared Imager (SEVIRI) (Schmetz et al. 2002) on board the geostationary Meteosat satellites and the Moderate Resolution

Imaging Spectroradiometer (MODIS) on board Terra and Aqua satellites on polar orbits are passive sensors, which provide measurements in VIS, NIR and IR spectral bands, essential for cloud characterization. Data from these two sensors are nowadays used by different algorithms (Baum and Platnick 2006; Roebeling et al. 2006) that allow to obtain the cloud properties through the mentioned IR and VIS/NIR techniques. The Climate Monitoring Satellite Application Facility (CM-SAF) (Schulz et al. 2009) of the European Organization for the Exploitation of Meteorological Satellites (EUMETSAT) provides data like the Cloud Property Data Set (Stengel et al. 2014), which uses the algorithm by Roebeling et al. (2006) to derive the cloud properties from SEVIRI observations. The algorithm by Roebeling et al. (2006) is based on the Nakajima and King (1990) approach, which uses reflectances at VIS and NIR wavelengths to retrieve simultaneously the COT and the cloud effective radius (r_e). The algorithm by Baum and Platnick (2006) also uses VIS/NIR techniques for COT and r_e retrievals, combining a non-absorbing band (0.6, 0.8 or 1.2 µm) with three longer wavelength bands where there is absorption (1.6, 2.1 and 3.7 µm). MODIS cloud products based on Baum and Platnick (2006) retrieval algorithm are made available by NASA Goddard Earth Sciences Distributed Active Archive Centre.

Remote sensing methods from ground-based measurements are also used to obtain the cloud properties (e.g. cloud optical thickness, effective radius, liquid water path, cloud base height, and cloud fractional cover). Cloud properties like liquid water path, cloud base height or cloud fractional cover may be obtained directly from the measurements performed by the different instruments. For example, the Vaisala ceilometer allows to obtain the cloud base heights from the time needed for a pulse of light to cross the atmosphere from the transmitter of the ceilometer to a backscattering cloud base and back to the receiver of the ceilometer. Another example is the sky-camera, which collects images of the cloudy conditions in the hemispherical field-of-view. The liquid water path may be obtained directly from microwave radiometer measurements, and if combined with COT it allows to estimate the cloud effective radius and the cloud droplet number concentration using the approaches by Stephens (1978) and by McComiskey et al. (2009), respectively. One of the most popular methods to retrieve the COT from ground-based measurements was proposed by Min and Harrison (1996). This method is based on measurements of the SW irradiance at 415 nm from the Multifilter Rotating Shadowband Radiometer (MFRSR), and it was

used several times in comparisons with other methods for COT retrievals (e.g. Chiu et al. 2006, 2014). Chiu et al. (2006) proposed a method to derive simultaneously the COT and the effective cloud fraction over vegetated surfaces from measurements of zenith radiances at 673 nm and at 870 nm. The principle of this method is the spectral contrast in the surface reflectances at these two wavelengths, since most of the vegetated surfaces are brighter at 870 nm than at 670 nm and the cloud properties are nearly identical in this wavelength region. Later, Chiu et al. (2010) presented a very similar method to infer the COT from AERONET (Aerosol Robotic Network) (Holben et al. 1998) cloud mode observations. AERONET is a global ground-based network designed to measure the microphysical and optical properties of the aerosols. Cloud mode observations are taken when clouds completely block the Sun making the measurements inappropriate to retrieve aerosol optical properties. Chiu et al. (2007, 2014) proposed another method for COT retrievals of water clouds, which is based on Lidar solar background signals combined with radiative transfer calculations. This method uses AERONET radiance measurements to calibrate the Lidar signals and outputs two COT values (one for thin and another for thick clouds), which are selected using the Lidar attenuated backscatter signal from cloud tops to 1 km above.

1.2 Motivation and research objectives

As mentioned before, clouds play a prominent role in the radiative balance, and therefore in determining the SW radiation fluxes that reach the surface. Évora is a small town having around 50.000 inhabitants located in a rural inland midlatitude almost flat site (38.5º N, 7.9º W), about 100 km east from the Atlantic Ocean. Due to its geographic location, Évora offers suitable conditions for cloud studies because it is on the track of frontal systems moving from the Atlantic Ocean, typically in winter and spring seasons, and because the solar radiation is highly available during all the year. On the other hand, the investigation on cloud characterization and on the SW cloud radiative effects for Évora site was limited. These reasons have motivated the author of this thesis to investigate the properties of the clouds over Évora by using different remote sensing methods and observations available at the site, and to determine its SW radiative effects at the surface. Additionally, the pristine conditions over the Azores and the availability of a wide set of different aerosol and cloud data motivated at a later stage of this thesis an exploratory work on aerosol-cloud interactions that will continue beyond this thesis.

Therefore, the overall objectives of this research are the study and the determination of the shortwave cloud radiative effects at the surface in Évora region, and the characterization of cloud properties and cloud-aerosol interactions using remote sensing methods based on Meteosat geostationary satellites and ground-based measurements. The cloud characterization consists of determining their microphysical and optical properties, essential to understand the SW cloud radiative effects.

The general objectives can be discriminated in the following specific objectives:

- Estimate the cloud radiative effects at Évora site using time series of ground-based SW irradiance measurements, taken during the years 2003 – 2010, and perform the seasonal and monthly variability analysis of the SW cloud radiative effects for all sky conditions in terms of type and fraction from partially cloudy to overcast.
- Retrieve the cloud optical thickness from ground-based transmittance measurements, and analyse its seasonal variability. Investigate the relationship between the warm cloud optical thickness retrievals and the SW cloud radiative effects at the surface over Évora region.
- Implement a method based on SEVIRI measurements to retrieve the cloud optical thickness and the effective radius/particle size that characterize the cloud field over the Iberian Peninsula, taking advantage of the temporal resolution (15 min) of Meteosat satellites.
- Study the relation between cloud properties retrievals from satellite and the SW cloud radiative effects from ground-based measurements over Évora region during the year 2015.
- Apply a remote sensing method based on Lidar background signals to retrieve the cloud optical thickness, and investigate the aerosol-cloud interactions using the cloud retrievals and aerosol properties measurements taken at the Eastern North Atlantic (ENA) site, in Graciosa Island (Azores).

1.3 Structure of the thesis

To reach the objectives of this research, the structure of the thesis was organized as follows: in the first chapter, *Introduction*, a revision of the state-of-art on the cloud radiative effects and on the remote sensing of cloud properties and aerosol-cloud interactions is made. This chapter also presents the objectives and motivation of the

research that makes part of this thesis. In the second, third and fourth chapters, results of the SW cloud radiative effects at the surface in the Évora region are presented, which in chapters 3 and 4 are related with the corresponding cloud properties retrievals using remote sensing methods based on ground-based measurements (chapter 3) and on both satellite and ground-based measurements (chapter 4); in the fifth chapter the study of aerosol-cloud interactions in Graciosa island, located in North Atlantic is presented.

The second chapter, "*Variability of the Daily-Mean Shortwave Cloud Radiative Forcing at the Surface at a Midlatitude Site in Southwestern Europe"* is a transcription of the paper by Salgueiro et al. (2014). Here, a study of the SW cloud radiative effects at the surface based on 7 years of measurements at Évora site is presented. A method to estimate the clear sky irradiance alternative to the method of Long and Ackerman (2000) is also proposed. The cloud radiative effects are calculated for two different SW spectral ranges, and their seasonal variation is discussed and compared with another data set also for a mid-latitude site.

The third chapter, "*Effects of clouds on the surface shortwave radiation at a rural inland mid-latitude site"*, is a transcription of the paper by Salgueiro et al. (2016). Following the work presented in chapter 2, where the seasonal variability of the CRE_{SW} was analysed but without relating it to the cloud properties, this chapter presents the seasonal variability of the cloud optical thickness retrieved for the 7 years of data considered in chapter 2. The retrievals for non-precipitating water clouds are evaluated against the corresponding MODIS COT, and related to the CRE_{SW} and efficiency on a seasonal basis.

The fourth chapter, "*Cloud parameter retrievals from Meteosat and their effects on the shortwave radiation at the surface"*, is a transcription of the paper by Salgueiro et al. (2017). This chapter complements the work of chapter 3 where the cloud characterization was done from ground-based data and related to the CRE_{SW}. Here, a method based on SEVIRI reflectances at 0.6 and 3.9 μm channels to retrieve the cloud optical thickness and the effective radius/particle size is established. This method allows for monitoring the cloud evolution over a suitable area in Évora region with an adequate temporal resolution to relate the cloud properties with CRE_{SW} obtained from ground-based hemispherical measurements. In this way, the work on the calculation of CRE_{SW} and its relationship with cloud properties reported in the previous chapters is improved. Thus, besides the satellite remote sensing method used, this chapter presents results on

the CRE_{SW} at the surface and the cloud modification factor, which are related with the cloud property retrievals from satellite over Évora region during the year 2015. A case study is presented, and a closure between the LWP estimated from the satellite retrievals and the corresponding LWP from ground-based measurements is also made.

The work described in the fifth chapter, *Warm cloud and aerosol properties over Azores*, is not published yet and it allowed to apply a different remote sensing method from those used in chapters 3 and 4 for COT retrievals. Here, the remote sensing method is based on Micropulse Lidar solar background signals. The method is used to retrieve the cloud optical thickness over Graciosa Island during the years 2014 and 2015, and the retrievals are combined with the liquid water path measurements to estimate the cloud droplet number concentration and the effective radius. The cloud properties together with *in situ* measurements of aerosol properties are used to assess the aerosol-cloud interactions.

The sixth chapter summarizes the main conclusions of each chapter, and gives suggestions for future work to improve the knowledge on cloud characterization and aerosol-cloud interactions.

It is important to note that from chapter to chapter some acronyms and symbols representing a same variable may change because each chapter (2, 3 and 4) is a transcription of a paper and these were published in different journals. The same can happen in the remaining chapters. For example, in chapter 2, the CRF_{SW} represents the same quantity as CRE_{SW} in chapters 3, 4 and 6. To note also that the Geophysics Centre of Évora (CGE) is now termed Institute of Earth Sciences (ICT) due to changes in the national research system during the period of development of this thesis. Thus, the list of symbols and acronyms is given for each chapter.

2 VARIABILITY OF THE DAILY-MEAN SHORTWAVE CLOUD RADIATIVE FORCING AT THE SURFACE AT A MIDLATITUDE SITE IN SOUTHWESTERN EUROPE

This chapter is a transcription of the paper with the following reference[1]:

Salgueiro, V., M. J. Costa, A. M. Silva, and D. Bortoli. 2014. "Variability of the daily-mean shortwave cloud radiative forcing at the surface at a midlatitude site in Southwestern Europe." *Journal of Climate*, 27 (20): 7769-7780. doi: 10.1175/JCLI-D-13-00696.1.

Abstract

The shortwave cloud radiative forcing is calculated from surface measurements taken in Évora from 2003 to 2010, with a Multi-Filter Rotating Shadowband Radiometer (MFRSR) and with an Eppley Black & White pyranometer. A new approach to estimate the clear-sky irradiance based on radiative transfer calculations is also proposed.

The daily mean values of the cloud radiative forcing (absolute and normalized) as well as their monthly and seasonal variabilities are analysed. The study shows greater variability of radiative forcing during springtime, with respect to the other seasons. The mean daily cloudy periods have seasonal variation proportional to the seasonal variation of the cloud radiative forcing, with maximum values also occurring during springtime. The minimum values found for the daily mean cloud radiative forcing are -139.5 W m^{-2} and -198.4 W m^{-2} for MFRSR and Eppley data, respectively; the normalized values present about 40% of sample amplitude, both for MFRSR and Eppley. In addition, a quantitative relationship between the MFRSR and Eppley cloud radiative forcing applicable to other locations is proposed.

[1] The references are not transcribed here but presented at the end of the dissertation all together, in order to avoid repetitions.

2.1 Introduction

Clouds are very important elements in the Earth-Atmosphere radiative balance due to their role in the interaction with shortwave (SW) (or solar) and longwave (LW) (or thermal) radiation. On one hand, they reflect and absorb part of the incoming SW radiation; on the other hand, they absorb LW radiation, emitted from the earth's surface, and, in turn, reemit LW radiation back to the earth and to space. Thus, clouds are the dominant modulators of radiation both at the surface and at the top of the atmosphere (TOA) (Dong et al. 2006). A way of quantifying the cloud radiation effects at the surface and at the TOA is the cloud radiative forcing (CRF), which is defined as an instantaneous change in net total radiation (SW plus LW; in W m^{-2}) obtained under cloudy conditions and its clear-sky counterpart; CRF can produce a cooling (negative CRF) or a warming (positive CRF) effect on the Earth-Atmosphere system.

CRF has been a research topic over the last decades due to its importance in understanding the effects of clouds in the radiative balance, which control the Earth-Atmosphere temperature; Ramanathan et al. (1989) and Harrison et al. (1990) were the first to estimate the global CRF and the seasonal effects of clouds on the radiation budget from ERBE (Earth Radiation Budget Experiment) data. Since then, with the improvement of satellites, ground-based instruments, and radiative transfer and climate models, many other studies dedicated to the radiative effects of clouds were developed (Mace et al. 2006; Kassianov et al. 2011; Berg et al. 2011; Liu et al. 2011; Dong et al. 2006), both at the surface and at the TOA. The calculation of CRF at the surface can be done through ground-based observations, and the information gathered at different sites all over the globe constitutes valuable information for validation purposes. The description of the cloud effects on the surface radiation budget is a critical component for understanding the current climate and an important step towards simulating potential climate change (Dong et al. 2006).

In this work, the shortwave cloud radiative forcing (CRF_{SW}), defined as the difference between the SW net fluxes (downward minus upward SW fluxes) obtained under both all-sky and clear-sky conditions, is calculated from irradiance measurements taken at the surface in the Geophysics Centre of Évora, which is located in the south of Portugal, about 100 km east from the Atlantic coast. Studies on the shortwave radiative forcing in this region, both at the TOA and surface levels, have already been made but mostly using atmospheric modelling and concentrating on the radiative effect of

aerosols and of contaminated clouds by desert dust aerosols (Santos et al. 2008, 2013). However, no investigation of the cloud radiative effects in the shortwave spectral range has been done at the site using the long-time series of surface SW irradiance measurements taken during the period 2003-2010.

These studies can be extremely useful to validate satellite assessments of radiative forcing or model calculations, particularly over a region of potential interest that is affected by contrasting air masses (Raes et al. 2000), and thus offers opportunities for studying not only clouds, but also their interaction with aerosols from different origins. During the winter season, the large-scale atmospheric circulation in Portugal is primarily determined by the location and intensity of the Icelandic low. The area is on the track of front systems typical of midlatitude regions, brought from the Atlantic Ocean by the westerly circulation and carrying moist air. These fronts affect the region more often in winter and spring, before the polar front moves northwards. When this happens, the synoptic circulation becomes constrained by the Azores anticyclone (during late spring and summer), which transports dry warm air from north or northeast into the region and is associated with clear-sky conditions. Besides, in the warm season, the intense surface heating of inland regions results frequently in the development of a thermal low pressure system at the Iberia scale, with shallow convection originating mostly in the afternoon (Costa et al. 2010).

In this study, the CRF estimates are relative only to the SW spectral range and involve global SW irradiance measurements in two different spectral bands obtained for all cloudy sky conditions, in terms of cloud type and cloud fraction (from partially cloudy to overcast), taken from ground-based instruments. Other authors have studied the variations of CRF for several sky conditions and for specific types of clouds (Dong et al. 2006; Berg et al. 2011; Liu et al. 2011). Berg et al. (2011) found a shortwave CRF average value of -45.5 W m^{-2} for shallow cumuli; Dong et al. (2006) have studied the seasonal and monthly variations of CRF for a mid-latitude site and showed that CRF_{SW} at the surface exhibited minimum values in spring and had a spring seasonal average of -61.3 W m^{-2} for all sky conditions. This study also analyses the seasonal and monthly variability of the surface CRF_{SW} for all sky conditions over a midlatitude site in southwestern Europe, aiming to contribute to the understanding of the cloud impact on the Earth's radiation balance, which is important for climate and climate change studies (Ramanathan et al. 1989).

The next section describes the methodology as well as the data used to estimate the shortwave cloud radiative forcing at the ground surface. Section 2.3 presents the results of this study, and section 2.4 summarises the work and the main results.

2.2 Data and methodology

2.2.1 Instruments and data

The measurements used here are recorded with two field instruments, a multifilter rotating shadowband radiometer (MFRSR) (Harrison et al. 1994) and an Eppley black and white pyranometer, both operating since 2003 at the Atmospheric Physics Observatory of Geophysics Centre of Évora (CGE; 38º34'N, 7º54'W, 300 m above mean sea level). The MFRSR is an instrument that provides automatic measurements of global and diffuse components of the spectral and broadband hemispherical shortwave irradiances with a temporal sampling of 1 minute. It has seven channels, covering the visible and partly the near infrared spectral regions (415, 500, 615, 673, 870 and 940 nm), with 10 nm of bandwidth and a broadband channel (300 – 1100 nm), used in this study. The Eppley black and white pyranometer provides measurements of hemispherical shortwave global irradiances, corresponding to the spectral region between 285 and 2800 nm, with a temporal sampling of 1 minute and providing 10-minute averages. The instruments are regularly calibrated, and their uncertainties estimated in 5%.

MFRSR broadband irradiance measurements taken from August 2003 to August 2010 have considerable gaps within the period, as listed in Table 2.1. Only the periods where coincident shortwave irradiance measurements from both instruments occur are used in the study. These measurements cover all sky situations in terms of cloud type and cloud fraction. The two sets of data from the MFRSR and Eppley instruments are used because the spectral bands of the instruments cover different fractions of the solar radiation spectrum at the surface (the MFRSR broadband channel covers approximately 73.5%, and the Eppley pyranometer covers roughly 95%). This allows comparison of the SW cloud radiative forcing at the surface obtained with two different sets of observed data for the same time period, geographic location, and atmospheric conditions and allows us to estimate the relative contribution of the MFRSR forcing to the total forcing (Eppley).

Aerosol optical thickness (AOT) and precipitable water vapor (PWV) data obtained from direct sun measurements continuously taken at the observatory of the Évora Geophysics Centre as part of the Aerosol Robotic Network (AERONET) (Holben et al. 2001) are also used in the study, as explained in the next subsection.

TABLE 2.1 MFRSR data available in Évora (cells with X) for the period 2003-10.

Month / Year	2003	2004	2005	2006	2007	2008	2010
January		X		X		X	
February		X		X		X	
March		X		X		X	
April		X		X			X
May				X		X	X
June				X		X	X
July				X		X	X
August	X			X	X		X
September	X			X	X		
October	X				X		
November	X		X		X		
December	X		X		X		

2.2.2 Clear-sky irradiance

The calculation of the SW cloud radiative forcing, which is described in the next subsection, requires irradiance values for clear-sky conditions; these values are not possible to obtain from measurements during cloudy periods. Long and Ackerman (2000) proposed a method to identify and produce continuous estimates of clear-sky irradiance values at the surface based on the empirical fit of clear-sky irradiance functions using the cosine of the solar zenith angle as the independent variable. While this method provides very good estimates of clear-sky irradiance at the surface for the day of the fitting, it ignores changes in atmospheric variables, such as PWV and AOT, between clear-sky days and therefore may introduce errors in the clear-sky irradiance estimates. A different approach is proposed here, based on radiative transfer (RT) calculations. The clear-sky irradiances corresponding to each measurement are calculated using the Library for Radiative transfer (LibRadtran) package (Mayer and Kylling 2005), taking into account both the MFRSR and Eppley spectral response functions. The surface is considered as a Lambertian reflector, with an albedo value of 0.22 for Eppley simulations (http://snowdog.larc.nasa.gov) and 0.27 for MFRSR broadband channel simulations obtained from spectral reflectance ground-based

measurements with a portable spectroradiometer (described by Potes et al. 2012). A midlatitude type of atmospheric vertical profile for winter or summer (McClatchey et al. 1971) was considered, according to the season. PWV and AOT values of 15 kg m^{-2} and 0.1 were used, respectively, corresponding to the average of AERONET measurements for the 7-year period and therefore considered representative of the conditions over Évora. Aerosols are assumed to be described by the (Shettle 1989) default properties, with rural type aerosols in the boundary layer, background aerosols above 2 km, spring-summer or fall-winter conditions (according to the season), and 50 km visibility. The radiative transfer equation is numerically solved using the discrete ordinate method (Stamnes et al. 2000) with 16 quadrature angles.

As mentioned before, day to day variations of atmospheric variables, such as PWV and AOT, may induce considerable changes in the radiation field; thus, fixed amounts of these variables may represent a poor approximation to accurately model the clear-sky irradiance. The method proposed here introduces two conversion functions that account for these variations and constitute a fast and accurate correction to the clear-sky irradiances calculated with the radiative transfer model. The conversion functions are defined as:

$$CF(\theta, x) = \frac{F_{\downarrow}^{cs}(\theta, x)}{F_{\downarrow}^{cs}(\theta, x_0)} \qquad (2.1)$$

Where $F_{\downarrow}^{cs}$ is the downwelling shortwave irradiance at the surface, θ is the solar zenith angle, x is either the AOT or the PWV value and x_0 takes the value of 0.1 (for the AOT) or 15 kg m^{-2} (for the PWV). Tables of the conversion functions are calculated with LibRadtran, considering the above described conditions, and varying the solar zenith angle (ranging from 0º to 90º with steps of 1º) and the AOT or the PWV within limits deemed adequate for the site based on AERONET measurements. The values of AOT were varied between 0.01 and 1.5, with a step of 0.1 between 0.1 and 1.5. The PWV was varied between 1 and 50 kg m^{-2}, with a step of 5 kg m^{-2} between 5 and 50. These conversion functions are normalised to unity for an AOT of 0.1 and a PWV of 15 kg m^{-2}, respectively. Figure 2.1 shows the contour plots obtained for both instruments and atmospheric variables considered. It can be noted that the conversion functions take values greater than one when the AOT is lower than 0.1 or when the PWV is lower than

15 kg m^{-2} (values considered for the normalisation of the conversion functions). Above these limits, the conversion functions decrease with the increase of both quantities. It is also worth mentioning that the variation of the conversion functions is more pronounced at higher values of the solar zenith angle, when irradiances are already quite low and differences in the atmospheric variables become increasingly important because of the longer path that radiation must travel in the atmosphere to reach the surface.

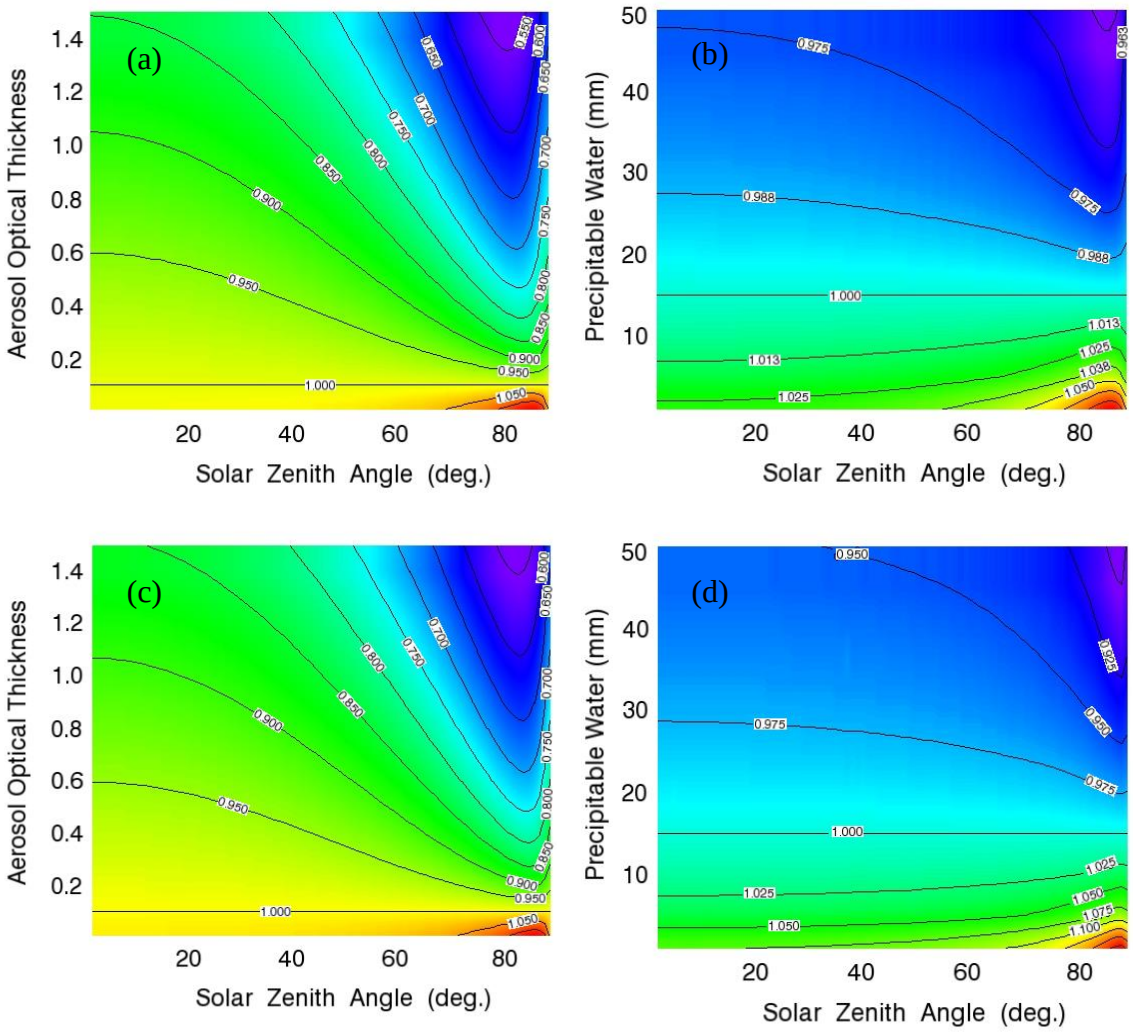

FIGURE 2.1 Conversion functions accounting for (a) AOT variations on MFRSR irradiances, (b) PWV variations on MFRSR irradiances, (c) AOT variations on Eppley irradiances, and (d) PWV variations on Eppley irradiances.

The clear-sky irradiance corrected to reflect the actual mean daily values of AOT and PWV $[F_{\downarrow}^{cs}(\theta)]$ is obtained from equation (2.2), using the conversion functions defined in equation (2.1). The conversion functions are obtained by linear interpolation

of the calculated tables using AERONET daily mean values of AOT and PWV for Évora site:

$$F_{\downarrow}^{cs}(\theta) = F_{\downarrow\,(AOT=0.1;PW=15)}^{cs}[CF(\theta, AOT)][CF(\theta, PW)] \qquad (2.2)$$

The irradiances obtained from equation (2.2) are compared to exact RT calculations considering the values of AOT and PWV represented by the conversion functions and spanning the values mentioned above in order to quantify the error involved in this approximation. Figure 2.2 shows the relative error as a function of the solar zenith angle, which is, in general, rather small and quite similar for MFRSR and Eppley spectral intervals. MFRSR presents slightly higher/lower extreme relative errors for lower zenith angles (grey dots in figure 2.2), which are obtained because absolute differences for MFRSR and Eppley simulations are roughly of the same order of magnitude, yet the clear-sky irradiance is higher for Eppley than for MFRSR (connected with the spectral range of each), yielding slightly higher relative errors in the latter case. For solar zenith angles lower than 70º, the relative error values are enclosed between -1.5% and 0.5%, increasing then with solar zenith angle to values between -3.5% and 3.0%. Note that the error distribution is biased towards negative values, indicating a slight tendency of the approximated clear-sky irradiance to underestimate the exact calculations. The overall mean bias errors (BIAS), root mean square error (RMSE), normalised BIAS (NBIAS) and normalized RMSE (NRMSE), as well as the number of data points used (*N*) and the correlation coefficient (*R*) are presented in table 2.2. The values obtained for the statistical parameters, with NBIAS of -0.05% and NRMSE of 0.1% in both cases, demonstrate the validity of the approximation expressed by equation (2.2).

TABLE 2.2 Statistics of the comparisons between exact radiative transfer calculations of clear-sky irradiance and the corresponding approximation using the conversion factors.

Case	BIAS (W m^{-2})	RMSE (W m^{-2})	NBIAS (%)	NRMSE (%)	*N*	*R*
MFRSR	-0.4	1.1	-0.05	0.1	4804	1.000
Eppley	-0.5	1.2	-0.05	0.1	4804	0.999

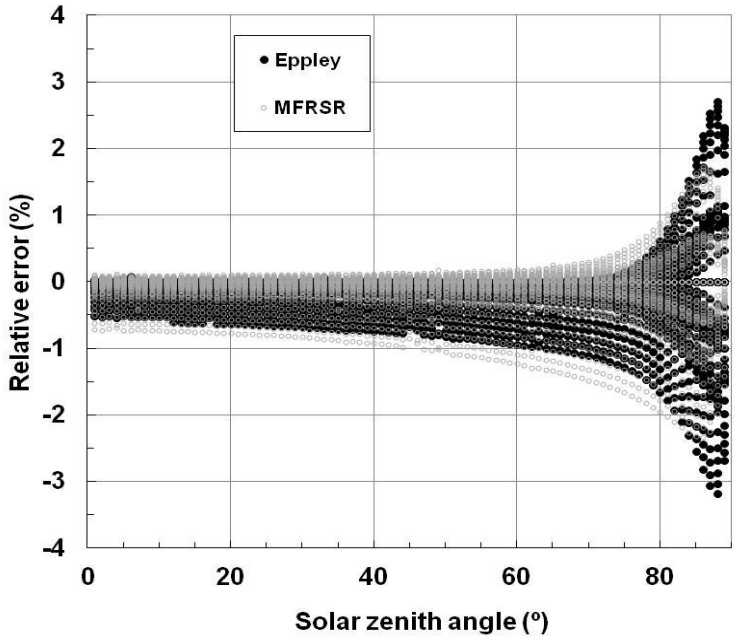

FIGURE 2.2 Relative error (%) associated with the solar irradiance calculation using the conversion factors, as a function of solar zenith angle.

The clear-sky irradiances obtained applying the described methodology are checked against clear-sky observations and are also compared to those obtained applying the method proposed by Long and Ackerman (2000). Figure 2.3 shows an example of the performance of the method for a case of moderately high values of AOT and PWV (0.47 and 24.6 kg m^{-2}, respectively) on 10 August 2010 for MFRSR and Eppley measurements. The clear-sky irradiance obtained from RT considering an AOT of 0.1 and PWV of 15 kg m^{-2} clearly overestimates the measurements; however, when the conversion factors are applied [equation (2.2)] accounting for the actual AOT and PWV values, a very good match between RT calculations and measurements is obtained in both cases, especially from around 10:00 UTC until the end of the day. Small differences between observations and RT calculations may also be due to variations in the AOT and PWV during the day, since daily averages are used to get the conversion factors for a certain solar zenith angle. The fit line obtained from the Long and Ackerman (2000) method also adjusts very well to the experimental points. However, this method requires a minimum number of clear-sky measurements over a considerable range of solar zenith angles to guarantee a statistically accurate calculation (Long and Ackerman 2000), which is not always available. Under cloudy conditions, the fits obtained with this method must be interpolated, introducing additional uncertainties in

the clear-sky irradiance. To compare the uncertainties introduced by the different methods, periods of at least four successive clear-sky days were selected from the complete dataset (2003-2010), in order to test the effect of the interpolation of the fit coefficients in a similar way to that followed by Long and Ackerman (2000), as well as to test the effect of the RT based methods. A total number of 64 days were found fulfilling the conditions mentioned before. Figure 2.4 shows the corresponding frequency histogram of relative differences between Eppley measured and estimated clear-sky irradiance using actually fitted coefficients (diagonal striped bars), interpolated coefficients (solid grey bars), RT calculations (solid black bars), and RT calculations combined with the conversion factors (checkered bars). Of the data obtained with the fitting method (Long and Ackerman 2000), 83% are within 3% of the clear-sky measurements, whereas, when the fitting coefficients are interpolated, only 58% of the data are within the same threshold (about the same percentage for the uncorrected RT method). The value increases to 70% when considering the method proposed here (RTM corrected). Similar results were obtained for the MFRSR data (plot not shown here) with 84% of the fitted clear-sky irradiances within 3% of the observations and 70% of the RT corrected irradiances within the same limit.

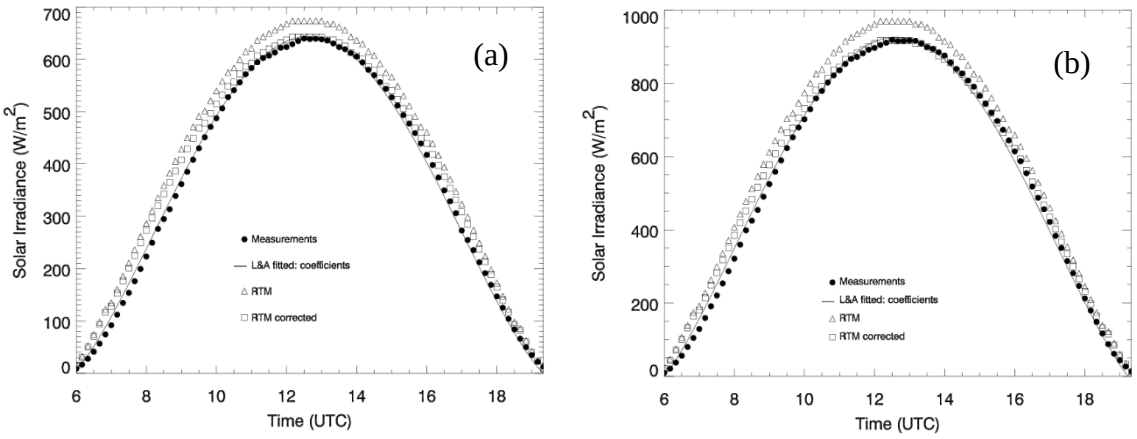

FIGURE 2.3 Global solar irradiance measurements (dots) and corresponding calculations using the Long and Ackerman (2000) method (line), the RT approach for fixed AOT and PWV values (triangles), and the RT approach combined with the conversion functions (squares) for 10 August 2010: (a) MFRSR and (b) Eppley.

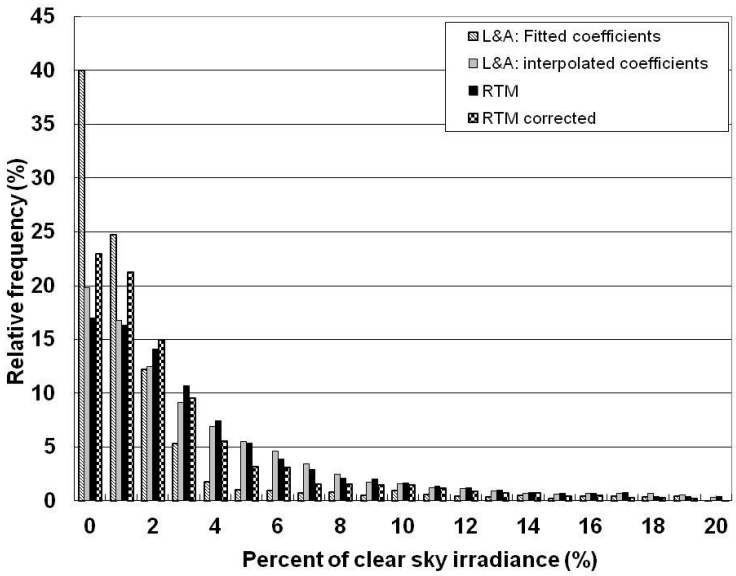

FIGURE 2.4 Frequency histogram of relative differences between Eppley 1-minute measured and estimated clear-sky irradiance using actually fitted coefficients (diagonal striped bars), interpolated coefficients (solid grey bars), RT calculations (solid black bars), and RT calculations combined with the conversion factors (checkered bars).

Although the fitting method presents the best performance (NRMSE of 2%), the proposed method constitutes a valid alternative (NRMSE of 3%), especially useful while clear-sky measurements are not available (preventing the use of the fitting method), as frequently happen during relatively long periods (more than 4 successive days) in autumn, winter and even springtime, when day to day changes in columnar aerosols and water vapour are also frequent. Since the main scope of this study is the analysis of the cloud radiative forcing at the surface, the clear-sky irradiance is estimated using the RT corrected method, which introduces an uncertainty of 3% (NRMSE), comparable to the uncertainty of the measurements (~5%).

2.2.3 Cloud radiative forcing

The shortwave cloud radiative forcing at the surface is defined as the instantaneous change in net [downwelling (↓) minus upwelling (↑)] shortwave irradiance (F) at the surface, due to changes in cloud conditions (type and/or cover). Negative values of CRF imply that less solar energy reaches the surface during cloudy conditions relative to the clear-sky ones, causing a cooling effect on the surface energy budget, and vice versa for positive cloud radiative forcing (Kassianov et al. 2011). The CRF_{SW}, in units of W m^{-2},

may be expressed by equation (2.3), where the superscripts "cld" and "cs" indicate cloudy and clear-sky, respectively. Considering that upward irradiance may be approximated by $\alpha F_{\downarrow}$, both for cloudy and clear-sky conditions, with α the albedo of the surface, the cloud radiative forcing may be rewritten as in equation (2.4).

$$CRF_{SW} = \left(F_{\downarrow}^{cld} - F_{\uparrow}^{cld}\right) - \left(F_{\downarrow}^{cs} - F_{\uparrow}^{cs}\right) \quad (2.3)$$

$$CRF_{SW} = (1-\alpha)\left(F_{\downarrow}^{cld} - F_{\downarrow}^{cs}\right) \quad (2.4)$$

It is necessary to know the surface albedo, as well as the downwelling surface irradiances in cloud and clear-sky conditions, with the latter taken as the reference to evaluate the irradiance change due to clouds. Surface albedo is probably slightly different for cloudy and clear-sky situations, but since this variation is not known precisely, the approximation adopted here is to consider the same surface albedo value, assuming that, to a first order, the variation of the surface albedo with cloud fraction has a minimal impact (Intrieri and Shupe 2004). This approach was also recently adopted by Mateos et al. (2013). A surface albedo of 0.22 is considered for Eppley simulations and 0.27 for MFRSR broadband channel simulations, as mentioned in the previous subsection. The cloudy downwelling surface irradiances are obtained from the MFRSR broadband measurements and from the Eppley measurements; the clear-sky irradiances are calculated with LibRadtran, as described in the above subsection.

It is sometimes useful to normalize the cloud radiative forcing, using the net irradiance for clear-sky conditions at surface (Sengupta et al. 2004) and thus eliminating the solar zenith angle and surface albedo dependence. As a result, the term (1-α) in equation (2.4), is eliminated, and the radiative forcing is only a function of the downwelling irradiances at the surface, as expressed in equation (2.5). The negative sign, in equation (2.5) is introduced to reflect the cooling effect of the SW cloud radiative forcing.

$$NCRF_{SW} = -\frac{\left(F_{\downarrow}^{cld} - F_{\downarrow}^{cs}\right)}{F_{\downarrow}^{cs}} \quad (2.5)$$

The normalized shortwave cloud radiative forcing ($NCRF_{SW}$) expresses the fraction of SW radiation that is attenuated by clouds through absorption or reflection and does not

reach the surface. If, in the limit, the $NCRF_{SW}$ assumes a value of zero, it means that clouds do not exert any effect on SW radiation (clear-sky conditions) and that the irradiance reaching the surface is the same with or without the presence of clouds $F_{\downarrow}^{cld} = F_{\downarrow}^{cs}$; the opposite situation ($NCRF_{SW}$ = 1) indicates that clouds would attenuate all the SW radiation $F_{\downarrow}^{cld} = 0$, which then would not reach the surface.

The (normalized) cloud radiative forcing calculated using the MFRSR broadband data and the Eppley pyranometer data are referred hereinafter as MFRSR (N)CRF_{SW} and as Eppley (N)CRF_{SW}, respectively.

2.3 Results and discussion

The CRF_{SW} as well the $NCRF_{SW}$ are calculated using data from the MFRSR broadband channel and from the Eppley pyranometer measurements [equation (2.4)], both corresponding to 10-minute averages. The results correspond to the whole period of measurements indicated in table 2.1 for all-sky conditions. Discarding the clear-sky periods, the data corresponds to a total of 28061 cloud occurrences (10-minute bins) in 963 days (240 in winter, 238 in spring, 251 in summer and 234 in autumn), considering all cloud situations in terms of type and fraction. The daily mean values of the CRF_{SW} and $NCRF_{SW}$ are calculated by integrating the 10-minute averaged values of CRF_{SW} and $NCRF_{SW}$ over the day (24 h) and dividing by this period, obtaining the all-sky CRF_{SW}. The cloudy periods, in hours per day, are also estimated from the 10-minute averaged data bins; those containing clouds (CRF_{SW}<0), in each day, are summed up to yield the cloudy period (in minutes), then converted to hours per day and averaged for all years of the study (2003-2010; table 2.1), for each season, and for each month. The use of this threshold to detect clouds constitutes a limitation with respect to enhancement events associated with broken cloud conditions (Piedehierro et al. 2014). These episodes exhibit CRF_{SW}>0, and thus, according to the classification adopted here, they are not considered cloudy, which may introduce additional uncertainty in the lower limits of the CRF statistics. Nevertheless, as the calculations are done using the 10-minute averages, the number of these enhancement events is expected to be small and the effect in the daily averages even smaller.

Overall CRF_{SW} results are represented in the probability distribution function (pdf) and cumulative distribution function (cdf) of figure 2.5 and correspond to the 963 days. MFRSR results are represented by the solid line and Eppley pyranometer values by the

dashed line. The distribution is clearly skewed to the left, with a long tail, reflecting in a few values with low daily mean CRF_{SW}, with the minimum MFRSR (Eppley) CRF_{SW} of -139.5 W m^{-2} (-198.4 W m^{-2}) and the median -18.9 W m^{-2} (-13.0 W m^{-2}). Yet, the interquartile range that contains 50% of the values is only 42.2 W m^{-2} (47.6 W m^{-2}), and the 10th and 90th percentiles are -73.1 and -2.0 W m^{-2} (-84.3 and -0.8 W m^{-2}), respectively, indicating a relatively low spread of the majority of the values in the sample. About 25% of the clouds exert a CRF_{SW} lower than -50 W m^{-2}, and only 3% (7%) present CRF_{SW} values lower than -100 W m^{-2}. Comparing the overall results obtained from MFRSR and Eppley data, only a minor change is observed in the central values; nevertheless, a great difference is obtained in the lower extreme, with a decrease from -139.5 W m^{-2} (MFRSR) to -198.4 W m^{-2} (Eppley).

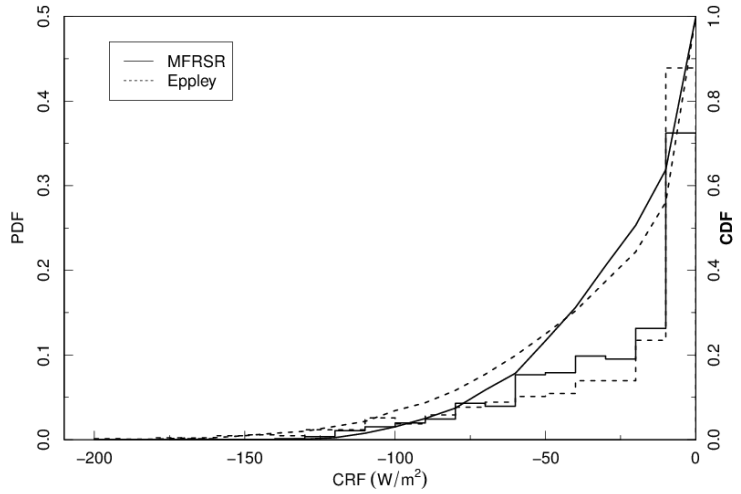

FIGURE 2.5 Pdf and cdf of MFRSR (solid line) and Eppley (dashed line) daily averaged CRF at Évora site during the 7-year period.

The monthly mean cloud periods, as well as the all-sky CRF_{SW} variability on a daily basis are shown in figure 2.6. Note that only days with at least one cloud occurrence (cloudy days) are represented (963 days in the 7-year period). A considerable spread of the daily mean CRF_{SW} and cloudy periods can be noted in March, April, and May. This indicates a large variability in springtime because of the large dispersion that occurs for all months of this season, with interquartile ranges of the MFRSR (Eppley) CRF_{SW} between 58.3 and 73.5 W m^{-2} (55.6 and 82.2 W m^{-2}) and relative errors of the daily mean cloudy periods ranging between 43 and 47%, hinting at a greater variability in the

sky conditions with respect to the other months. Autumn and winter months present very similar distributions and the cloudy periods present little variation. The summer season (June, July, and August) presents the lowest interquartile distance (MFRSR CRF_{SW}: 24.4 W m^{-2}; Eppley CRF_{SW}: 17.0 W m^{-2}) and the minima are -129.8 W m^{-2} (MFRSR CRF_{SW}) and -177.1 W m^{-2} (Eppley CRF_{SW}), which occur in the month of June. The cloudy periods represented in figure 2.6 (a) show higher variability (higher interquartile ranges) for the spring and autumn months than for winter and summer, when it scarcely varies, suggesting that these are transition months with highly variable conditions in terms of cloud occurrences. In fact, during the spring (autumn) season, the synoptic conditions are determined by the northerly (southerly) migration of the polar front, which determines the passage of Atlantic frontal systems over the area. On the other hand, in these seasons the region is sometimes affected also by northward drifts of the Azores anticyclone, which brings warm dry air into the region and is associated with clear-sky periods. The variability in the cloud occurrences originates from the occurrence of these synoptic patterns, as is typical of the transition seasons.

The all-sky daily CRF_{SW} is seasonally and annually averaged (considering also clear-sky days), and the results obtained using the Eppley measurements are compared with those reported by Dong et al. (2006) for another mid-latitude site. Seasonal and annual CRF_{SW} averages are also obtained under the conditions of total cloud, as described by Dong et al. (2006). The comparisons are summarized in table 2.3 and show, in general, similar CRF_{SW} annual cycles. The all-sky CRF_{SW} presents lower absolute values for this study, and the lowest CRF_{SW} values (more negative) are obtained for spring in both studies. Dong et al. (2006) estimate a springtime average CRF_{SW} for all sky conditions of -61.3 W m^{-2}, whereas in this study, the estimated mean value for the CRF_{SW} is -45.5 W m^{-2}. The annual average obtained here of -29.8 W m^{-2} is also lower (absolute value) than that estimated by Dong et al. (2006), who present a value of -41.5 W m^{-2}. As for the CRF_{SW} for total cloud conditions (also shown in table 2.3), it presents very similar results for both studies, with slightly more negative CRF_{SW} obtained here for winter and summer and slightly less negative values for spring and autumn, with respect to Dong et al. (2006). Overall total CRF_{SW} is very similar in both sites. The dissimilarities of all-sky CRF_{SW} and similarities of total CRF_{SW} also hint at the occurrence of more clear-sky days in Évora. Berg et al. (2011) reported a value of -45.5 W m^{-2} for summertime shallow cumuli, which is thus not directly comparable with

the CRF_{SW} obtained here. Mateos et al. (2013) also estimated the CRF_{SW} for another south Iberian site, obtaining average values of -78 W m^{-2} and -50.0 W m^{-2}, for solar zenith angles of 30º and 60º, respectively.

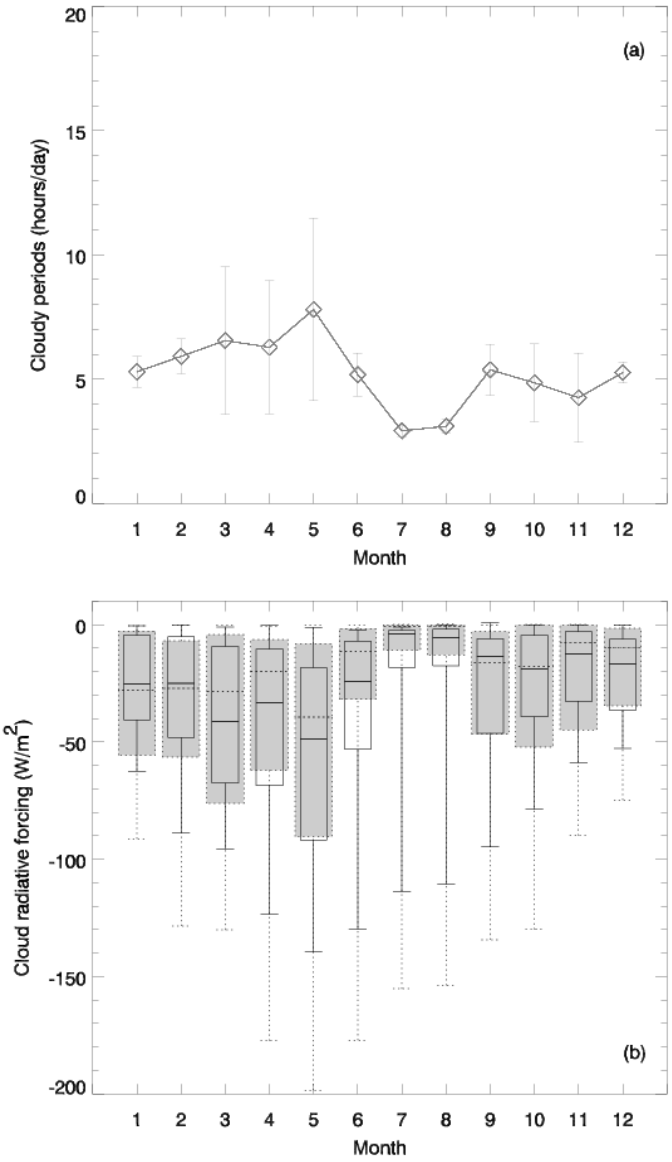

FIGURE 2.6 Box plots showing the monthly variation of the (a) mean cloudy periods and (b) daily mean MFRSR CRF_{SW} (black) and Eppley CRF_{SW} (dotted grey filled).

Figure 2.7 presents the pdf and cdf of the daily mean MFRSR $NCRF_{SW}$ and Eppley $NCRF_{SW}$. The median present moderately low values of 7.8% for the MFRSR $NCRF_{SW}$ and 4.2% for the Eppley $NCRF_{SW}$. The interquartile range of the MFRSR (Eppley) $NCRF_{SW}$ is 15.9% (13%) and the 10th and 90th percentiles are 0.8% and 26.5% (0.0% and 23.1%), respectively, indicating once again a relatively low variability of the

majority of the values in the sample. The distance between the 75th percentile and the maximum is quite large (MFRSR $NCRF_{SW}$: 22.8%; Eppley $NCRF_{SW}$: 26.8%), significantly higher than the interquartile range (MFRSR $NCRF_{SW}$: 15.9%; Eppley $NCRF_{SW}$: 13.0%); yet, according to the pdfs, the high extreme values presented in the sample are only a small number. In fact, barely 3% of the data presents a daily mean MFRSR $NCRF_{SW}$ above 30% and even less for the Eppley $NCRF_{SW}$. Eppley broadband decreases the variability of the central values by about 3% relative to MFRSR data; nevertheless, in terms of total variability, there is practically no change, with the maximum in both cases around 40%, similarly to Liu et al. (2011).

TABLE 2.3 Seasonal and annual averages of CRF_{SW} (all-sky and total cloud; W m^{-2}), where S denotes this study and D denotes Dong et al. (2006).

	Winter S/D	Spring S/D	Summer S/D	Autumn S/D	Annual S/D
All-sky	-26.6 / -34.0	-45.5 / -61.3	-18.8 / - 37.1	-28.4 / -33.4	-29.8 / -41.5
Total cloud	-56.2 / -54.1	-94.5 / -105.8	-80.8 / -75.0	-68.9 / -73.8	-75.1 / -77.2

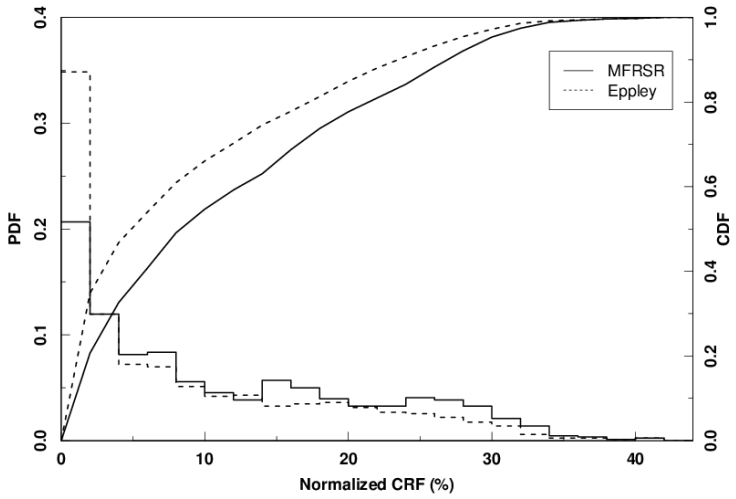

FIGURE 2.7 As in figure 2.5, but for the daily mean $NCRF_{SW}$.

The monthly variability of the daily mean MFRSR $NCRF_{SW}$ and Eppley $NCRF_{SW}$ is presented in figure 2.8. The season with the largest interquartile range of MFRSR (Eppley) $NCRF_{SW}$ is again spring with 19.7% (16.5%), contrasting with summer with only 7.6% (5.5%), which is probably related to the longest cloudy periods in spring (6.9

h day^{-1}) and the shortest in summer (3.6 h day^{-1}) [figure 2.6 (a)]. Nevertheless, in summer, the low variability in the central values oppose to the rather large upper extremes, which are as high as about 39.5% (originated in June). Autumn and winter present very similar distributions, skewed to the right, with moderately high upper whiskers (maxima of roughly 36% and 35%, respectively).

The daily mean surface CRF_{SW} results obtained from the MFRSR and Eppley measurements are different, basically because of the different spectral regions covered by each instrument (see section 2.2.1). These quantities are compared in order to determine a quantitative relationship relating to both CRFs, which may be applied to other locations where only one of the instruments is present or to modelled data. The minima Eppley CRF_{SW} values obtained each month (lower ends of the whiskers in the box plots of figure 2.6) exhibit a clear linear dependence on the minima MFRSR CRF_{SW}, with $CRF_{SW}^{Eppley} = 1.42 CRF_{SW}^{MFRSR}$ (R^2 = 0.97; NBIAS = 0.7%; NRMSE = 5%). Conversely, when all daily mean surface CRF_{SW} are considered (963 days), this dependence is no longer linear, being well described by a second-degree polynomial equation with a determination coefficient (R^2) of 0.87:

$$CRF_{SW}^{Eppley} = -0.0036 CRF_{SW}^{MFRSR\,2} + 0.83 CRF_{SW}^{MFRSR} \qquad (2.6)$$

When comparing the measured Eppley CRF_{SW} with that calculated with equation (2.6), the NBIAS is - 0.3%, indicating only a very slight tendency to underestimate the Eppley CRF_{SW}, and the NRMSE is 6% showing a low dispersion of the data. The reason for the nonlinearity in the previous relationship is related to the different response of the two spectral bands to different atmospheric conditions, increasing the dissimilarity between both as the cloud effect augments (lower CRF_{SW} corresponding to higher cloud optical thickness). As for the minima monthly CRF_{SW} relationship, these are likely representative of extreme cloudy conditions (highest cloud optical thickness each month), when most of the solar radiation at the surface is diffuse and isotropic; therefore, the cloud attenuation behaviour in both spectral regions (MFRSR and Eppley) is linearly related. The relationship proposed in equation (2.6) introduces only a low uncertainty (6%) and may constitute a useful tool to relate the CRF_{SW} in these spectral bands under any cloud conditions.

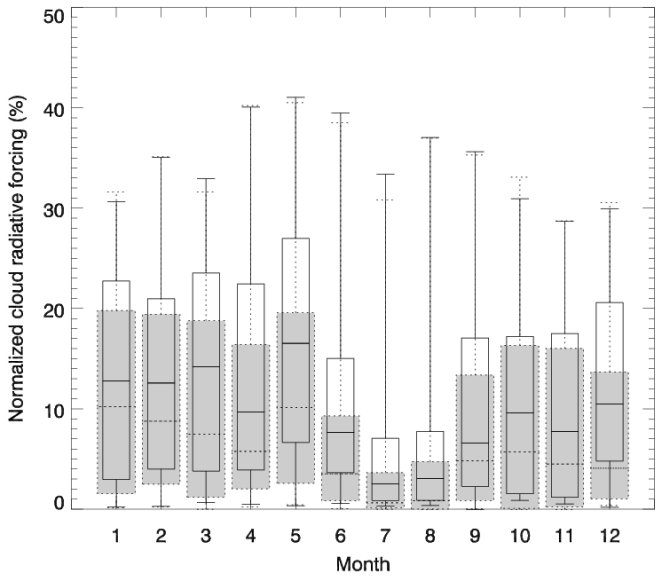

FIGURE 2.8 As in figure 2.6 (b), but for the monthly variation of the daily mean MFRSR $NCRF_{SW}$ (black) and Eppley $NCRF_{SW}$ (dotted grey filled).

2.4 Summary

The main purpose of this work was the calculation of the SW cloud radiative forcing at the surface, using surface irradiance measurements taken at a mid-latitude site (Évora), with a multifilter rotating shadowband radiometer (MFRSR CRF_{SW}) and an Eppley black and white pyranometer (Eppley CRF_{SW}), for all-sky situations in terms of cloud type and fraction. A new methodology to estimate the clear-sky irradiance is also proposed, based on the correction of the values obtained from radiative transfer calculations, using conversion functions to account for day to day atmospheric changes (aerosols and water vapor). It is shown that the clear-sky irradiances obtained in this way present a small uncertainty (~3%), constituting a fast tool to estimate this variable.

Overall results of CRF_{SW} show a large variability of the springtime values with respect to the other seasons and the lowest variability in summer for both absolute and normalized values; it is also in spring that the cloud occurrence presents the highest values and variability. Minimum values of -139.5 and -198.4 W m^{-2} for MFRSR CRF_{SW} and Eppley CRF_{SW}, respectively, were obtained considering the complete dataset (table 2.1). Yet for this dataset, it was found that the interquartile range (containing 50% of the values) is only 42.2 and 47.6 W m^{-2} for MFRSR CRF_{SW} and Eppley CRF_{SW}, respectively.

The $NCRF_{SW}$ presents an amplitude range of approximately 40%, considering the complete dataset (table 2.1). This implies that, in this study, clouds may attenuate (by absorption or scattering) up to about 40% of the solar radiation on a daily basis, or in other words, 40 % less solar radiation reaches the surface because of the cloud effects. Considering the $NCRF_{SW}$ results, the spring is the season with the largest variability, contrasted with summer, which presents the lowest variability, and probably this is related to the cloudy periods occurred in spring (6.9 h day^{-1}) and in summer (3.6 h day^{-1}). The same relation, between cloudy periods and CRF_{SW}, was verified showing that the variability of the cloudy periods is proportional to the variability of the cloud radiative forcing with its maximum value in springtime.

The use of two different instruments (MFRSR and Eppley) that cover different fractions of the solar radiation spectrum reveals some differences, with respect to the distributions of the daily mean CRF_{SW} and $NCRF_{SW}$. Curiously, there is only a minor change in the central values of the CRF_{SW} distributions, both from MFRSR and Eppley instruments; nevertheless, there is a strong decrease of the minimum value for the case where most of the solar radiation is included (Eppley). On the other hand, the total variability of the $NCRF_{SW}$ remains practically unchanged, both for MFRSR and Eppley instruments, although the variability of central values decreases by about 3% in the Eppley case. A mathematical equation is derived, expressing the relationship between the CRF_{SW} obtained in the two spectral bands, which may constitute a useful tool under any cloud conditions for different locations where only one of the instruments is present, or may even be applicable to modelled data.

Acknowledgements

This work is financed through FCT grant SFRH/BD/88669/2012 and through FEDER (Programa Operacional Factores de Competitividade – COMPETE) and National funding through FCT – Fundação para a Ciência e a Tecnologia in the framework of projects FCOMP-01-0124-FEDER-009303 (PTDC/CTE-ATM/102142/2008), FCOMP-01-0124-FEDER-014024 (PTDC/AAC-CLI/114031/2009) and provided by the Évora Geophysics Centre, Portugal, under the contract with FCT (the Portuguese Science and Technology Foundation), PEst-OE/CTE/UI0078/2014. The authors also acknowledge the project and support of the European Community - Research Infrastructure Action under the FP7 "Capacities" specific program for Integrating Activities, ACTRIS Grant

Agreement no. 262254. Thanks are due to Sérgio Pereira and Samuel Bárias for maintaining radiometric instrumentation used in this work.

The authors would like to thank the anonymous reviewers for their valuable comments and suggestions to improve the paper.

3 EFFECTS OF CLOUDS ON THE SURFACE SHORTWAVE RADIATION AT A RURAL INLAND MID-LATITUDE SITE

This chapter is a transcription of the paper with the following reference[2]:

Salgueiro, V., M. J. Costa, A. M. Silva, and D. Bortoli. 2016. "Effects of clouds on the surface shortwave radiation at a rural inland mid-latitude site." *Atmospheric Research*, 178-179: 95-101. doi: 10.1016/j.atmosres.2016.03.020.

Abstract

Seven years (2003- 2010) of measured shortwave (SW) irradiances were used to obtain estimates of the 10-minute averaged effective cloud optical thickness (ECOT) and of the shortwave cloud radiative effect (CRE_{SW}) at the surface in a mid-latitude site (Évora - south of Portugal), and its seasonal variability is presented. The ECOT, obtained using transmittance measurements at 415 nm, was compared with the correspondent MODIS cloud optical thickness (MODIS COT) for non-precipitating water clouds and cloud fractions higher than 0.25. This comparison showed that the ECOT represents well the cloud optical thickness over the study area. The CRE_{SW}, determined for two SW broadband ranges (300 – 1100 nm; 285 – 2800 nm), was normalized ($NCRE_{SW}$) and related with the obtained ECOT. A logarithmic relation between $NCRE_{SW}$ and ECOT was found for both SW ranges, presenting lower dispersion for overcast-sky situations than for partially cloudy-sky situations. The $NCRE_{SW}$ efficiency ($NCRE_{SW}$ per unit of ECOT) was also related with the ECOT for overcast-sky conditions. The relation found is parameterized by a power law function showing that $NCRE_{SW}$ efficiency decreases as the ECOT increases, approaching one for ECOT values higher than about 50.

[2] The references are not transcribed here but presented at the end of the dissertation all together, in order to avoid repetitions.

3.1 Introduction

The cloud optical thickness (column integrated extinction of radiation due to scattering and absorption by cloud particles) is an important cloud property in determining the amount of incoming shortwave (SW) solar radiation reaching the surface. Thus, the cloud optical thickness (COT) is critical to investigate the SW cloud radiative effects (CRE_{SW}) (Mateos et al. 2014a), which typically are described in terms of the difference between the clear sky and cloudy sky reflected solar fluxes (Ramanathan et al. 1989). The COT is also essential for any cloud radiation parameterization (Chiu et al. 2006), as well as for estimating the solar radiation available at the surface. Besides the COT, the CRE_{SW} depends on the season being determined by the insolation and cloud cover, and the seasonality of the net cloud radiative effect (shortwave plus longwave cloud effects) is driven by the SW cloud radiative effect (Pyrina et al. 2015). In this context, the study of the SW cloud radiative effects and their relation with cloud parameters and properties is essential to understand changes in solar fluxes due to clouds (Wacker et al. 2011; Pyrina et al. 2015; Song and Yum 2012).

Ground-based measurements represent a valuable source of information for cloud studies if gathered in different sites over the globe, for example for validation purposes. Different methods have been used to obtain the cloud optical thickness of different cloud types, using radiation from ground-based measurements (e.e. Min and Harrison 1996; Barker and Marshak 2001; Min et al. 2004; Chiu et al. 2006, 2010)]. Barker and Marshak (2001) and Chiu et al (2006; 2010) proposed retrieval methods based on the spectral contrast of the surface reflectance and used a combination of measurements at two wavelengths to derive the cloud optical thickness over vegetated surfaces. In particular, a family of retrieval algorithms has been proposed, making use of total, diffuse and direct irradiance measurements taken with a MultiFilter Rotating Shadow-band Radiometers (MFRSR) to infer the optical properties (cloud optical thickness and droplet effective radius) of warm clouds (Min and Harrison 1996) and the optical thickness of thin clouds (Min et al. 2004).

The aim of this work is to investigate the relation between the warm cloud optical thickness and the shortwave cloud radiative effects at the surface, in Évora, a city in the south of Portugal located about 100 km east from the Atlantic coast, representative of a rural inland midlatitude site. The cloud optical thickness is obtained using ground-based MFRSR global irradiance measurements at 415 nm considering all sky conditions from

broken clouds to overcast, being hereinafter referred as effective cloud optical thickness (ECOT) since it represents the total cloud optical thickness in the hemispheric field of view (FOV) of the instrument. Such quantity is relevant for the study of the CRE_{SW}, as well as for its efficiency (cloud radiative effect per unit of cloud optical thickness), which consents to propose simple parameterizations of the CRE_{SW} at the surface. CRE_{SW} assessment at this mid-latitude site (Évora) has already been made (Santos et al. 2008, 2013; Salgueiro et al. 2014), but without relating it with the cloud characterization. Santos et al. (2008, 2013) used atmospheric modelling to study the radiative effects of contaminated clouds by desert dust aerosols, whereas in Salgueiro et al (2014) the CRE_{SW} was evaluated using temporal series of surface SW irradiance measurements in two different SW spectral bands (300 – 1100 nm; 285 – 2800 nm). Thus, this work aims at contributing to the assessment of cloud optical thickness using ground based irradiance measurements, as well as to investigate the relation of the cloud optical thickness with the SW cloud radiative effect and efficiency of water clouds for the first time in Portugal, where solar radiation is an important natural resource highly available all around the year. In summary, this work constitutes a contribution to the investigation of cloud-radiation interaction in Portugal using for the first-time irradiance measurements from ground-based instrumentation.

The next section describes the data used in the study as well as the methodology; section 3.3 presents the results along with its discussion and finally in section 3.4 a short summary and the main conclusions are presented.

3.2 Methods and data

The experimental data used in this work (SW spectral and global irradiances) were obtained with a Multi-Filter Rotating Shadowband Radiometer (MFRSR) (Harrison et al. 1994; 6 narrow band channels centred at 415, 500, 615, 673, 870 and 940 nm and a broadband channel from 300 to 1100 nm) and an Eppley Black & White Pyranometer (broadband from 285 to 2800 nm). These instruments are installed at the atmospheric physics observatory of the Institute of the Earth Sciences (ICT; 38º34’N, 7º54’W, 293 m above mean sea level) located in Évora, south of Portugal, since 2003. The data used correspond to seven years of measurements, from 2003 until 2010. Both radiometers have a temporal sampling of 1 min used to provide 10 min averages and are regularly calibrated, with estimated instrumental errors of 5%. Since MFRSR and Eppley

instruments cover different fractions of the solar radiation spectrum at the surface (the MFRSR broadband channel covers approximately 73.5% and Eppley covers roughly 95%), the data by both instruments are used in calculations. This allows for the comparison of the SW cloud radiative effect and efficiency obtained with two different sets of SW observed data for the same time period, geographic location and atmospheric conditions.

3.2.1 Effective cloud optical thickness retrieval methodology

The methodology to retrieve the effective cloud optical thickness (ECOT) of water clouds is comparable to that described by Min and Harrison (1996) and later on validated by Min et al. (2004), which is based on MFRSR (fully described by Harrison et al. 1994) ground-based hemispherical SW transmittance measurements, at 415 nm, combined with 1D radiative transfer calculations. The spectral transmittance measurements are used instead of the directly measured SW spectral irradiances, which are highly dependent on the calibration accuracy. The Langley method is applied to selected days (clear sky stable and aerosol "free" conditions) in order to determine the top of the atmosphere irradiance, which is subsequently used to calculate the SW spectral transmittance values. These values are given by the ratio between the measured spectral irradiances under cloudy conditions and the top of the atmosphere spectral irradiance (Min and Harrison 1996). From the set of MFRSR channels (415, 500, 615, 673, 870 and 940 nm), the 415 nm channel is preferred over higher wavelengths, due to several reasons (Min and Harrison 1996): the surface albedo is lower at 415 nm than at higher wavelengths (e.g. 870 nm) and thus minimizes the cloud to ground interactions (Chiu et al. 2006); the O_3 Chappuis band is avoided, leaving only the weaker NO_2 absorption at 415 nm, whose correction represents a far lower error; the cloud optical thickness is less sensitive to changes of the droplet effective radius at lower wavelengths. Since cloud droplets fall onto the geometric optics regime for solar wavelengths, no spectral dependence is expected for the cloud optical thickness in this spectral range being, from this point of view, the wavelength choice irrelevant.

On the other hand, Look-Up Tables (LUTs), storing 415 nm MFRSR transmittance and cloud optical thickness values, are calculated using the 1D LibRadtran code Library for Radiative Transfer; Mayer and Kylling 2005). These LUTs are built for a selected grid of cloud optical thickness and solar zenith angles considering a thorough set of

plausible atmospheric conditions for a standard mid-latitude atmospheric profile comprising 50 levels between 0 and 120 km by Anderson et al. (1986), and taking into account the MFRSR spectral response function. The cloud optical thickness is varied between 1 and 100, with steps of 2 (values lower than 20), 3 (between 20 and 50) and 5 (between 50 and 100). The solar zenith angle is varied between 10º and 90º, with steps of 2º. The surface is considered as a Lambertian reflector with an albedo value of 0.04 and the aerosols, with an optical thickness of 0.1, are assumed to be described by the Shettle (1989) default properties with rural type aerosols in boundary layer, background aerosols above 2 km, and 50 km visibility. The values used for the aerosol optical thickness, surface albedo and precipitable water vapour (15 kg m^{-2}), correspond to the average of AERONET (Aerosol Robotic Network; Holben et al. 2001) measurements taken at the ICT observatory for the period considered in this work (2003-2010). Since there is no ancillary data providing information on the cloud phase, only water clouds are considered in the simulations, with a fixed cloud base height at 900 m and top height at 1100 m, obtained from a statistical analysis of four years of ceilometer measurements taken at the ICT observatory (Salgueiro 2011). An effective radius of 6 μm is used, based on a climatological distribution of low clouds (Liou 1992). In calculations, clouds are represented as homogeneous and plane-parallel layers with geometrical thickness of 200 m. The liquid water content [LWC; equation (3.1)] characterizing the cloud layer is calculated from the effective radius and optical thickness given as input parameters, and assuming cloud vertical homogeneity. In equation (3.1), ρ is the water density, r_e is the effective radius, τ is the cloud optical thickness and Δz is the cloud geometrical thickness. The water cloud particles, characterized by dimension r_e, are assumed as spheres and the conversion of microphysical to optical properties is done using pre-calculated Mie tables (available from http://www.libradtran.org).

$$LWC = \frac{2}{3}\frac{\rho r_e \tau}{\Delta z} \qquad (3.1)$$

The ECOT is then obtained by simple interpolation of the measured transmittance using the modelled transmittances contained in the LUTs. For each MFRSR measurement, the corresponding LUT (matching solar zenith angle and season) is used, yielding the corresponding interpolated ECOT value.

3.2.2 Shortwave cloud radiative effect calculations

The shortwave cloud radiative effect (CRE_{SW}; W m^{-2}) is determined using downward broadband global irradiance measurements (10-minute averages), recorded at the surface with the two field instruments described in the previous section: an Eppley pyranometer (285 - 2800 nm) and a MFRSR (300 – 1100 nm). All situations in terms of cloud cover and cloud type were considered to determine the CRE_{SW}, which is defined as the difference between the shortwave net surface fluxes [down ($F_{\downarrow}$) – up ($F_{\uparrow}$)] for all-sky and for clear-sky conditions. Over long-time averages or large spatial domains, the CRE_{SW} is always negative because clouds reflect more SW radiation than clear-sky, implying that less solar radiation reaches the surface. This produces a cooling effect, with its magnitude depending on the cloud optical properties and fraction, and varying with the season (Dong et al. 2006). CRE_{SW} can be expressed by equation (3.2) (Mateos et al. 2013; Salgueiro et al. 2014) considering that the upward irradiance ($F_{\uparrow}$) is approximated by $\alpha F_{\downarrow}$ both for all-sky ("cld") and clear-sky ("cs") conditions, where α is the surface albedo and $F_{\downarrow}$ the downward irradiance at the surface. The surface albedo α takes the values of 0.22 for Eppley (http://speclib.jpl.nasa.gov; last assessed in 2015/12/07) and 0.27 for MFRSR broadband channel, obtained from spectral reflectance ground based measurements with a portable spectroradiometer (described by Potes et al. 2012). Both albedo values are for all-sky and clear-sky conditions assuming that, to a first order, the variation of α with cloud fraction has a minimal impact (Intrieri and Shupe 2004). In order to eliminate the CRE_{SW} dependence on the surface albedo and on the solar zenith angle, this quantity is normalized using the net clear-sky irradiance (Sengupta et al. 2004) and as result the term (1-α), in equation (3.2), is eliminated. The normalized shortwave cloud radiative effect ($NCRE_{SW}$) is expressed in equation (3.3), where the negative sign is conveniently introduced to reflect the cooling effect of the CRE_{SW}.

$$CRE_{SW} = (1-\alpha)\left(F_{\downarrow}^{cld} - F_{\downarrow}^{cs}\right) \quad (3.2)$$

$$NCRE_{SW} = -\left(F_{\downarrow}^{cld} - F_{\downarrow}^{cs}\right)/F_{\downarrow}^{cs} \quad (3.3)$$

The downward broadband global irradiances in clear-sky conditions, taken as reference to evaluate the cloud effects, are calculated using the LibRadtran code since

these irradiance values are not possible to obtain from direct measurements during cloudy periods. The irradiance calculations are done for the same atmospheric conditions described in the previous section and taking into account both the Eppley and MFRSR broadband response functions. These calculated clear-sky irradiances at the surface are then corrected for variations in aerosol optical thickness and precipitable water vapour using the RT-method described by Salgueiro et al. (2014), which is an alternative method to Long and Ackerman (2000) that allows to identify and produce continuous clear-sky irradiance values at the surface. The 10-minute periods containing clouds are defined by $CRE_{SW} < 0$ and the positive CRE_{SW} is considered to be clear-sky. Although in case of enhancement events associated with broken clouds (Piedehierro et al. 2014) the CRE_{SW} can be greater than 0, and the applied threshold presents a limitation because these events are not considered as cloudy. Nevertheless, the number of these enhancement events is expected to have a small impact in the 10-minute samples considered with $CRE_{SW} < 0$ (Salgueiro et al. 2014).

3.3 Results and Discussion

The seasonal variability of ECOT, CRE_{SW} and $NCRE_{SW}$, obtained for the same time period, is represented in figures 3.1, 3.2 and 3.3, respectively. These results are based in the 10-minute measurement averages, corresponding to a total of 27932 cloud occurrences (10-minute periods when $CRE_{SW} < 0$) in 963 days between 2003 and 2010 for all cloudy sky situations in terms of type and fraction, spread over all seasons as indicated by the number of data (N) in figure 3.1. The overall results show that the majority of ECOT occurs for values lower than approximately 40 in all seasons (figure 3.1). Particularly, it is in summer that the highest number of occurrences, corresponding to lowest ECOT values, are registered comparatively to the other seasons (winter, spring and autumn), where the ECOT seems more spread in all variation range (1–100). This is in agreement with the ECOT seasonal mean values (figure 3.1) which vary between a minimum of 12.3 in summer to a maximum of 17 in winter. The spring and autumn seasons present similar ECOT mean values, but a slightly higher ECOT median (10.1) was obtained for the spring season. Although all seasons present a high number of occurrences for low ECOT (less than 10), most probably with higher errors, which can be associated to low cloud fractions, spring presents a slightly different distribution with respect to the others, with the highest frequency between 10 and 20. This

variability in ECOT values is related with the type of clouds occurring in each season, which are determined by the synoptic patterns typical of the mid latitude regions, where Évora site is located. Ramos et al. (2014) show that the cyclonic weather type in the Iberian Peninsula presents a maximum in spring with respect to the other seasons, and a minimum in summer. This weather type is typically associated with unsettled conditions, clouds and thunderstorms. The variability in cloud optical thickness together with the available solar radiation, in each season, determine the CRE_{SW} and $NCRE_{SW}$ at the surface (figures 3.2 and 3.3), explaining the extremely negative CRE_{SW} values obtained in the spring months (mean values of -168.6 W m^{-2} and -178.6 W m^{-2}), especially with respect to autumn (mean values of -127.3 W m^{-2} and -150.9 W m^{-2}), also a transition season. Overall results for the CRE_{SW} (figure 3.2) are in correspondence with ECOT, low number of occurrences of more negative CRE_{SW} correspond to less occurrence of high ECOT values. The highest CRE_{SW} occurrence is found in summer for CRE_{SW} > -50 W m^{-2}, corresponding to Eppley instrument, which is in accordance with highest number of occurrences of low ECOT values. This summer effect can be also observed for $NCRE_{SW}$ (Eppley instrument; figure 3.3), where the highest number of occurrences is observed for $NCRE_{SW}$ < 10% meaning that clouds have a low effect on SW radiation that reaches at the surface.

The obtained CRE_{SW} (figure 3.2) can be compared with studies in other sites. Mateos et al. (2013), using 1-minute data, obtained in Granada (Spain) mean values of -78 W m^{-2} and -50 W m^{-2} for solar zenith angles of 30º and 60º, respectively. Wacker et al. (2011) obtained shortwave cloud radiative effects between -167.4 W m^{-2} and -456.9 W m^{-2} around local noon for stratus conditions in the Payerne site (Switzerland). Berg et al (2011) obtained hourly average values of lower than -300 W m^{-2} for all periods with shallow cumuli in the United States. Also in the United States, Dong et al. (2006) obtained values around -250 W m^{-2} for total cloud around local noon and seasonal mean values between -54.1 W m^{-2} and -105.8 W m^{-2} in winter and summer seasons, respectively. Although clouds and time resolutions used in each study are different, the obtained CRE_{SW} seems to be in agreement with the previous studies.

Yet, due to the different ranges of the spectral bands (Eppley: 285 – 2800 nm; MFRSR: 300 – 1100 nm), the Eppley CRE_{SW} presents more negative values than the MFRSR CRE_{SW}. This effect is more pronounced in spring, a transition season characterized by a greater variation in cloudy periods (figure 2.6 (a) in previous

chapter). The different CRE_{SW} and $NCRE_{SW}$ occurrences between both instruments can be also explained by the different range of the spectral bands. The $NCRE_{SW}$, i.e. the CRE_{SW} without solar zenith angle effects, shows that in this study, clouds may attenuate up to 80% of SW radiation (figure 3.3) in all seasons.

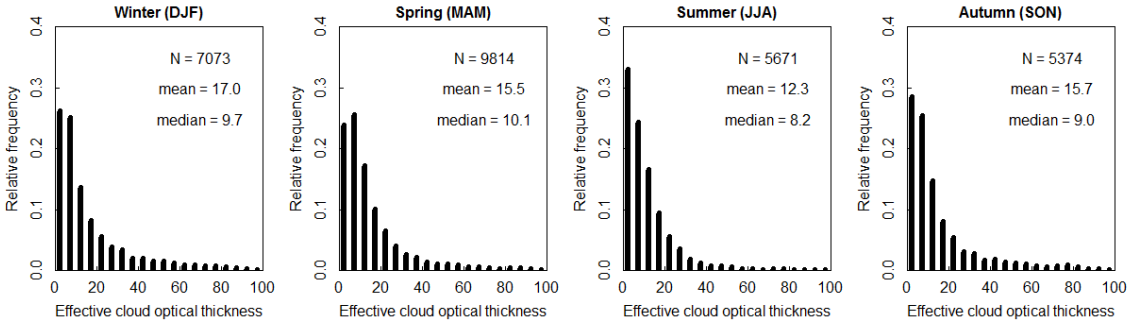

FIGURE 3.1 Seasonal variability of the effective cloud optical thickness; N is the number of cloud occurrences in each season.

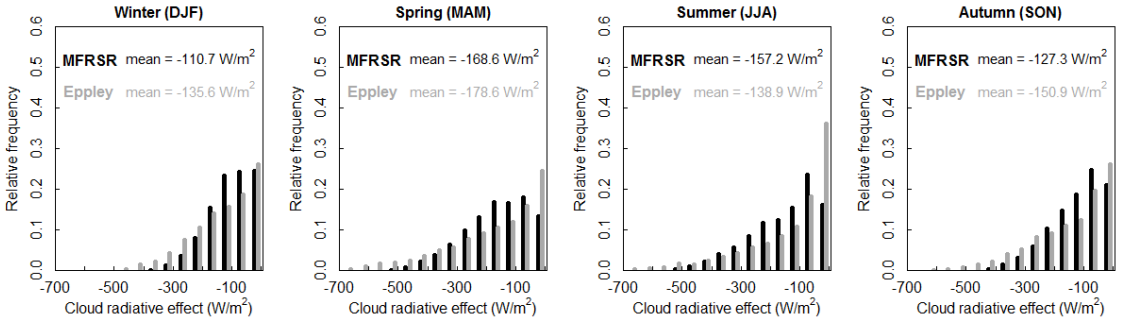

FIGURE 3.2 Seasonal variability of the SW cloud radiative effect at the surface.

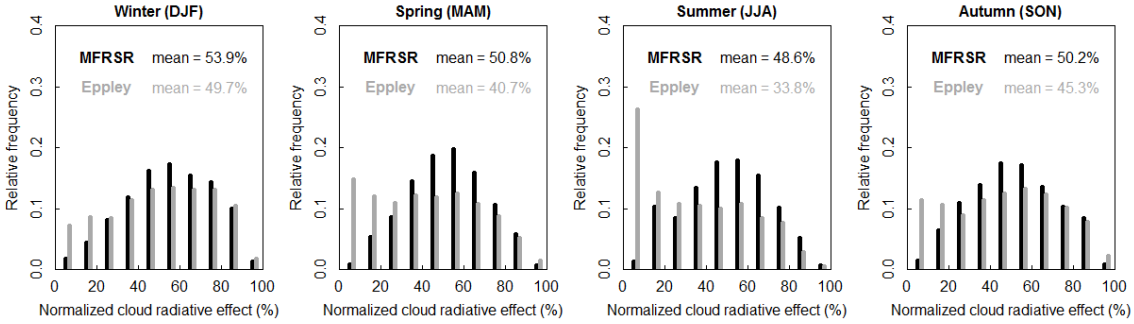

FIGURE 3.3 Seasonal variability of the normalized SW cloud radiative effect at the surface.

3.3.1 ECOT vs. MODIS cloud optical thickness

The ECOT values are compared with the MODIS cloud optical thickness retrievals (MODIS COT) obtained from Collection 051 of the MODIS cloud product Level 2 data (King et al. 1997; Menzel et al. 2010), at 1 km spatial resolution. Datasets of MODIS COT are considered over an area of 0.2º × 0.2º, centred in the geographical coordinates of the ICT observatory (38º34′N, 7º54′W) where the MFRSR is installed and in correspondence, ECOT values differing by up to 1 h (before or after) from the MODIS overpass time are taken. The area 0.2º × 0.2º is considered to be an area representative of the characteristics of the Évora site in terms of cloud extension and radiative properties of the surface (albedo). Cloud type is determined from MODIS cloud product and data is filtered to obtain only non-precipitating water clouds, corresponding to cloud fractions greater than 0.25 in the area considered. This selection is done using simultaneous rain-gauge data of the meteorological station installed at the ICT observatory. This comparison aims at evaluating the ability of the ECOT to represent the cloud optical thickness variability over such an area. Figure 3.4 shows the relation found between the MFRSR and MODIS cloud optical thickness mean values, corresponding to 205 MODIS scenes. Overall results show that the ECOT is a good indicator of the cloud optical thickness with a correlation coefficient of 0.81 and a root mean square error (RMSE) of 5.8. The spatial (MODIS) and temporal (MFRSR) variability of the cloud optical thickness mean values is represented, respectively, by the horizontal and vertical error bars in figure 3.4. The obtained relation between MFRSR and MODIS, in figure 3.4, shows that the MFRSR cloud optical thickness tends to overestimate the MODIS COT (intercept of 3.94) suggesting that the ECOT may be more sensitive to higher values of the cloud optical thickness values in the area. Nevertheless, these results show that the ECOT represents quite well the cloud optical thickness over the study area.

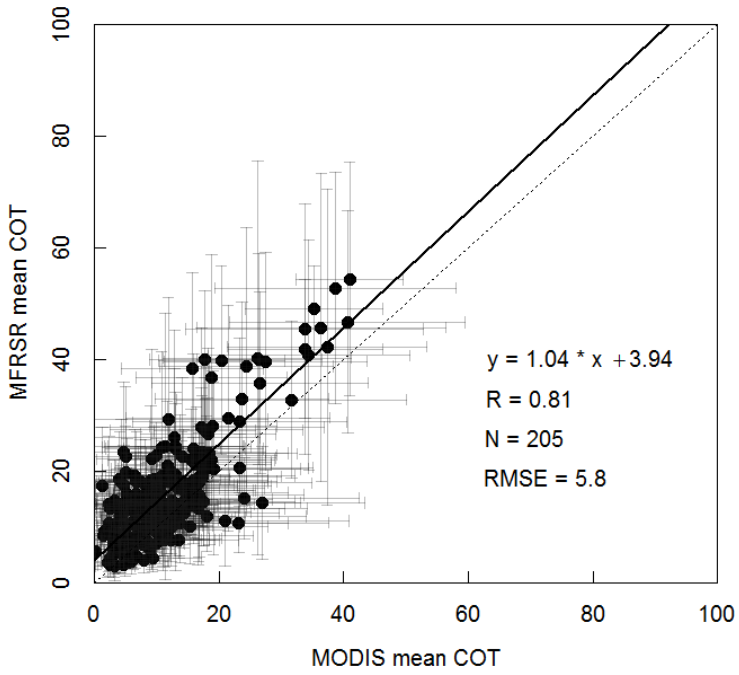

FIGURE 3.4 Scatter plot relating the MFRSR and MODIS COT mean values over an area of 0.2º × 0.2º, centred in the geographical coordinates of the ICT observatory. The dashed grey line represents the relation 1:1.

3.3.2 ECOT vs. NCRESW

The scatter plots in figure 3.5 present the relation between $NCRE_{SW}$ and ECOT for both instruments, MFRSR [figure 3.5 (a)] and Eppley [figure 3.5 (b)]. The normalized CRE_{SW} values are used instead of the absolute CRE_{SW} values, which would result in a great dispersion of the data (due to the solar zenith angle dependence). The data represented in figure 3.5, comprising 1349 points (460 in winter, 483 in spring, 274 in summer and 132 in autumn), correspond to the ECOT dataset described previously (sub-section 3.3.1) before being averaged. This dataset assumes that the cloud phase maintains the same over the area during this period, i.e., non-precipitating water cloud conditions to cloud fractions greater than 0.25 and excluding the overcast conditions. The MFRSR $NCRE_{SW}$ and the ECOT values are related by a logarithmic function, presenting a root mean square error (RMSE) of 7.2%. The same type of function may be used to fit the relation between the Eppley $NCRE_{SW}$ and the ECOT values, however the dispersion of data is considerably higher with a RMSE of 16%. The reason for the increased scattering of data from the MFRSR to the Eppley instrument is connected to

the enlargement of the spectral region from the first to the second one, which includes several absorption bands, especially of water vapour, becoming extremely variable. The SW radiation at the surface is particularly sensitive to these variations and its influence is increasingly important for decreasing cloud fractions when the clear-sky contribution becomes larger, and greater errors associated to ECOT retrievals are expected. Although water vapour plays a role in the reflection and absorption characteristics of cloudy atmospheres (Fung and Ramaswamy 1999), it is expected that the dispersion of data is lower for overcast situations, when the contribution of clouds becomes predominant. To note also that in general, the winter season presents for both MFRSR and Eppley instruments, slightly higher $NCRE_{SW}$ values than for the remaining seasons, for the same ECOT values; conversely, spring season presents a slightly different behaviour, with the $NCRE_{SW}$ values smaller than those corresponding to the remaining seasons. This enhanced effect of the $NCRE_{SW}$ values in winter can be related with the lowest levels of SW clear-sky irradiance available in this season. On the other hand, for a same ECOT value the radiation extinction due to clouds in winter season can be greater than in the other seasons due to the longer atmospheric path. Thus, the radiation extinction can be translated by a higher percentage value relatively to the SW clear-sky irradiance in that season.

The relation between the $NCRE_{SW}$ and ECOT for both MFRSR and Eppley instruments, under overcast cloudy conditions, is shown in figure 3.6, being the dataset constituted by 229 occurrences (99 in winter, 101 in spring, 10 in summer and 19 in autumn). The RMSE relating the MFRSR $NCRE_{SW}$ with the ECOT is reduced [figures 3.5 (a) and 3.6 (a)], with a moderate decrease of the RMSE from 7.2% (all cloud fractions greater than 0.25 and excluding the overcast conditions) to 4.5% (overcast). The scatter plot of the Eppley $NCRE_{SW}$ as a function of the ECOT for overcast conditions [figure 3.6 (b)] presents a much lower dispersion of the data (a RMSE of 7.7%), with respect to that obtained for all cloud fractions [figure 3.5 (b)], with a RMSE of 16%. The slope is very similar for both equations [figures 3.5 (b) and 3.6 (b)], however the intercept is slightly different. These equations may constitute useful parameterizations to estimate the Eppley $NCRE_{SW}$ as a function of ECOT in mid latitude regions, especially in the case of overcast skies that present a relatively low dispersion of the data. The MFRSR and Eppley CRE_{SW} values can then be easily inferred from the previous parameterizations, using equations (3.2) and (3.3), if the

corresponding downward clear sky surface irradiances and the surface albedo are known.

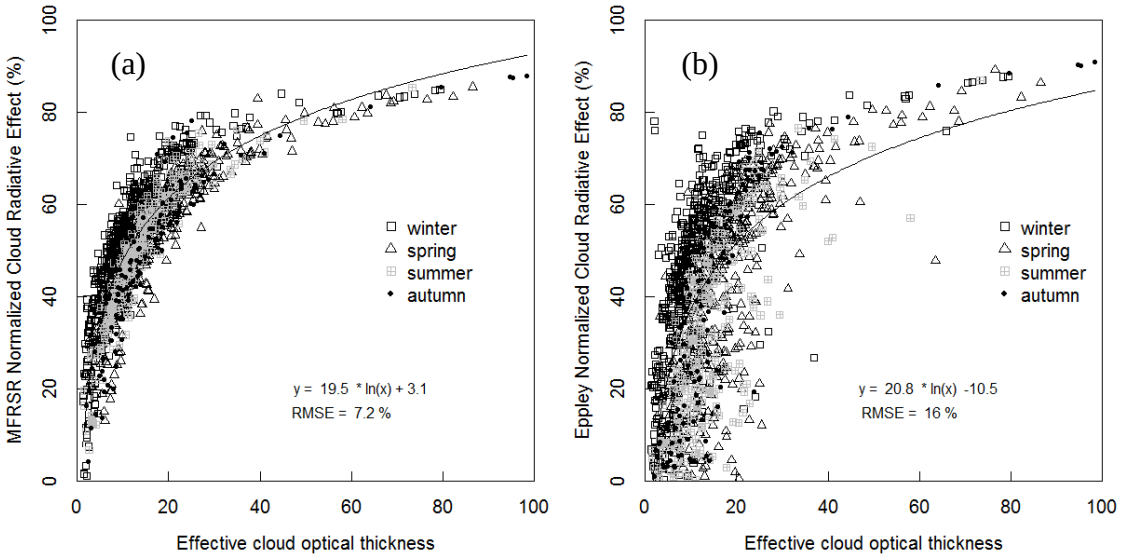

FIGURE 3.5 Scatter plot of the seasonal MFRSR $NCRE_{SW}$ (a) and Eppley $NCRE_{SW}$ (b) as function of the ECOT for non-precipitating water cloud conditions corresponding to cloud fractions greater than 0.25 and excluding the overcast situations.

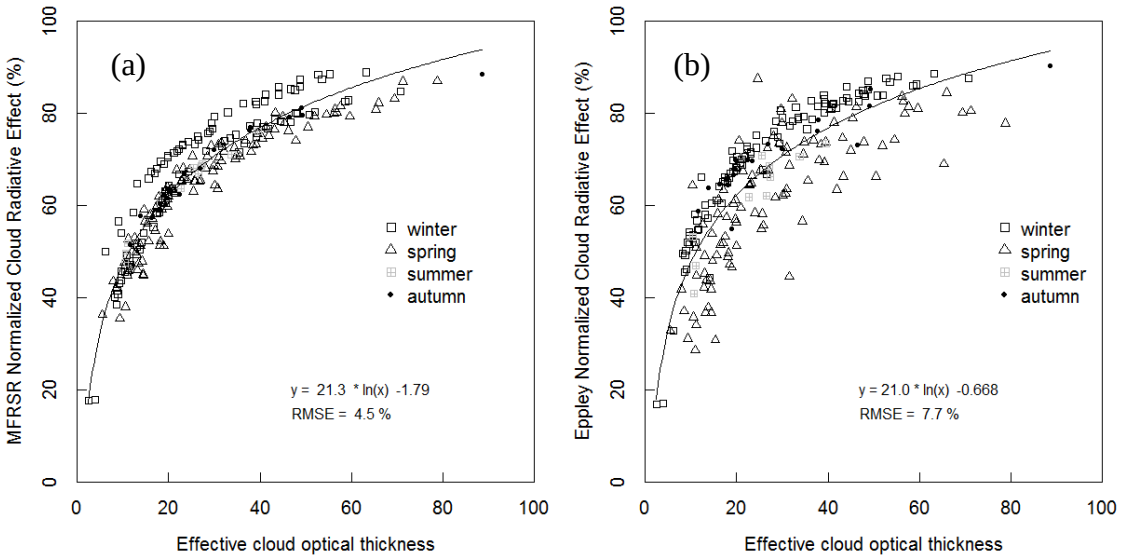

FIGURE 3.6 Scatter plot of the seasonal MFRSR $NCRE_{SW}$ (a) and Eppley $NCRE_{SW}$ (b) as function of ECOT for overcast sky situations.

3.3.3 NCRESW Efficiency

The shortwave cloud radiative effect efficiency, CRE_{SW} per unit of cloud optical thickness (Mateos et al. 2014a) can be understood as the rate change of the clear-sky SW irradiance with a unit increase in the cloud optical thickness. Here, the $NCRE_{SW}$ efficiency is investigated. The MFRSR and Eppley $NCRE_{SW}$ efficiencies as a function of ECOT under overcast sky conditions are presented in figure 3.7. It can be observed that as the ECOT increases, both for MFRSR and Eppley spectral regions, the $NCRE_{SW}$ efficiency decreases slowly for ECOT values higher than 50, approaching the unit for ECOT values obtained. The equations in figures 3.7 (a) and (b) translate the relation between $NCRE_{SW}$ efficiency and ECOT, which can be interpreted as follows: for very high ECOT values, the transmitted downward SW radiation for overcast conditions is strongly reduced due to absorption and reflection back to space (McBride et al. 2011), i.e. the SW radiation is intensely attenuated by clouds. Thus, the $NCRE_{SW}$ is very high and the $NCRE_{SW}$ efficiency tends to a low value. This means that for very high ECOT values, the $NCRE_{SW}$ efficiency becomes less sensitive to changes in ECOT.

The MFRSR $NCRE_{SW}$ efficiency [figure 3.7 (a)] presents quite low dispersion of the data, being the data well fitted by a power law model (RMSE = 0.40 %). The Eppley $NCRE_{SW}$ [figure 3.7 (b)] efficiency presents slightly higher dispersion of the data relatively to MFRSR $NCRE_{SW}$ for low values of the ECOT. A detailed analysis of each of these scattered data points shows that they always correspond to differences of more than 45 min with respect to the MODIS overpass time, therefore possibly corresponding to cloud fractions lower than one (recall that the ECOT dataset considered includes ECOT values with maximum differences of 1 h with respect to MODIS overpass time, assuming that the cloud phase is kept the same over the area during this period). Nevertheless, a power function can also be used to accurately model the data (RMSE = 0.55 %) as illustrated in figure 3.7 (b). The equations given in figure 3.7 allows for parameterizing the MFRSR and Eppley $NCRE_{SW}$ efficiencies for water clouds in overcast-sky conditions at midlatitudes.

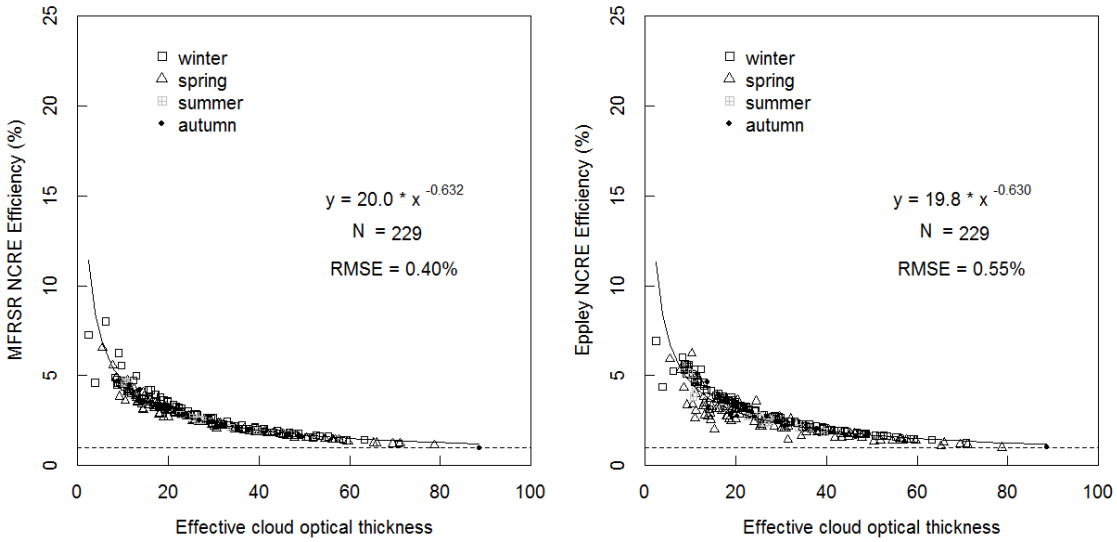

FIGURE 3.7 Scatter plots of the seasonal MFRSR $NCRE_{SW}$ (a) and Eppley $NCRE_{SW}$ (b) efficiencies as a function of the ECOT for overcast sky situations.

3.4 Summary and conclusions

Surface measurements of SW irradiance (spectral at 415 nm and broadband) were used to obtain the ECOT and CRE_{SW} in a mid-latitude site (Évora, - south of Portugal). The data, covering 7 years of measurements (2003-2010), were collected with a MFRSR radiometer and an Eppley pyranometer. Results showed that the seasonal variability of ECOT is in accordance with the seasonal variability of CRE_{SW}. Although, Eppley CRE_{SW} presents more negative values, due to the larger spectral band, relatively to MFRSR, the results showed that clouds can attenuate by up to 80% of SW radiation in all seasons considering both spectral bands and taking into account all cloud conditions in terms of type and fraction. The ECOT, obtained from MFRSR measured SW transmittance at 415 nm, was compared with the correspondent MODIS COT for non-precipitating water clouds and cloud fractions higher than 0.25. This comparison showed that the ECOT, although slightly overestimates MODIS COT, is a good indicator of the cloud optical thickness (with little dispersion R = 0.81, RMSE = 5.8) over the study area and thus can be related with cloud radiative effects. The CRE_{SW} values obtained from both instruments (MFRSR and Eppley) were normalized and related with the ECOT values. First, taking into account all-sky situations to cloud fractions higher than 0.25 and excluding overcast-sky situations, logarithmic functions

relating the $NCRE_{SW}$ and the ECOT were found, although with more dispersion for the Eppley than for MFRSR data. When considered only the overcast sky situations, the dispersion of Eppley data is significantly reduced and the logarithmic relation between $NCRE_{SW}$ and ECOT is kept. In addition, for overcast sky situations, a power law function translates the relation found between $NCRE_{SW}$ efficiency and ECOT. This relation, with little dispersion for both spectral ranges used (MFRSR and Eppley instruments), showed that as the ECOT increases the $NCRE_{SW}$ efficiency decreases approaching the unit for ECOT values higher than about 50. These relations obtained for overcast sky conditions constitute useful parameterizations of the $NCRE_{SW}$ and $NCRE_{SW}$ efficiency at a rural inland mid-latitude site, where Évora site is located.

Acknowledgements

The first author is financed through FCT (the Portuguese Science and Technology Foundation) grant SFRH/BD/88669/2012. The work is co-funded by the European Union through the European Regional Development Fund, included in the COMPETE 2020 (Operational Program Competitiveness and Internationalization) through the ICT project (UID / GEO / 04683/2013) with the reference POCI-01-0145-FEDER-007690. The authors wish to thank Sérgio Pereira and Samuel Bárias for maintaining instrumentation that allowed the measurement of data used in this work.

MODIS data were obtained from the Level 1and Atmosphere Archive and Distribution System (LAADS, http://ladsweb.nascom.nasa.gov). Thanks are due to AERONET/PHOTONS and RIMA networks for the scientific and technical support. CIMEL calibration was performed at the AERONET-EUROPE GOA calibration center, supported by European Union's Horizon 2020 research and innovation programme (grant agreement No 654109).

4 CLOUD PARAMETER RETRIEVALS FROM METEOSAT AND THEIR EFFECTS ON THE SHORTWAVE RADIATION AT THE SURFACE

This chapter is a transcription of the paper with the following reference[3]:

Salgueiro, V., M. J. Costa, A. M. Silva, C. Lanconelli, and D. Bortoli. 2017. "Cloud parameter retrievals from Meteosat and their effects on the shortwave radiation at the surface." *International Journal of Remote Sensing*, 38:4: 1137-1161. doi: 10.1080/01431161.2017.1280630

Abstract

A method based on SEVIRI (Spinning Enhanced Visible and Infrared Imager) measured reflectance at 0.6 and 3.9 μm is used to retrieve the cloud optical thickness (COT) and cloud effective radius (r_e) over the Iberian Peninsula. A sensitivity analysis of simulated retrievals to the input parameters demonstrates that the cloud top height is an important factor in satellite retrievals of COT and r_e with uncertainties around 10% for small values of COT and r_e; for water clouds these uncertainties can be greater than 10% for small values of r_e. The uncertainties found related with geometries are around 3%. The COT and r_e are assessed using well-known satellite cloud products, showing that the method used characterize the cloud field with more than 80% (82%) of the absolute differences between COT (r_e) mean values of all clouds (water plus ice clouds) centred in the range from ±10 (±10 μm), with absolute bias lower than 2 (2 μm) for COT (r_e) and root mean square error values lower than 10 (8 μm) for COT (r_e). The cloud water path (CWP), derived from satellite retrievals, and the shortwave cloud radiative effect at the surface (CRE_{SW}) are related for high fractional sky covers (F_{sc} > 0.8), showing that water clouds produce more negative CRE_{SW} than ice clouds. The COT retrieved was also related to the cloud modification factor, which exhibits reductions and enhancements of the surface SW radiation of the order of 80% and 30%, respectively, for COT values lower than 10. A selected case study shows, using a

[3] The references are not transcribed here but presented at the end of the dissertation all together, in order to avoid repetitions.

ground-based sky camera that some situations classified by the satellite with high F_{sc} values correspond to situations of broken clouds where the enhancements actually occur. For this case study, a closure between the liquid water path (LWP) obtained from the satellite retrievals and the same cloud quantity obtained from ground-based microwave measurements was performed showing a good agreement between both LWP data set values.

4.1 Introduction

Clouds play a prominent role on the Earth's radiation budget through their interaction with solar and thermal radiation (Cess et al. 1989; Ramanathan et al. 1989; Harrison et al. 1990). The knowledge of the cloud physical properties, such as cloud optical thickness (COT) and particle effective radius, and its relationship with radiative fluxes is essential to understand the cloud radiation interactions. Clouds continuously vary in space and time as they are dynamic systems. Thus, methods to retrieve cloud properties with an adequate temporal frequency and large area coverage are crucial to monitor the cloud evolution and its radiative effects. Satellites are very instrumental for studying and monitoring cloud evolution at regional and global scales. In particular, operational geostationary meteorological satellites enable a near-real-time cloud monitoring on a large scale due to their unrivalled image space coverage and time repetition.

For several decades, remote-sensing techniques using selected spectral bands in the visible (VIS), near-infrared (NIR) and thermal infrared (IR) have been developed to determine cloud properties. Nakajima and King (1990) were among the first to use reflected solar radiation at VIS and NIR wavelengths to retrieve simultaneously the cloud COT and the effective radius (r_e) of water clouds. Since then, different algorithms based on passive sensor measurements on board polar and geostationary satellites have been proposed to characterize the cloud field in terms of physical properties (e.g., COT, effective radius, thermodynamic phase, cloud top height, liquid, and ice water paths) (Nakajima and Nakajma 1995; King et al. 1997; Jolivet and Feijt 2003; Baum and Platnick 2006; Roebeling et al. 2006; Costa et al. 2007; Bugliaro et al. 2011). Examples of passive sensors used nowadays to obtain cloud properties from combined VIS/IR remote-sensing techniques are the Moderate Resolution Imaging Spectroradiometer (MODIS) flying on board the low Earth orbit Terra and Aqua Earth Observing System (EOS) platforms and the Spinning Enhanced Visible and Infrared Imager (SEVIRI) on

board the Meteorological Satellite (Meteosat) satellites on a geostationary orbit. The Climate Monitoring Satellite Application Facility (CM-SAF) of the European Organization for the Exploitation of Meteorological Satellites (EUMETSAT) provides geophysical parameter datasets for climate monitoring (e.g. radiation budget and cloud parameters) derived from satellite measurements (Schulz et al. 2009). Among the data sets provided by the CM-SAF, the Cloud Property Data Set (CLAAS) (Stengel et al. 2014), obtained using hourly SEVIRI data, is based on a period of 8 year measurements (from 2004 until the end of 2011) and derived with the Cloud Physical Properties (CPP) algorithm (Roebeling et al. 2006; Meirink 2013). The National Aeronautics and Space Administration (NASA) Goddard Earth Sciences Distributed Active Archive Centre (GES DAAC) also provides cloud products (Baum and Platnick 2006) from MODIS low Earth orbit of the spacecraft (Terra and Aqua) twice a day over the same spot at mid-latitudes. MODIS Level 2 cloud property retrievals are assessed in Painemal and Zuidema (2011), with the COT correlating well with aircraft-derived values, with MODIS presenting larger values (mean difference = 1.42) and the standard effective radius at 2.1 µm exceeding the *in situ* cloud top effective radius with a mean bias of 2.08 µm. MODIS is the reference used to compare cloud physical property retrievals from ground-based data (Min et al. 2012), as well as aircraft (Min et al. 2012) and space-born instruments. For example, Stengel et al. (2014) evaluate the CPP cloud product of CM-SAF against MODIS retrievals at pixel level, reporting bias values of 1.8 for COT and of -0.1 g m^{-2} (-6.7 g m^{-2}) for liquid water path (ice water path).

Cloud radiation interactions still represent a source of uncertainty (Boucher et al. 2013) because of the potential variations in cloud properties as the cloud droplet number concentration, which can be calculated by combining the COT and effective radius retrievals (Painemal and Zuidema 2011). The interaction between clouds and radiation can be estimated by using the cloud radiative forcing, which is a measure of the net total fluxes (all-sky fluxes minus clear-sky fluxes in shortwave plus longwave spectral ranges; in W m^{-2}) (Ramanathan et al. 1989). In general, the total radiative effect produced by clouds is negative causing a cooling effect in the earth-atmosphere system with negative and positive contributions of the shortwave and longwave components, respectively. Since the improvement of satellites, ground-based instrumentation and climate models, different studies of cloud radiative effects have been performed (Oreopoulos and Rossow 2011; Allan 2011; Calisto et al. 2014; Dong et al. 2006; Berg

et al. 2011). The International Satellite Cloud Climatology Project [ICCP; Schiffer and Rossow (1983)] was the first project whose basic objective is to collect and analyse satellite radiance data to infer the global distribution of cloud radiative properties, in order to improve the modelling of cloud effects on climate. Orepoulos and Rossow (2011) examined the cloud radiative effects of various cloud regimes using a 24-year long-term data set from the ICCP for three distinct geographical zones covering most of the Earth's surface area. Calisto et al. (2014) analysed and compared the radiative forcing for 10 years of the Clouds and the Earth's Radiant Energy System onboard Terra and Aqua satellites (CERES) measurements with 11 Coupled Model Intercomparison Project Phase 5 (CMIP5) models. A global mean SW cloud radiative forcing between -54.7 and -40.8 W m^{-2} for the CMIP5 models and -47.5 W m^{-2} for CERES was found. Allan (2011) used Geostationary Earth Radiation Budget (GERB) onboard Meteosat-9 satellite and CERES satellite data and numerical forecast model reanalysis data to compute an estimate of the cloud radiative effect on the global multi-annual mean radiative energy budget of the atmosphere and surface, and a net cooling of the climate system of -21 W m^{-2} was found. Using ground-based measurements, Berg et al. (2011) found a shortwave cloud radiative forcing average value of -45.5 W m^{-2} for shallow cumuli and Dong et al. (2006) showed that the shortwave cloud radiative forcing for a mid-latitude site exhibits minimum values in spring for all sky conditions. This study aims at contributing to the understanding of the relation between cloud parameters and solar radiation received at the surface, taking advantage of the adequate temporal resolution of geostationary satellites to provide the cloud daily evolution. It is demonstrated here through a closure procedure that for certain cloud situations, it is indeed possible to relate satellite cloud retrievals (obtained from above the clouds) with ground-based observations (made below the clouds) of the same cloud quantity.

The Iberian Peninsula, located at midlatitudes in southwestern Europe, is usually affected by contrasting air masses (Raes et al. 2000), with marked differences in terms of cloud occurrences between the cold and warm seasons (Salgueiro et al. 2014), offering thus good opportunities not only for cloud studies but also for studies of cloud-aerosol interactions due to the different origin of the aerosols carried by the different air masses passing in the region (Silva et al. 2002; Santos et al. 2008). On the other hand, the southern regions of the Iberian Peninsula typically present the highest values of annual surface solar radiation in Europe (Bojanowski et al. 2014), which highly depend

on the COT (Mateos et al. 2014a; Salgueiro et al. 2014). For these reasons, the Iberian Peninsula presents suitable conditions to study the cloud properties and their influence on solar radiation at the surface, to deepen the understanding of cloud radiation interactions in the area.

This work aims to study the relation of two cloud quantities retrieved from satellite measurements (COT and effective radius) with shortwave cloud radiative effects obtained from ground-based global irradiance measurements taken in 2015 in Évora region, southwestern Iberian Peninsula. There are studies that analyse the relation between cloud properties and solar radiation at this region, using ground-based measurements of both (Antón et al. 2012; Mateos et al. 2014a; Mateos et al. 2014b; Salgueiro et al. 2016). However, to our knowledge, no study has yet addressed the relation between cloud parameters obtained from geostationary satellite remote sensing and surface solar radiation measurements at the study region taking advantage of the adequate temporal resolution of Meteosat satellite to provide the cloud daily evolution while monitoring a suitable area.

The satellite and surface radiation data used as well as the description of the retrieval method can be found in section 4.2. The results and discussion, including the comparison of the cloud properties retrievals with independent data, as well as the relation between the cloud properties and the shortwave radiative effects are presented in section 4.3. Summary and conclusions are presented in section 4.4.

4.2 Methods and data

4.2.1 Satellite data and cloud parameter retrievals

Satellite data of the SEVIRI radiometer on board Meteosat satellite were used in this work. SEVIRI is a passive imaging radiometer (Schmetz et al. 2002) that provides continuous observations (every 15-minute), of the earth-atmosphere system covering a region that includes Europe. It measures radiation in 12 spectral channels in the VIS, NIR, and IR spectral regions. Eleven of these channels provide data of the Earth's full disc with an image sampling distance of 3 km at sub-satellite point, at wavelengths between 0.6 μm and 14 μm. A high-resolution visible (HRV) channel (broadband: 0.4-1.1 μm) is also included, with sampling distance of 1 km at nadir. The satellite data used in this work were obtained from EUMETSAT Earth Observation Portal, corresponding to SEVIRI level 1.5 image data.

The retrieval method used in this work is based on the well-known principle that cloud reflectances at non-absorbing wavelengths in the VIS spectral region are strongly related with COT, while at absorbing wavelengths, in the NIR region, they are primarily related to cloud particle size (Nakajima and King 1990; Nakajima and Nakajma 1995). In fact, the sensitivity of the non-absorbing (absorbing) reflectances to the COT (cloud effective radius) are almost orthogonal functions (Nakajima and King 1990). Thus, the COT and effective droplet radius/ice particle size (r_e) can be determined from the comparison between pre-calculated reflectances and the corresponding measured quantities. The method uses two SEVIRI channels, VIS0.6 (centred at 0.635 μm) and IR3.9 (centred at 3.90 μm), and is limited to daytime applications because it depends on solar radiation. In the VIS spectral region, the channel VIS0.6 was chosen due to the lower reflectivity of the surface and vegetation so that thin (or transparent) clouds are better detected. The channel IR3.9 was chosen due to its sensitivity to cloud top conditions (Rosenfeld et al. 2004), and it is used to obtain the effective droplet radius/ice particle size near the cloud tops. At 3.9 μm both solar reflection and thermal emission take place during daytime, since the emission by the surface, atmosphere and clouds provide a non-negligible contribution to the total IR3.9 radiance. Hence, the cloud reflectance at 3.9 μm is determined assuming the following assumptions (Charvát 2007; Kaufman and Nakajima 1993): the same type of cloud homogenously covers the whole pixel; clouds are partially opaque with respect to radiation, that is, there is no upward transmission of radiation through the cloud from the surface and from the atmosphere below the cloud therefore the cloud reflectance plus its emittance is unity. The relation between the total upward radiance ($I_{3.9}$) and the cloud reflectance ($r_{3.9}$) adopted is translated by equation (4.1) from Kaufman and Nakajima (1993):

$$I_{3.9} = \tau_{3.9}^{0}\left(\frac{F_0\mu_0}{\pi}\right)r_{3.9} + \tau'_{3.9}B_{3.9}(T)(1 - r_{3.9}) \qquad (4.1)$$

In equation (4.1), the first and second terms on the right side represent the solar and thermal components of the IR3.9 upward radiance at the satellite level (top of the atmosphere), respectively; τ^0 is the total downward and then upward transmission of sunlight above the cloud, τ' is the upward transmission of thermal radiation above the cloud, F_0 is the extra-terrestrial solar flux at IR3.9 channel, μ_0 is the cosine of the solar zenith angle and $B_{3.9}(T)$ is the thermal radiance represented by the Planck function at

temperature T and wavelength 3.9 μm. The temperature, T, is approximated by the brightness temperature of cloud top given by channel IR10.8, since at this wavelength the emissivity is close to one for all surfaces and the atmospheric absorption is low. The thermal component is then estimated following the relation between the SEVIRI radiances and the equivalent brightness temperature described in EUMETSAT (2012), and the transmittance follows the theory described in the work of Charvát (2007). The cloud reflectance at IR3.9 channel can be derived from equation (4.1) as shown in equation (4.2):

$$r_{3.9} = \frac{I_{3.9} - \tau'_{3.9} B_{3.9}(T)}{\tau^0_{3.9} F_0 \mu_0 / \pi - \tau'_{3.9} B_{3.9}(T)} \qquad (4.2)$$

Look-Up Tables (LUTs) of calculated reflectances as seen by Meteosat were built using the one-dimensional (1D) radiative transfer code Library for Radiative transfer (LibRadtran) (Mayer and Kylling 2005). These reflectances were calculated for different values of COT, effective droplet radius/ice particle size, solar zenith angle (θ_0), satellite zenith angle (θ) and relative azimuth angle ($\Delta\varphi$) defined as the difference between solar and satellite azimuthal angles (see table 4.1). The calculations were done using the different spectral response functions of the VIS0.6 and IR3.9 channels of the SEVIRI instrument. Solar and satellite zenith angles were chosen within the ranges of valid values over the Iberian Peninsula.

TABLE 4.1 Input parameters used in the LUT calculations: cloud effective droplet radius/ice particle size (r_e), cloud optical thickness (COT), solar zenith angle (θ_0), satellite zenith angle (θ) and relative azimuth angle ($\Delta\varphi$). In bold the values considered for the sensitivity analysis.

Input parameter	Values used	
r_e (μm)	Water clouds: 2, **4**, **6**, **9**, **12**, **15**, **20**, 25	Ice clouds: 5, **7**, **10**, **15**, **20**, **30**, **40**, 50
COT	0.5, **1**, **2**, **4**, **7**, **10**, **14**, **20**, **30**, **50**, 70	
θ_0 (°)	From 5° to 70° with step of 1°	
θ (°)	From 35° to 55° with step of 1°	
$\Delta\varphi$ (°)	From 0° to 180° with step of 1°	

The radiative transfer calculations were done considering a homogeneous and plane-parallel cloud layer constituted by liquid or ice particles with geometrical thickness of 1 km. The cloud top is located at 3 and 7 km for water and ice clouds, respectively. The

main difference between water and ice clouds is that the latter usually are formed by non-spherical particles with no unique definition of their effective size. Thus, the conversion from microphysical to optical properties uses different parameterizations. For water clouds, hydrometeors are assumed spherical and the conversion is done using pre-calculated Mie tables. For the ice cloud properties, the conversion is done by using the parameterization from Baum et al. (2005a, 2005b) where the bulk scattering model is based on reanalysis of *in situ* data from a variety of midlatitude and tropical ice cloud field experiments. The atmosphere is characterized by default conditions for aerosols (Shettle 1989) and gases from a midlatitude profile comprising 50 levels between 0 and 120 km (Anderson et al. 1986). Gas absorption was parameterized using the LOWTRAN model (Pierluissi and Peng 1985), as adopted by the SBDART radiative transfer code (Ricchiazzi et al. 1998) that includes all radiatively active molecular species found in the Earth's atmosphere. The underlying surface albedo is selected from the LibRadtran database of the International Geosphere Biosphere Programme (IGBP) albedo libraries (Belward and Loveland 1996). The radiative transfer equation was numerically solved using the discrete ordinate method (Stamnes et al. 2000) with 16 quadrature angles.

Figure 4.1 shows a flowchart of the method followed to obtain COT and r_e for each SEVIRI pixel (approximately 3 × 3 km). As a first step, each pixel is classified in terms of thermodynamic phase as water or ice cloud following the cloud classification proposed by Costa et al. (2007). This cloud classification is based on the use of VIS and IR measurements assuming that clouds are made of either liquid water or ice particles, hence not considering mixed phase clouds. Afterwards, a pre-calculated LUT is selected according with the pixel content (water or ice cloud) and pixel viewing geometry (solar zenith angle, satellite zenith angle and relative azimuth angle). Subsequently, both quantities, COT and r_e, are retrieved evaluating the locations of the SEVIRI measured reflectances (VIS0.6 and IR3.9) on the selected LUT using linear interpolation. The retrieved COT and r_e, hereinafter termed as Cloud Properties using SEVIRI (CPS), are compared with two sets of independent data: MODIS cloud product (MOD06_L2) collection 5.1 (Baum and Platnick 2006) and Cloud Physical Properties (CPP-Product) of CM-SAF (Stengel et al. 2014). The MOD06_L2 cloud product used includes thermodynamic phase, optical thickness and particle size derived at the spatial resolution of 1 km from the MODIS scanning radiometer flying on board Terra satellite

platform. The CPP-Product is a pixel-based hourly product with spatial characteristics identical to the SEVIRI imaging projection and resolution (approximately 3 × 3 km at the sub-satellite point). The CPP-Product used here (COT, cloud effective radius and cloud thermodynamic phase) corresponds to SEVIRI/MSG2 level 1 (version 001).

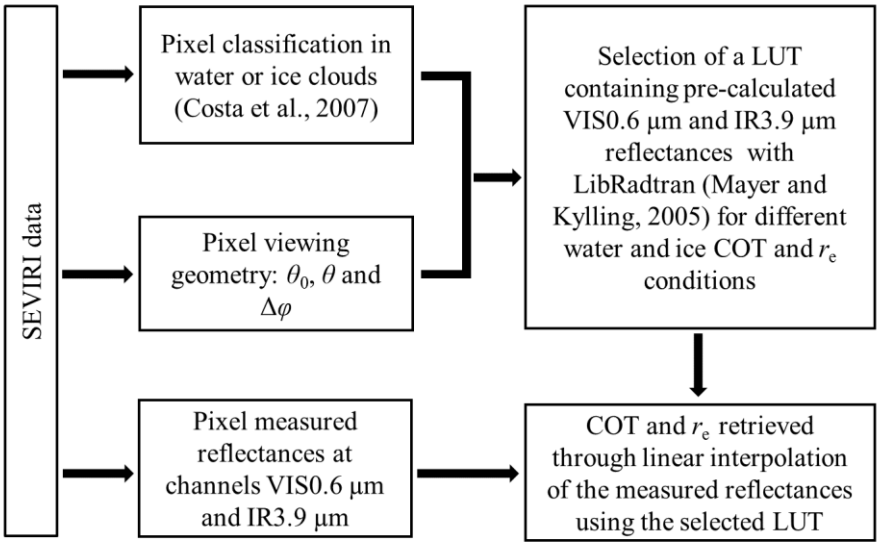

FIGURE 4.1 Flowchart of the method followed to obtain cloud optical thickness (COT) and r_e from Spinning Enhanced Visible and Infrared Imager (SEVIRI) measured reflectances.

4.2.2 Surface data and cloud radiative effects calculations

The shortwave cloud radiative effect at the surface (CRE_{SW}) can be defined as the difference between the net shortwave irradiance (downward minus upward shortwave irradiance) in cloudy and clear sky conditions, translating changes in the SW radiation that reaches the surface due to changes in clouds (type and/or cover). CRE_{SW} can be expressed by equation (4.3) (Ramanathan et al. 1989) where α is the surface albedo and $F^{\downarrow}$ represents the downward global SW irradiance at the surface under cloudy (cld) and clear sky (cs) conditions:

$$\mathrm{CRE_{SW}} = (1-\alpha)\left(F^{\downarrow}_{\mathrm{cld}} - F^{\downarrow}_{\mathrm{cs}}\right) \qquad (4.3)$$

The measured global and diffuse SW irradiance was recorded with a Kipp&Zonen CM 6B, which complies with the specifications for “first class” pyranometer

(broadband 305 – 2800 nm) during the period from January to December of 2015 with a temporal sampling of 1 minute. The global SW clear sky irradiance corresponding to each measurement was calculated using the empirical clear sky method proposed by Long and Ackerman (2000), which identifies and produces continuous estimates of clear sky SW irradiance at the surface. A cloud screening algorithm based on independent tests of the SW components (global and diffuse), selects clear sky events on a 1-minute basis comparing measured values and their temporal variability, with solar zenith angle corrected threshold limits. When enough points per day are flagged as clear (~100), a power law is fitted to represent the SW clear sky global irradiance, using the cosine of the solar zenith angle as the independent variable. The two regression parameters are interpolated in time for days that do not satisfy the minimum requirement in terms of number of clear sky events.

Visual information using an all sky camera was also used to check the cloud cover conditions. Liquid water path measurements obtained using a RPG-HATPRO humidity and temperature profiling passive microwave radiometer (MWR), with an accuracy of ± 20 g m^{-2} (Rose et al. 2005) were also used to perform a closure with the LWP obtained from the satellite retrievals. MWR has two bands 22-31 GHz (seven channel filter bank humidity profiler and LWP radiometer) and 51-59 GHz (seven channel filter bank temperature profiler) and presents zenith and azimuth scanning capabilities. Attached to the MWR there are also a meteorological station and an infrared radiometer providing cloud base detection. All ground-based instrumentation used in this work is installed at the atmospheric physics observatory of the Institute of Earth Sciences (ICT; 38° 34′ N, 7° 54′ W, 293 m above mean sea level) in Évora.

4.3 Results and Discussion

4.3.1 COT and r_e retrievals

4.3.1.1 Sensitivity analysis of the LUTs to input parameters

A sensitivity analysis of the COT and r_e to LUT input parameters (cloud top height, surface albedo, aerosol optical thickness and viewing geometries) was performed to quantify the uncertainties in COT and r_e retrievals using the method described in section 4.2.1. Following the same methodology as in the LUT construction (section 4.2.1), new reflectance calculations were done for each of the different input parameters keeping all the others as in section 4.2.1. The COT and r_e, values considered in the sensitivity

analysis are the same as in the LUTs, excluding the first and last values (see table 4.1) in order to guarantee that the retrievals would fall inside the LUT domain. As for the analysed input parameters, they are varied one at a time while keeping the remaining ones fixed as done in the calculations of the LUTs: the cloud top height took the values 1, 1.5, 2 and 4 km for water clouds and 7.5, 8, 9, 10 and 11 km for ice clouds; the surface albedo (available from http://giovanni.gsfc.nasa.gov/giovanni/; last accessed 21 September 2016) took typical values of the different seasons (spatial averages over the Iberian Peninsula: winter = 0.14, autumn = 0.16 and summer = 0.17); the aerosol optical thickness was considered to take the values 0.05, 0.1, 0.2, 0.3 and 0.5. Since the viewing geometries vary in a large range of values (table 4.1), fixed values of solar zenith angle (30º), satellite zenith angle (40º) and azimuthal angle (140º) were chosen for the sensitivity analysis of the cloud top height, surface albedo and aerosol optical thickness. For the sensitivity analysis of the LUT geometry, the new reflectances were calculated for several angles differing 0.5º from those indicated in table 4.1, corresponding to the maximum possible geometric deviation of the LUT, since its geometric resolution is 1º. The retrieval method was then applied to these new reflectance values.

Figures 4.2 (a-f) and 4.3 (a-f) show the uncertainties in COT and r_e with the variations of cloud top height, surface albedo and aerosol optical thickness for water and ice clouds, respectively (the reference cases corresponding to the conditions considered in the LUTs are represented in each plot by the dotted line y = 0). The r_e (COT) variation in figures 4.2 (a-f) and 4.3 (a-f) are presented for fixed COT (r_e) values (intermediate values chosen from the range considered in the sensitivity analysis) for intelligibility of the plots. A value of COT equal to 10 was chosen to present the results of r_e uncertainties for both water and ice clouds, whereas the results of COT refer to r_e values of 12 and 10 μm chosen for water and ice clouds, respectively. In general, for water and ice clouds, the uncertainties due to the cloud top height variation increase with the COT and decrease with r_e. The maximum values reach around 10% for the highest COT values and for the lowest ice cloud r_e considered. As for water clouds, the large uncertainties reaching around 30% for small r_e are connected with the fact that a lower initial r_e value is considered with respect to ice clouds; note that for r_e = 7 μm the uncertainties are of the same order both for water and ice clouds. Although the cloud height affects the TOA reflectance in both SW channels used (0.6 and 3.9 μm), the

largest effect is on the NIR spectral region reflecting in the greater error of r_e with respect to COT retrievals. The seasonal albedo has little influence on r_e, but for small COT the uncertainties reach values larger than 10%. This happens because for small COT values the reflection from the surface becomes an important component of the reflectance that reaches the satellite, especially in the visible spectral region; in the NIR, this contribution is less important, which is reflected in the minor effect obtained on r_e. A similar behaviour is found for the aerosol optical thickness, also with the largest uncertainties occurring for small COT values, as expected, since the aerosol role becomes increasingly important in these cases. For water clouds, the aerosol optical thickness has little influence in the r_e values similarly to the surface albedo. The sensitivity analysis of the solar and geometries gives maximum uncertainties of the order of 3% both for COT and r_e, which may be attributed to the relatively high LUT geometric resolution considered (1º).

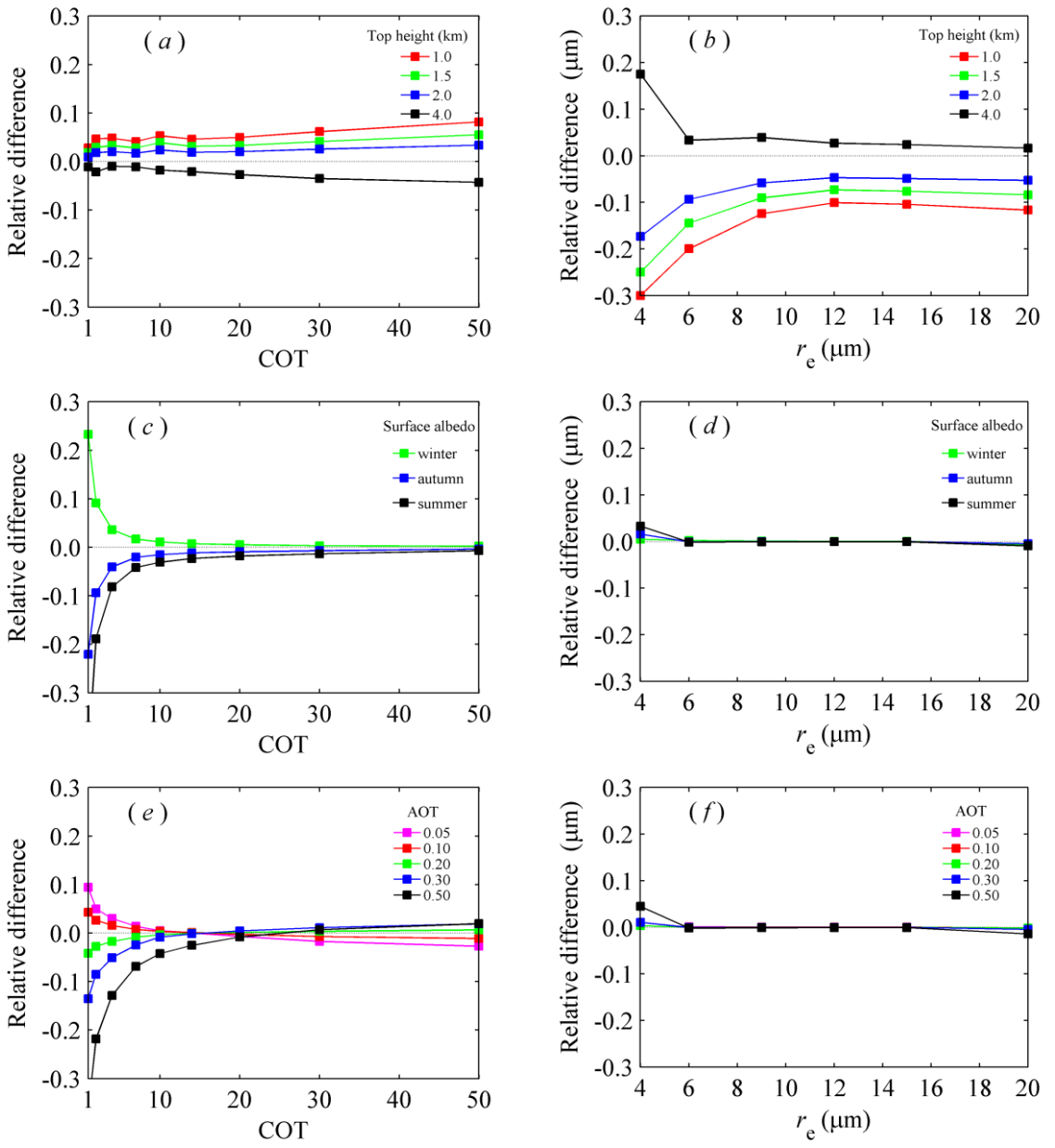

FIGURE 4.2 COT and r_e relative differences for water clouds (solar zenith angle of 30º, satellite zenith angle of 40º and relative azimuth angle of 140º) considering different values of cloud top height (a, b), surface albedo (c, d) and aerosol optical thickness (e, f). COT plots (a, c and e) and r_e plots (b, d and f) were done considering a fixed value of r_e = 12 μm and COT = 10, respectively.

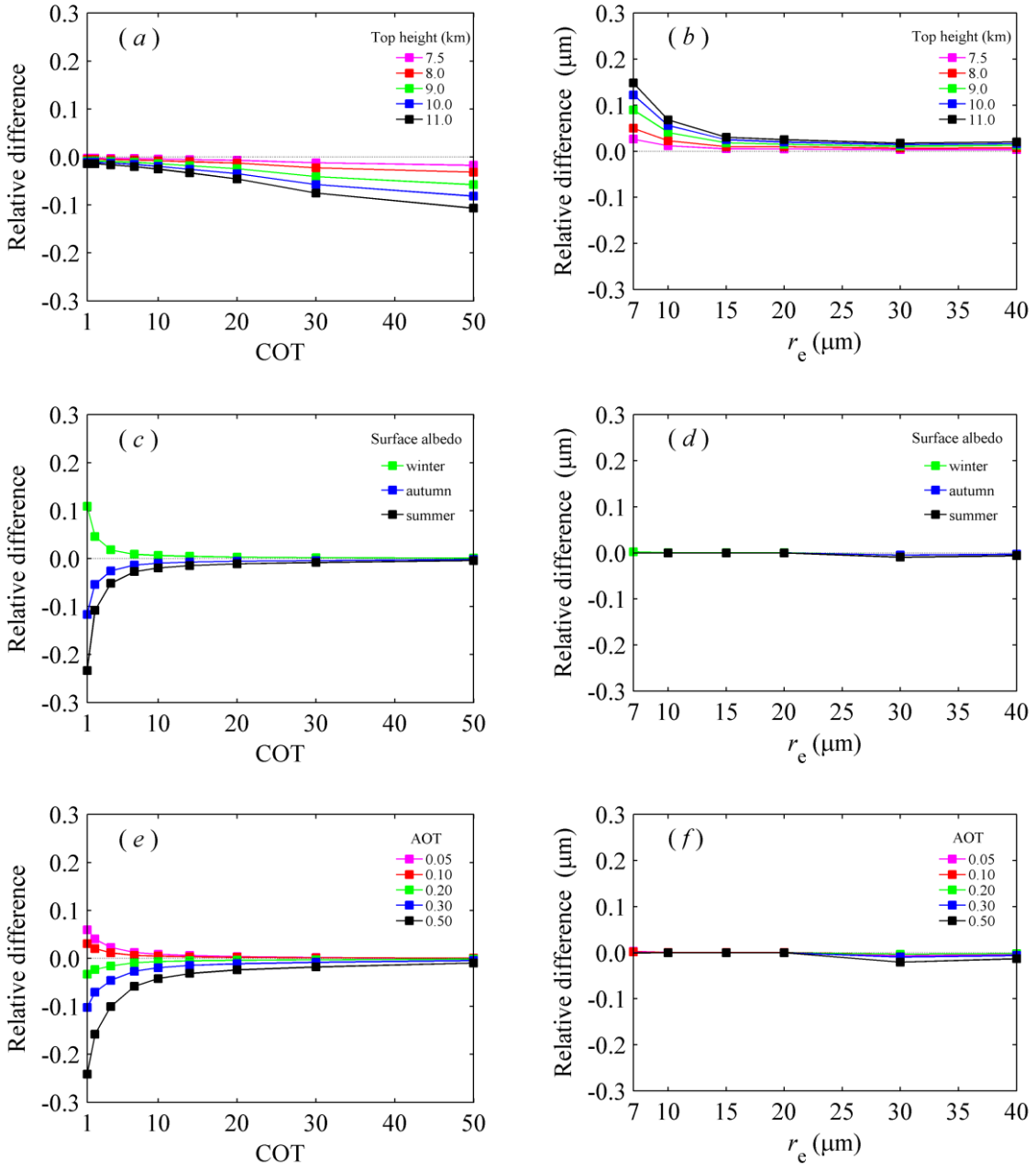

FIGURE 4.3 Same as in figure 4.2 but for ice clouds. COT plots (a, c and e) and r_e plots (b, d and f) were done considering a fixed value of r_e = 10 μm and COT = 10, respectively.

4.3.1.2 COT and r_e retrievals and comparison with independent data

A set of 22 SEVIRI images, covering the Iberian Peninsula (34° N to 44° N and 11° W to 4° E) during the period March - May 2011, were used to retrieve pixel-based COT and r_e values with the described methodology in subsection 4.2.1. The values obtained are compared with the corresponding MODIS (MOD06_L2) and CM-SAF (CPP-product) cloud products. SEVIRI images were selected for cases of clouds over the Iberian Peninsula, once a day when the SEVIRI data acquisition time was closer to the acquisition time of MODIS data on board Terra satellite and CPP product, which was available with an hourly frequency. This yielded maximum time differences of 15 minutes between SEVIRI and MODIS images. Due to the differences in spatial resolution between MODIS and SEVIRI radiometers, the comparison is done by averaging the pixel-based COT and r_e values in a regular longitude-latitude grid of 0.05° × 0.05° considering all cloudy pixels in each grid cell. The averages for water and ice clouds in table 4.2 were determined considering only the liquid or ice cloudy pixels in each cell, respectively. The distinction between water and ice clouds was done using the CPS cloud classification, as well as the MOD06_L2 and CPP cloud phase products.

TABLE 4.2 Statistical parameters bias and root mean square error (RMSE) of COT and r_e mean values.

	CPS vs. CPP	CPS vs. MOD06_L2	
Statistical parameter	All clouds		No. of grid points
Bias COT	1.26	-1.74	672552
RMSE COT	7.94	9.58	
Bias r_e (μm)	-0.92	-1.61	
RMSE r_e (μm)	7.65	6.13	
	Water clouds		
Bias COT	0.47	-1.08	204390
RMSE COT	7.62	8.93	
Bias r_e (μm)	-2.24	-1.32	
RMSE r_e (μm)	4.59	2.98	
	Ice clouds		
Bias COT	0.24	-3.79	249841
RMSE COT	7.11	10.06	
Bias r_e (μm)	1.39	-0.60	
RMSE r_e (μm)	9.37	7.28	

Figure 4.4 (a-f) shows the spatial distribution of the COT and r_e mean values obtained with CPS (a, b) over the Iberian Peninsula at 11:00 UTC on 1 May 2011. The equivalent MODIS image at 11:05 UTC on the same day was chosen, and the MOD06_L2 COT and r_e mean values are also represented in figure 4.4 (c, d) as well as the CPP COT and r_e mean values (e, f). In general, the cloud patterns obtained with CPS are very similar to the results from MOD06_L2 and from CPP [figure 4.4 (a-f)]. On the other hand, CPS seems to detect slightly fewer clouds than MOD06_L2 and CPP, which is more visible by the location of the grey areas in r_e figures. This detection of fewer clouds and the tendency to underestimate the r_e values by CPS are related to the inversely proportional relationship between the reflectance at 3.9 µm and r_e, that is, the reflectance at 3.9 µm decreases with increasing r_e, saturating for values higher than 30 µm (Rosenfeld et al. 2004). Therefore, because of this limitation, the method fails in certain ice cloud cases and the cloud properties are not retrieved explaining the detection of fewer clouds by CPS. For instance, in the north of the Iberian Peninsula there are areas in the cloud field where it is visible that the CPS presents some missing values of r_e, while for the same areas MOD06_L2 and CPP present r_e values higher than 40 µm. For all algorithms (CPS, CPP and MOD06_L2), the COT presents maximum values around 60 in the south as well as in some cloud structures over the north of the Iberian Peninsula. The areas where CPS COT values are missing in the cloud field are the same as for r_e. Yet, it should be noted that the absolute peaks in COT and r_e might not be displayed in the maps due to the spatial average done on the 0.05° × 0.05° grid.

Density scatter plots showing the distribution of COT and r_e mean values between the different algorithms (CPS, CPP and MOD06_L2) are represented in figure 4.5 (a-d). These mean values correspond to all clouds (water plus ice) in each grid cell (0.05° × 0.05°) considering the 22 SEVIRI images used. Most of the r_e values are between 0 and 15 µm, and the dispersion of the data seems to increase as r_e increases, being higher in the comparison with CPP than with MOD06_L2. The differences with respect to the r_e values are probably also due to differences in the algorithms, since the CPP algorithm weights the retrieved r_e with a climatological value of 8 µm for water clouds and 26 µm for ice clouds, respectively (Stengel et al. 2014). Both cases show the tendency of CPS to slightly underestimate the highest r_e values, which is in accordance with the bias values in table 4.2 and related with the aforementioned limitation of the 3.9 µm reflectance that saturates for high r_e values.

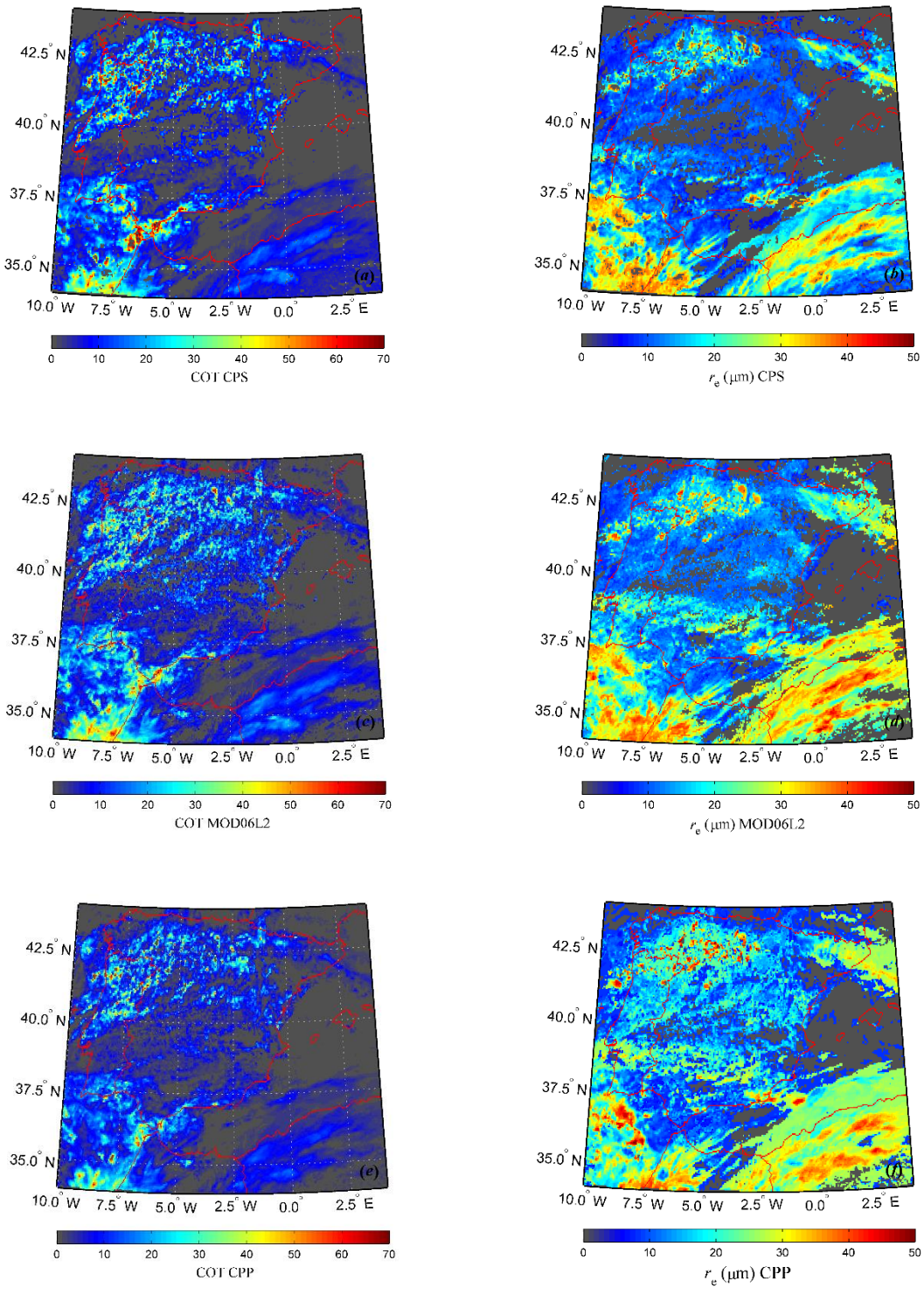

FIGURE 4.4 COT and r_e mean values in a regular grid of 0.05º × 0.05º on 1 May 2011 around 11:00 UTC. COT and r_e retrieved using CPS (a, b), MODIS (c, d) and CPP (e, f).

Still, the data density is low for higher r_e values. In general, the COT values are concentrated between 0 and 40. In both cases, the comparison of COT with the independent algorithms (CPP and MOD06_L2) shows a good agreement with low dispersion of the data. Considering the same data set, the frequency of occurrence of COT and r_e absolute differences between the different algorithms is presented in figure 4.6. Most of the COT absolute differences are centred in the range from -10 to +10 (CPS- MOD06_L2: 80.3 % and CPS-CPP: 86.8 %). The r_e absolute differences found in the range -10 to +10 µm are 89.7 % (CPS- MOD06_L2) and 81.9 % (CPS-CPP). The results of bias and root mean square error (RMSE) are presented in table 4.2 for all clouds in each grid cell and distinguished between water and ice clouds. These results show that CPS slightly overestimates the CPP COT and underestimates the MOD06_L2 COT in all cases (all clouds, water clouds and ice clouds). The behaviour of the effective radius is slightly different, since the CPS overestimates the CPP r_e for ice clouds and in the remaining cases it underestimates the CPP and MOD06_L2 r_e. The differences found between the different data sets are reasonable because the algorithms used in the comparisons are different. The main differences include the used spectral channel as non-absorbing and absorbing channels, as well as the slightly different image acquisition times and the different spatial resolutions of SEVIRI and MODIS. The CPP algorithm uses SEVIRI VIS0.6 and NIR1.6 as non-absorbing and absorbing channels, respectively (Stengel et al. 2014). As for MODIS cloud products, the retrieval scheme uses as non-absorbing band (0.65, 0.86 or 1.2 µm) combined with three longer wavelength bands where there is absorption (1.6, 2.1 and 3.7 µm). MOD06_L2 product provides three different effective sizes corresponding to each of the absorbing bands (Baum and Platnick 2006). The comparisons presented in this work were done for MODIS cloud effective radius retrieved at 3.7 µm. Zhang and Platnick (2011) performed a systematic assessment of the difference among effective radius retrieved at 1.6, 2.1 and 3.7 µm of marine water clouds and found that the r_e retrievals at 3.7 µm can be smaller than the ones at 1.6 and 2.1 µm. In addition, for convective clouds the radiation at 3.7 µm is more influenced by the uppermost part of the cloud, while at 1.6 µm the radiation originates from deep inside that same cloud and if the cloud droplets reach the precipitation potential, the r_e at 1.6 µm increases due to the precipitation droplets from the deeper portions of the cloud (Rosenfeld et al. 2004). In general, the

retrieved r_e at 3.9 µm tends to be small than the MOD06_L2 r_e (at 3.7 µm) and CPP r_e (at 1.6 µm) as can be seen in table 4.2 by the bias values lower than 0.

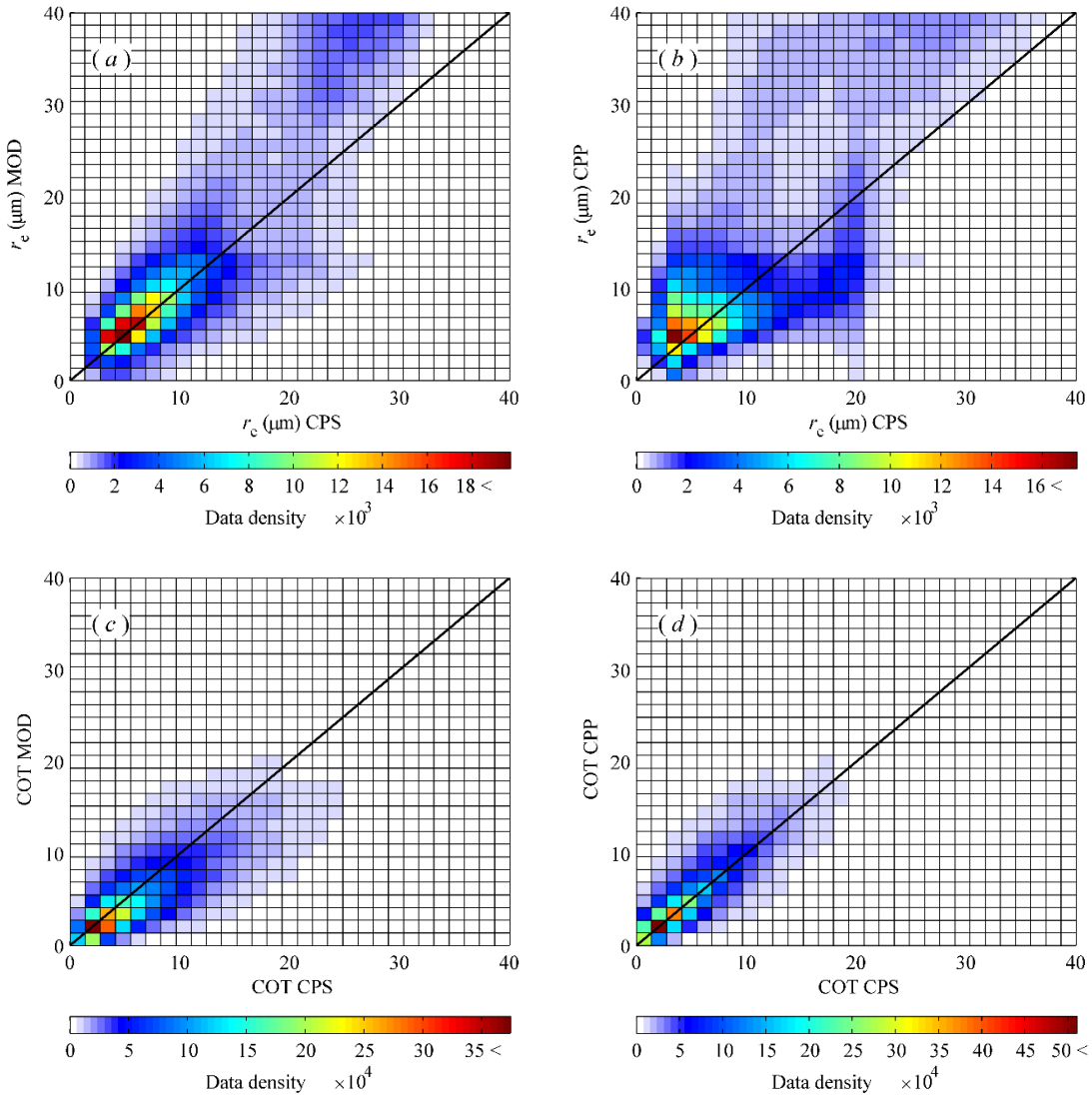

FIGURE 4.5 Density scatter plots of r_e (a, b) and COT (c, d) obtained from CPS, CPP and MOD06_L2 for all data (22 SEVIRI images). These data correspond to averaged values in a regular grid of 0.05º × 0.05º considering all clouds (water plus ice clouds) in each grid cell. The black line represents the 1:1 relation.

MODIS with a higher spatial resolution is able to identify smaller cloudy or clear sky scenes, consequently for fractional cloud cover regions the TOA reflectances at different spatial resolutions may be considerably different resulting in COT differences between two sensors observing the same scene (Zeng et al. 2012). Cloud classification is another important factor to be considered when analysing the results. Pixel by pixel comparisons between the cloud classification used in CPS and in the CPP cloud phase

product showed that both algorithms classify 86.3% of the pixels as clouds and in 72.5% of the cases they agree with the classification (water or ice). Overall results show a good agreement between the method applied and the well-established MOD06_L2 and CPP cloud product algorithms, with absolute bias lower than 2 (2 μm) for COT (r_e) and RMSE values lower than 10 (8 μm) for COT (r_e).

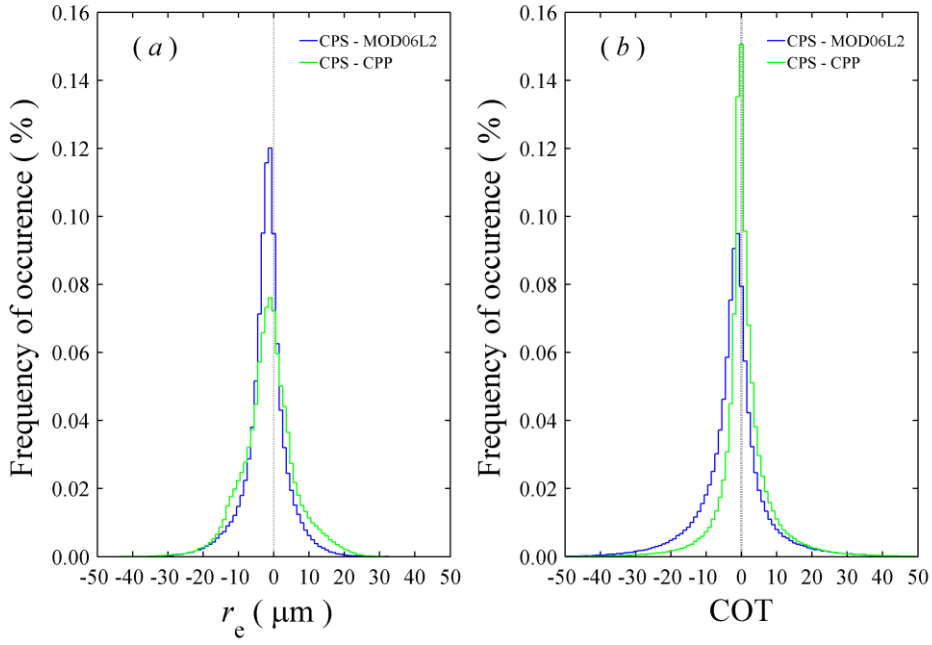

FIGURE 4.6 Histograms of the differences between CPS, CPP and MOD06L2 of r_e (a) and COT (b) mean values. These results are for all clouds (water plus ice clouds) in each grid cell of 0.05º × 0.05º using the data of the 22 SEVIRI images considered for the comparisons.

4.3.2 Cloud effects on the SW radiation at the surface

In this section, the cloud radiative effects at the surface are related with the cloud quantities retrieved with CPS method over Évora region for an area of 0.2° × 0.2° centred in the geographic coordinates of the ICT observatory. This area was chosen because is representative of the characteristics of the Évora site in terms of cloud extension and radiative properties of the surface (Salgueiro et al. 2016). For this purpose, daytime hourly images of SEVIRI covering the study site were collected from January to December 2015. Only cases of cloud contamination (all cloud situations in terms of type and fraction) and of solar zenith angles lower than 70° were selected, yielding a total of 603 images distributed by 124 days (30 days in winter, 34 in spring, 21 in summer and 39 in autumn). The CPS method was applied to obtain the COT and

the droplet effective radius/particle size at the cloud tops for the selected images. These retrieved quantities were then used to derive the cloud water path (CWP; g m^{-2}) using equation (4.4) (Stephens 1978), where ρ is the water/ice density. CWP is referred as the vertical integral of cloud condensate, either for liquid clouds (LWP) or ice clouds (IWP). While COT is representative of the extinction of the whole cloud extension, the retrieved r_e is representative of the cloud tops. Thus, to relate the retrieved quantities with CRE_{SW} at the surface, the CWP is used since it allows for relating simultaneously both quantities, r_e and COT, with the cloud radiative effects. Since the satellite takes approximately 12 minutes to scan the entire disc, the CRE_{SW} are calculated 10 minutes after each hour, which roughly corresponds to the scanning time in the study area:

$$\mathrm{CWP} = \frac{2}{3} r_e(\mathrm{COT})\rho \qquad (4.4)$$

The SW radiative effects at the surface due to different types of clouds are presented for cases when water and ice clouds produce a surface cooling effect ($CRE_{SW} < 0$) over the study area. These cases were filtered to situations of fractional sky covers (F_{sc}) higher than 0.8, which was considered the lower limit for overcast situations. The F_{sc} was calculated as the ratio between the number of cloudy pixels and the number of total pixels that constitute the study area. This resulted in 79 ice and 112 water cloud situations. The variation of the CRE_{SW} at the surface with the IWP and LWP (average over the study area) is represented in figure 4.7 (a, b) for different solar zenith angle ranges. In general, water clouds present lower values of LWP (less than 400 g m^{-2}) than ice clouds that present maximum values of IWP around 700 g m^{-2}. Since CWP is obtained from the retrieved cloud parameters (COT and r_e), cases classified as ice clouds may correspond to clouds of vertical development with high COT values that represent all cloud extent. In addition, in these cases if r_e, representing the value in cloud tops, is higher than the mean r_e of the cloud, the IWP can be overestimated justifying the high values showed in figure 4.7 (a, b). Nevertheless, the magnitude of the CRE_{SW} produced by water clouds is of the same order or higher than ice clouds. The different fittings of the data, although with dispersion, show the tendency of water clouds to produce more negative CRE_{SW} than ice clouds for a same value of CWP and this effect is more pronounced for higher solar zenith angles due to the longer atmospheric path made by radiation. The results shown in figure 4.7 (a, b) suggest that

water clouds are responsible for a higher CRE_{SW} efficiency than ice clouds. These results also show that the available sunlight is an important factor determining the CRE_{SW} (Boucher et al. 2013). Shupe et al. (2008) also demonstrate that for mixed-phase clouds, there is a strong radiative dominance of cloud liquid water over ice clouds.

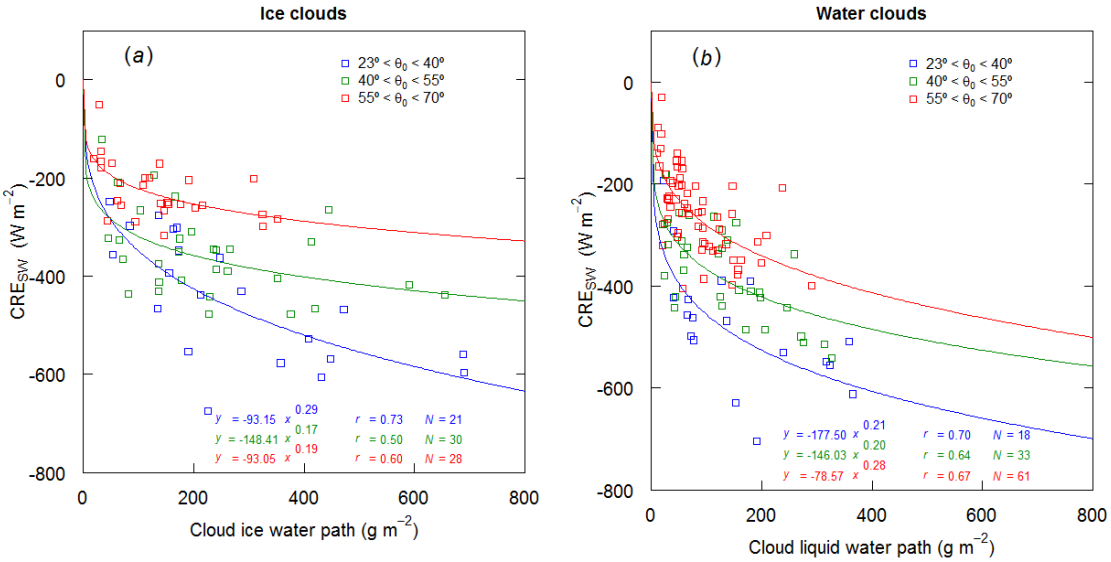

FIGURE 4.7 Variation of the CRE_{SW} at the surface with the IWP (a) and LWP (b) for cloud fractions greater than 0.8. The data take different colour according with the solar zenith angle range where they fall; N is the number of data and r is the correlation coefficient.

The cloud radiative effects on solar radiation can be also expressed in terms of the cloud modification factor (CMF), which is used to characterize the attenuation of radiation by clouds. CMF is defined as the ratio between the measured SW irradiance under cloudy conditions and the estimated SW irradiance in clear sky conditions, considering that all other atmospheric conditions are kept the same as in the actual measurement (Calbó et al. 2005). In general, CMF assumes values lower than the unit. However, there are situations known as enhancement events in which the levels of SW radiation reaching the surface in cloudy conditions are higher than the levels in its corresponding clear sky conditions (Piedehierro et al. 2014). Figure 4.8 shows the variation of the CMF at the surface with the COT (average over the study area) for different fractional sky covers considering the complete set of data (603 images). It can be observed that the CMF decreases approximately exponentially as COT increases, which is more evident for F_{sc} values higher than 0.6, although with dispersion of the data. Similar results were found for solar ultraviolet radiation under overcast conditions

by Antón et al. (2012). Most of the COT mean values are lower than 15, which is in agreement with the results obtained by Salgueiro et al. (2016) for Évora site using ground-based data. For small values of F_{sc}, corresponding to COT lower than 10, the CMF factor presents a large variation spanning from reductions in the SW radiation of the order of 80% (CMF=0.2) to enhancements larger than 30% (CMF=1.3), showing that the SW radiation at the surface is very sensitive to changes in clouds translated here by the COT variation. Yet, there are other cases in which CMF takes the value of approximately 1 meaning that clouds have an equivalent effect to clear sky conditions in the SW radiation that reaches the surface due to multiple scattering by cloud particles.

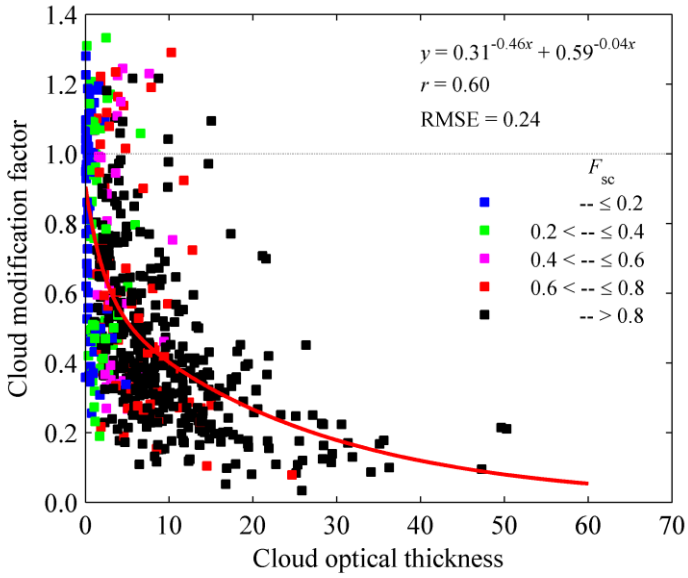

FIGURE 4.8 Variation of the experimental cloud modification factor with COT for several fractional sky cover (F_{sc}) values over Évora region.

Although the enhancement events generally occur for relatively low COT values, they are observed for all F_{sc} situations including F_{sc} higher than 0.8 (overcast). These events occurring for high F_{sc} situations are probably related to differences in the F_{sc} value derived from cloud classification by satellite and the true conditions at a sub-pixel scale. Since the enhancements events occur mostly when there is a broken cloud field in the sky without a concrete value of cloud cover (Piedehierro et al. 2014), the enhancement events corresponding to F_{sc} higher than 0.8 in figure 4.8 may, therefore, correspond to broken cloud field conditions. These broken cloud fields appear as homogeneous fields of thin clouds at the SEVIRI resolutions (Roebeling et al. 2006),

while using ground-based sky camera images these fields are shown either as cloud free or as broken clouds.

4.3.3 Analysis of a case study

To deepen the analysis of these enhancement situations corresponding to $F_{sc} > 0.8$, a day case study (11 June 2015) was selected illustrating also the importance of taking advantage of the 15-minute temporal frequency of Metetosat. Images from an all-sky camera installed at the same site were used to check the cloud cover conditions and are shown for two different times [figure 4.9 (a, b)]. Figure 4.9 (c) represents the daily series of the SW irradiances at the surface on 11 June 2015: global (tsw), direct (dir) and diffuse (dif) measurements, as well as clear-sky (csw) obtained from the empirical clear sky method proposed by Long and Ackerman (2000) (subsection 4.2.2). The corresponding shortwave cloud radiative effects at the surface, CRE_{SW}, are represented simultaneously with the daily evolution of LWP [figure 4.9 (d)] and with the daily evolution of COT [figure 4.9 (e)]. Both LWP [figure 4.9 (d)] and COT [figure 4.9 (e)] derived from satellite retrievals have SEVIRI time resolution (15-minute). Note that the clouds presented over the Évora area on 11 June 2015 were classified as water clouds. It is observed that in the morning period the measured SW global irradiance, governed by its diffuse component, is always lower than the clear sky irradiance and the corresponding CRE_{SW} is always negative. The sky camera image taken at 09:10 UTC shows overcast sky conditions [figure 4.9 (a)], which are in accordance with $F_{sc} = 1$ derived from the corresponding satellite image. In the afternoon, the oscillations of the SW global irradiance between high and low values is characteristic of a broken cloud field and in certain cases the global irradiance exceeds the clear-sky irradiance producing enhancement events with positive CRE_{SW} values and CMF higher than 1. In this situation, the sky camera image at 15:10 UTC [figure 4.9 (b)] shows that the true conditions are a broken cloud field with a cloud fraction lower than 0.85 responsible for the enhancement event observed at that time, while F_{sc} derived from the satellite image assumes values higher than 0.9.

Figure 4.9 (d) shows the daily evolution of the LWP (left axis) and the corresponding CRE_{SW} (right axis). The red line represents the SEVIRI LWP obtained from the satellite COT and r_e retrievals and using equation (4.4), while the blue line represents the LWP obtained from the microwave radiometer ground-based

measurements (RPG LWP). The surface measurements of the LWP were averaged for the correspondent 15 minutes of the SEVIRI LWP. The error bars represent the spatial variability of the SEVIRI LWP calculations (red error bars) in the study area (0.2° × 0.2°) and the temporal variability over the 15 minutes for RPG LWP measurements (blue error bars). The results show that both LWP lines have a similar pattern and in some cases, they are almost coincident with maximum values in the morning and lower values in the afternoon. Although the two approaches (satellite retrievals and microwave radiometer measurements) refer to two distinct surfaces, the satellite is looking at the top of the clouds and the microwave radiometer is looking at the bottom of the clouds, the matching of the LWP results is good, evidencing a remarkable LWP closure and showing that it is indeed possible to study clouds from the combined use of satellite and ground based measurements. The retrieved COT [figure 4.9 (e)], with the error bars representing the spatial variability in the area considered, exhibits the same pattern as the LWP lines with maximum values during the morning period and lower values in the afternoon. The daily evolution of the cloud quantities, LWP and COT, agrees with the CRE_{SW} evolution as shown in the right axes of figure 4.9 (d, e). In the morning period, more negative values of CRE_{SW} are produced due to higher values of LWP and COT while in the afternoon the opposite situation is observed. In the afternoon, positive CRE_{SW} values are observed corresponding to the enhancement events, which occur when global irradiance exceeds the clear-sky irradiance, as shown in figure 4.9 (c). The observed enhancements are typical cases of positive cloud effects as discussed in the original paper of Long and Ackerman (2000). This enhancement effects occur because in the presence of a broken cloud cover (e.g. cumulus or broken stratus) the diffuse component enhances with respect to clear-sky situations due to the increase of scattering (compared to molecular scattering prevailing in clear-sky situations) by the cloud edges. Therefore, the total component results greater than in the clear-sky situations. This is recognized as a local effect in space and time, for example, when averaged in time, clouds are expected to reduce incoming radiation at the surface.

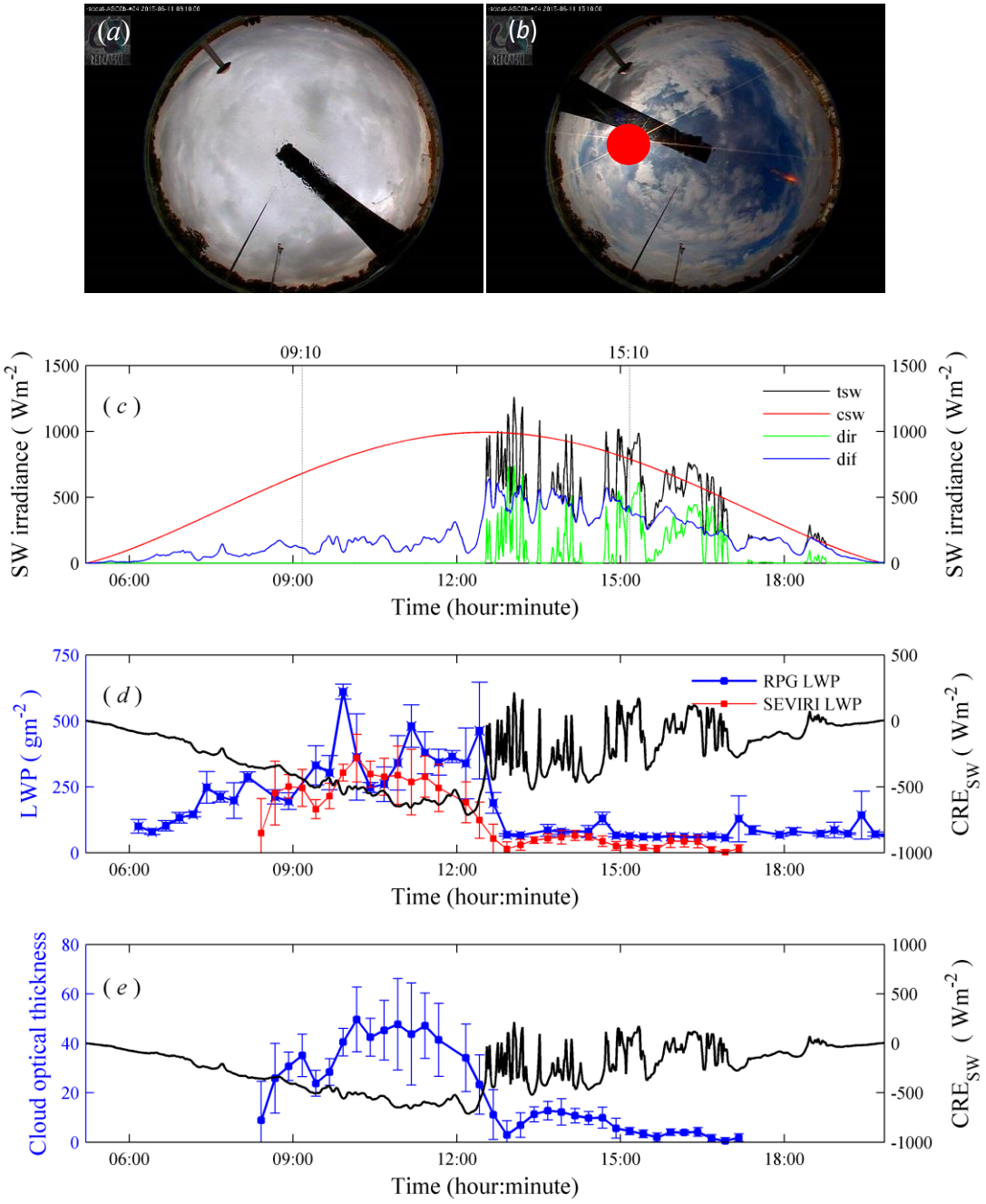

FIGURE 4.9 Sky camera images obtained on 11 June 2015 at 09:10 UTC (a) and at 15:10 UTC (b); (c) daily temporal series of SW irradiance, where tsw is the global irradiance, csw is the clear sky irradiance, dir is the direct irradiance and dif is the diffuse SW irradiance; (d) daily temporal series of CRE_{SW} and LWP obtained from surface microwave radiometer measurements (RPG LWP) and from SEVIRI derived data (SEVIRI LWP); (e) daily temporal series of CRE_{SW} and COT.

4.4 Summary and conclusions

The main purpose of this work was to use SEVIRI reflectance measurements to obtain cloud parameters and study the relation between these quantities and the cloud radiative effects at the surface in Évora region. The CPS method used to retrieve the cloud parameters, COT and r_e, is based in the principle of using reflectances in non-absorbing (0.6 μm) and in absorbing (3.9 μm) wavelengths. A sensibility analysis of simulated retrievals to input parameters (cloud top height, surface albedo and aerosol optical thickness) demonstrated that these parameters are important factors in COT and r_e retrievals with large uncertainties around 10 % for small values of COT and r_e. It was also demonstrated that for water clouds the uncertainties related to cloud top height can be greater than 10 % for small values of r_e. The uncertainties found related with geometry are around 3 %. The CPS was tested for a set of 22 images and the obtained COT and r_e were compared with the corresponding MOD06_L2 (based on MODIS measurements) and CPP (based on SEVIRI measurements) cloud products. This comparison was done in terms of average values in a longitude-latitude grid of 0.05º × 0.05º showing that more than 80 % (82 %) of the absolute differences between COT (r_e) mean values are centred in the range from ±10 (±10 μm) considering all clouds (water plus ice clouds) in each grid cell. In general, the obtained COT (r_e) exhibit a tendency to slightly underestimate (underestimate) the MOD06_L2 COT (r_e) and to overestimate (underestimate) the CPP COT (r_e).

The CPS, able to characterize the cloud field in terms of COT and r_e evolution, was used to retrieve COT and r_e of the hourly images over Évora region during 2015. The CWP obtained from COT and r_e satellite retrievals and the COT were related with the CRE_{SW} and CMF. The relation between CWP and CRE_{SW} for F_{sc} greater than 0.8, considered as overcast conditions, revealed that the liquid water clouds exhibit a tendency to produce more negative CRE_{SW} than ice clouds. This behaviour was more pronounced for high solar zenith angles. The CMF, translating the attenuation of radiation by clouds, exhibited approximately an exponential decrease with COT increasing for high fractional sky covers. It was found that for low fractional sky covers, the CMF presents a large variation with reductions of 80 % and enhancements of 30 % of the SW radiation for small COT values (<10). Yet, this relation between the CMF and the COT revealed that some enhancement events are included in situations classified as overcast (F_{sc}>0.8). Some enhancement events occurring for F_{sc}>0.8 were

analysed in a case study using ground-based sky camera images. This allows to conclude that certain situations classified by satellite with high F_{sc} values (>0.9) are situations of broken clouds, ideal to produce radiation enhancements at the surface. Yet, the evolution of the cloud parameters (LWP and COT) obtained from satellite measurements is in good agreement with the CRE_{SW} evolution obtained from surface measurements and the SEVIRI LWP follows the same tendency as the LWP obtained from ground-based measurements. This also shows the very good LWP closure attained and shows the importance to combine satellite data with surface measurements to study clouds and their radiative effects.

Acknowledgements

This work was financed through FCT (the Portuguese Science and Technology Foundation) grant SFRH/BD/88669/2012. The work is co-funded by the European Union through the European Regional Development Fund, included in the COMPETE 2020 (Operational Program Competitiveness and Internationalization) through the ICT project (UID / GEO / 04683/2013) with the reference POCI-01-0145-FEDER-007690 and also through the ALOP project (ALT20-03-0145-FEDER-000004). METEOSAT imagery was kindly made available by EUMETSAT Data Centre Online Ordering (https://eoportal.eumetsat.int). The MODIS Cloud product was acquired from the Level-1 & Atmosphere Archive and Distribution System (LAADS) Distributed Active Archive Center (DAAC), located in the Goddard Space Flight Center in Greenbelt, Maryland (https://ladsweb.nascom.nasa.gov/). This work also made use of data from EUMETSAT Satellite Application Facility on Climate Monitoring (CM SAF) obtained from the web user interface (https://wui.cmsaf.eu). Thanks are due to Chuck Long (NOAA affiliated) that provided short wave clear identification and cloud cover analysis programs.

5 WARM CLOUD AND AEROSOL PROPERTIES OVER THE AZORES

5.1 Introduction

Aerosols, of natural or anthropogenic origin, may serve as cloud condensation nuclei upon which cloud droplets form. Because of their relationship, changes in aerosols may lead to changes in properties of clouds. For a constant liquid water path, an increase in aerosol amounts may cause an enhancement of the cloud droplet number concentrations and a reduction in the cloud drop sizes, resulting in a high cloud reflectance and increased optical depth. This effect is referred as cloud albedo effect (Twomey 1974, 1977). Aerosol-cloud interactions (ACI) are yet one of the major sources of uncertainty in estimating the magnitude of the radiative forcing (Myhre et al. 2013), and thus understanding these interactions is essential to increase the level of understanding and confidence of future climate projections.

ACI can be defined using different cloud microphysical variables [e.g. cloud optical depth (COD), cloud droplet effective radius (r_e) and cloud droplet number concentration (N_d)] and aerosol proxies [e.g. cloud condensation nuclei concentration (N_{CCN}) and light scattering coefficient and aerosol index]. ACI can be written as follows (Feingold et al. 2001):

$$\mathrm{ACI_{COD}} = \frac{\partial ln\mathrm{COD}}{\partial ln\alpha}\Big|_{\mathrm{LWP}} \tag{5.1}$$

$$\mathrm{ACI_{re}} = -\frac{\partial lnr_e}{\partial ln\alpha}\Big|_{\mathrm{LWP}} \tag{5.2}$$

$$\mathrm{ACI_{Nd}} = \frac{\partial ln\mathrm{N_d}}{\partial ln\alpha} \tag{5.3}$$

Where α is an aerosol proxy. The $\mathrm{ACI_{COD}}$, $\mathrm{ACI_{re}}$ and $\mathrm{ACI_{Nd}}$ are theoretically bounded by 0 – 0.33, 0 – 0.33 and 0 – 1 respectively, reaching the maximum absolute values if all aerosol particles are activated to droplets (McComiskey et al. 2009).

Different studies have been made to quantify and investigate the variability of the aerosol-cloud interactions in low-level liquid water clouds (e.g. Feingold et al. 2003; McComiskey et al. 2009; Sarna and Russchenberg 2016; Painemal and Zuidema 2013;

Painemal et al. 2015; Painemal et al. 2017). For example, McComiskey et al. (2009) examined the ACI at Pt. Reyes (California, US) for non-precipitating coastal stratus clouds, focusing on the variability of natural drivers (activation and collision-coalescence, aerosol size distribution, updraft velocity and adiabaticity) and uncertainty in ACI measurements from ground-based remote sensing observations. Painemal et al. (2015) used *in situ* aerosol measurements from ship transects between California and Hawaii taken during the Marine ARM GPCI Investigation of Clouds (MAGIC) campaign, combined with satellite [Fifteenth Geostationary Operational Environmental Satellite (GOES-15)] and with numerical model outputs to investigate the circulation patterns that modulate the synoptic and monthly variability of cloud condensation nuclei in boundary layer. Later, Painemal et al. (2017) estimated the ACI for spring-summer season using N_d retrievals from the GOES-15 and from the Moderate Resolution Imaging Spectroradiometer (MODIS) combined with MAGIC *in situ* aerosol measurements.

In the last chapters, different methods based on ground-based and satellite measurements were applied to retrieve the cloud optical depth over Évora site (38.57° N, 7.9° W), which is representative of an inland mid-latitude region located about 100 km east from the Atlantic Ocean. In this chapter, another remote sensing method to retrieve COD, as well as other cloud properties, is applied. Here, the retrievals are made for the Eastern North Atlantic site (ENA), established in 2013 by the U.S. Department of Energy Atmospheric Radiation Measurement (ARM) Climate Research Facility, and located on Graciosa Island (39.09° N, 28.02° W) in the Azores archipelago. Graciosa, with an area of approximately 60 km^2, represents a maritime pristine region, and thus with distinct cloud conditions from Évora. ENA site provides valuable information on marine boundary layer clouds, where the cloud occurrences are in the order of 60 – 80 % with a summertime minimum (Rémillard et al. 2012). Boundary layer clouds are the most frequently observed cloud type in Azores (40 - 50 %), with most prevalent types: shallow cumulus (20 %), cumulus under stratocumulus layers (10 – 30 %), and single-layer stratocumulus (10 %) (Rémillard et al. 2012). Due to its geographic location and cloud conditions, Azores archipelago offers good opportunities to perform studies on clouds and aerosol-cloud interactions (Rémillard et al. 2012; Wood et al. 2015; Sarna and Russchenberg 2016). CAP-MBL (Clouds, Aerosols and, Precipitation in the Marine Boundary Layer) ARM deployment at Graciosa Island was a 21-month field campaign

(Wood et al. 2015) that allowed to gather an extended record of cloud and aerosol properties, and meteorological data. Rémillard et al. (2012) studied the MBL clouds in terms of their occurrences and precipitation using data from the ARM program deployment. Two cases studies also selected from ARM deployment data set were used by Sarna and Russchenberg (2016) to present a method to determine values of ACI.

Here, we investigate the effect of aerosols on non-precipitating water clouds from ground-based measurements taken at ENA site during the years 2014 – 2015. The set of ACI metrics described previously is used to quantify the aerosol effect. First, the instruments and measurements, as well as the cloud properties (COD, r_e and N_d) retrieval methodology are presented. This is followed by the results obtained for cloud properties, as well as ACI_{COD}, ACI_{re} and ACI_{Nd}, which are compared with results from other studies. Finally, the main results are summarized. The work described here started during a 3-month stay at the University of Reading, and it is presently work in progress. Thus, it is foreseen that a more complete analysis of this work will be published.

5.2 Data and Methods

5.2.1 Instruments used and data

The cloud and aerosol properties analysed in this work were obtained from a set of instruments, summarized in table 5.1. All the instruments are installed at the ENA site. The Micropulse Lidar (MPL) and the Multifilter Rotating Shadowband Radiometer (MFRSR) are both used for cloud optical depth retrievals as described in the next subsection. MPL operates at a wavelength of 532 nm recording backscatter signals every 10 s from 150 m to 18 000 m with 15 m vertical resolution and an uncertainty of ±2%. The MFRSR performs hemispherical measurements of global and diffuse components of solar irradiance at six narrowband channels centred at wavelengths 415, 500, 615, 673, 870, and 940 nm with a 20-s time resolution. A 3-channel microwave radiometer (MWR3C) centred at 23.834, 30 and 89 GHz is used to measure the liquid water path, with an uncertainty of 15 g m^{-2}. The cloud base height was obtained from a Vaisala ceilometer (model CL31), which detects up to three cloud layers simultaneously. The Vaisala ceilometer measures the backscattered light intensity at 910 nm as function of distance, allowing to determine the cloud base heights above ground level and below 7700 m with 10 m resolution and an uncertainty of 5 m. A YES Total Sky Imager (TSI) Model TSI-660 was used to check the sky conditions. The TSI

provides time series of hemispheric sky images during daylight hours at 30-s sampling interval. The cloud condensation nuclei concentration is measured with a Droplet Measurement Technologies CCN counter every second, and cycling every hour for different values of supersaturation (0.0, 0.1, 0.2, 0.5, 0.8 and 1.0%). An Integrating Nephelometer is used to measure the aerosol light scattering coefficient. The Nephelometer performs measurements at three wavelengths of 450, 550 and 700 nm oscillating between 1 and 10 μm size cut particle diameters at 30-s time resolution.

TABLE 5.1 Instruments installed at ENA site and used to obtain cloud and aerosol properties.

Instruments	Estimated/measured quantity
Micropulse Lidar (MPL)	Cloud optical depth (COD_{MPL}) (Chiu et al. 2007)
Multifilter Rotating Shadowband Radiometer (MFRSR)	Cloud optical depth (COD_{MFRSR})
Microwave radiometer 3 channel (MWR3C)	Liquid water path (LWP; g m^{-2})
Ceilometer (Vaisala CL31)	Cloud base height
YES total sky imager (model TSI - 660)	Hemispheric sky images
CCN counter (Droplet Measurement Technologies)	Cloud condensation nuclei concentration (N_{CCN}; cm^{-3}) at 0.5% supersaturation
Integrating Nephelometer (TSI model 3563)	Aerosol scattering coefficient (σ_s; Mm^{-1}) at 550 nm

5.2.2 Cloud properties retrievals

The method used here to retrieve the cloud optical depth is based on solar background signals of the MPL, and was proposed by (Chiu et al. 2007). The solar background light of MPL, in units of photon counts, is a source of noise for measured returned backscattered laser light. When Lidar is pointing straight up, the solar background signal is the solar zenith radiance and can be calibrated using the principal plane measurements from AERONET (Chiu et al. 2007).

The MPL calibrated solar radiance is compared with computed look-up tables to retrieve the cloud optical depth (COD_{MPL}). Look-up tables are fully described in (Chiu et al. 2014). The solar radiance increases with optically thin clouds due to increase of scattering, and decreases with optically thick clouds due to the attenuation increase. Due to this non-monotonic relationship between COD_{MPL} and the solar zenith radiance, the

algorithm provides two values of COD_{MPL}, one corresponding to optically thin clouds and another to optically thick clouds. This COD_{MPL} ambiguity was not solved as described in (Chiu et al. 2014), but simply the thicker clouds were taken. Therefore, only the highest COD_{MPL} value was considered, which does not always correspond to the true cloud conditions observed, since sometimes there may be thinner clouds or clear-sky. To solve this issue, the COD_{MPL} for thick clouds is compared with the cloud optical depth retrievals from the MFRSR (COD_{MFRSR}) for solar zenith angles lower than 70°. The COD_{MFRSR} was retrieved using the MFRSR global transmittances at 415 nm combined with 1D radiative transfer calculations, like the method of Min and Harrison (1996). The transmittance is given by the ratio between the MFRSR measured irradiance and the corresponding quantity at the top of the atmosphere, which is determined using the Langley method. Because MPL and MFRSR instruments have different temporal resolutions, the COD_{MPL} and COD_{MFRSR} were averaged over 1-minute time periods. The COD_{MPL} is then selected using the COD_{MFRSR}. If COD_{MFRSR} is higher than 10 during at least 60 consecutive minutes indicating that the sky is overcast, the COD_{MPL} is selected otherwise it is excluded from the data set. The value of COD_{MFRSR} equal to 10 was arbitrarily chosen, but it avoids the condition of a large thick cloud in the MFRSR field-of-view while the rest of the sky is clear.

Figure 5.1 shows an example of the temporal evolution of the cloud optical depth from MPL signals, MFRSR transmittances at 415 nm, and AERONET cloud mode (Chiu et al. 2010) (level 1.0) on 23 May 2014. AERONET cloud optical depth is obtained from the sun photometers only when clouds block the Sun. The optical depth from the different approaches agrees well during the morning period when the cloud conditions are more homogeneous, which can be confirmed by the TSI images taken, for example, at 11:00 UTC and 13:00 UTC as figure 5.2 (a) and (b) show. After 13:30 UTC, the cloud optical depth from MPL assumes larger values than the cloud optical depths from MFRSR and AERONET cloud mode in several time periods, as for example around 15:00 UTC and 17:00 UTC when the homogenous cloud situation is not observed anymore [figure 5.2 (c) and (d)]. During these time periods, the COD_{MPL} retrievals for optically thick clouds do not represent the true cloud conditions observed, and thus these values of COD_{MLP} are excluded from the data set using the COD_{MFRSR} threshold value of 10 (blue traced line) after averaging the cloud optical depths on a 1-

minute basis. In situations like these, the COD_{MPL} corresponding to thin clouds should be the right solution.

Finally, since the aim of the work is the study of water clouds, a criterion to exclude ice clouds based on MPL, radio soundings and ceilometer data was applied. This criterion involves the cloud top height from MPL, the ceilometer cloud base height and the freezing level obtained from the daytime sounding launched at Graciosa typically at 11:30 UTC. The ice clouds associated with the measurements are those where the highest cloud top detected by MPL is above the freezing level. Because the cloud mask based on the MPL data is indeterminate for clouds below 500 m due to instrumental limitations (overlap effect), the ceilometer lowest cloud base height was used to address cases like these. To avoid precipitation, the data were selected using the microwave radiometer 3-channel (MWR3C) that contains information about the precipitation at the surface.

The effective radius (r_e) is estimated combining the measured liquid water path (LWP), the water density (ρ_w) and the COD_{MPL} using equation (5.4) (Wood and Hartmann 2006), which considers a linear increase of the liquid water content (LWC) from the cloud base to the cloud top, and a constant cloud droplet number concentration.

$$r_e = \frac{9}{5}\frac{\mathrm{LWP}}{\mathrm{COD_{MPL}}\rho_w} \qquad (5.4)$$

The COD_{MPL} retrievals are also combined with the measured LWP to estimate the cloud droplet number concentration (N_d) using the equation (5.5) as in McComiskey et al. (2009), under the same argument of linear LWC with respect to cloud height (i.e. clouds are considered adiabatic). In equation (5.5), the C(T, P) is a known function of cloud base temperature and pressure. Here, constant values were assumed for temperature and pressure of 288 K and 900 hPa respectively, resulting in a C(T, P) equal to 8.4718×10^{-5} $kg^{0.5}\,m^{-2}$.

$$N_d = \mathrm{C(T,P)}\mathrm{COD_{MPL}}^{3}\mathrm{LWP}^{-2.5} \qquad (5.5)$$

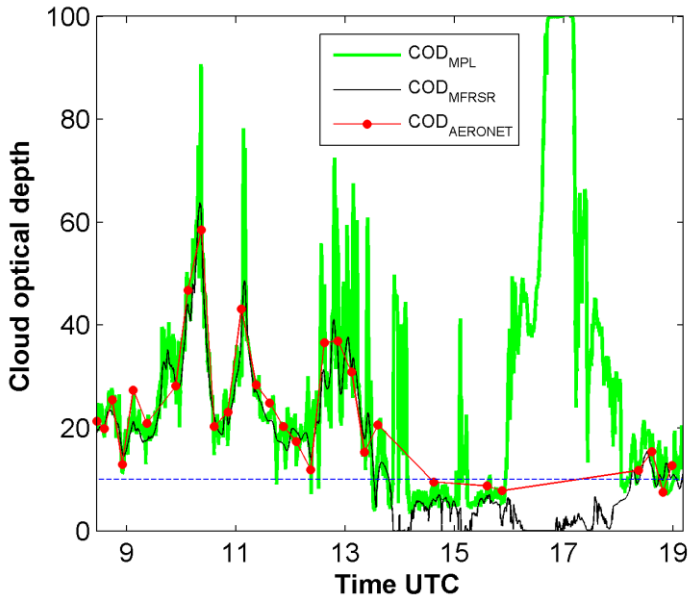

FIGURE 5.1 Time series of cloud optical depth on 23 May 2014 retrieved from solar background signals of micropulse Lidar (COD_{MPL}), transmittances at 415 nm from the multifilter rotating shadowband radiometer (COD_{MFRSR}), and AERONET cloud mode observations ($COD_{AERONET}$). The blue traced line represents the cloud optical depth threshold of 10 considered to select the COD_{MPL}.

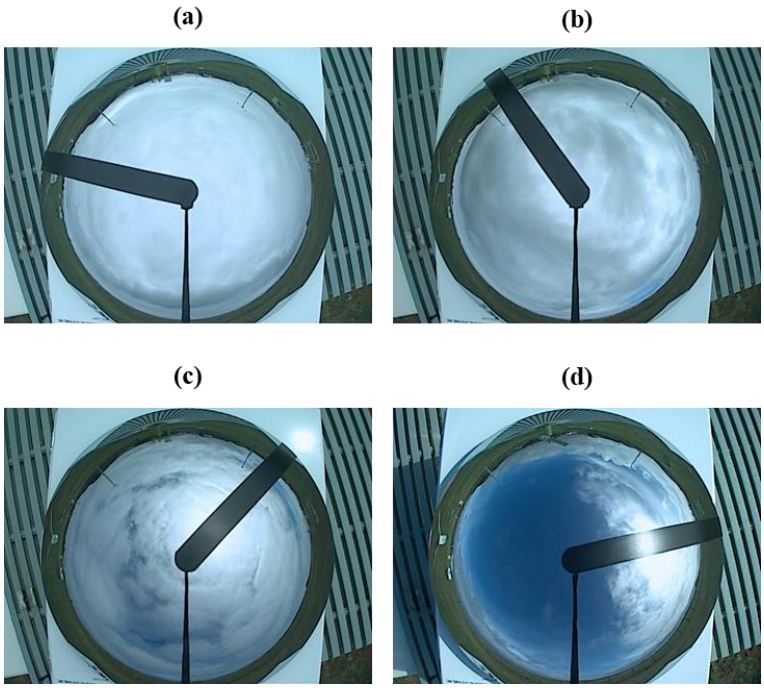

FIGURE 5.2 Sky camera images taken on 23 May 2014 at ENA site: (a) 11:00 UTC, (b) 13:00 UTC, (c) 15:00 UTC, and (d) 17:00 UTC.

5.3 Results of aerosol-cloud interaction measures

The 1-minute averaged COD_{MPL} is evaluated against COD_{MFRSR}. All data (one-minute basis) containing non-precipitating water clouds and effective radius between 3 and 100 µm, in the period of May 2014 until December 2015 are considered. This resulted in a total of 6367 data points (on a minute basis). Figure 5.3 shows the scatter plot (a) and the histogram (b) of the 1-minute average cloud optical depth retrievals from MPL background signals and MFRSR transmittances at 415 nm, corresponding to the 6367 data points. The scatter plot shows that COD_{MPL} slightly underestimates the COD_{MFRSR} with a bias of -1.25, and with cloud optical depth mean values of 27.7 and 28.9 for MPL and MFRSR respectively. The scatter plot also shows that, in general, the data are around the line 1:1 (black line), presenting some dispersion that increases for COD_{MPL} values larger than 40. A high correlation coefficient of 0.94 and a root-mean-square error of 5.6 between the two optical depth data sets were obtained. The differences between the two data sets of cloud optical depth retrievals can be likely because MFRSR performs hemispherical measurements while MPL performs zenith measurements, and thus MPL captures larger variations in clouds than MFRSR. Both the scatter plot and the histogram show a peak at the optical depth 15-20, and a discrepancy of bins 0-10 due to the COD_{MFRSR} threshold used for COD_{MPL} selection.

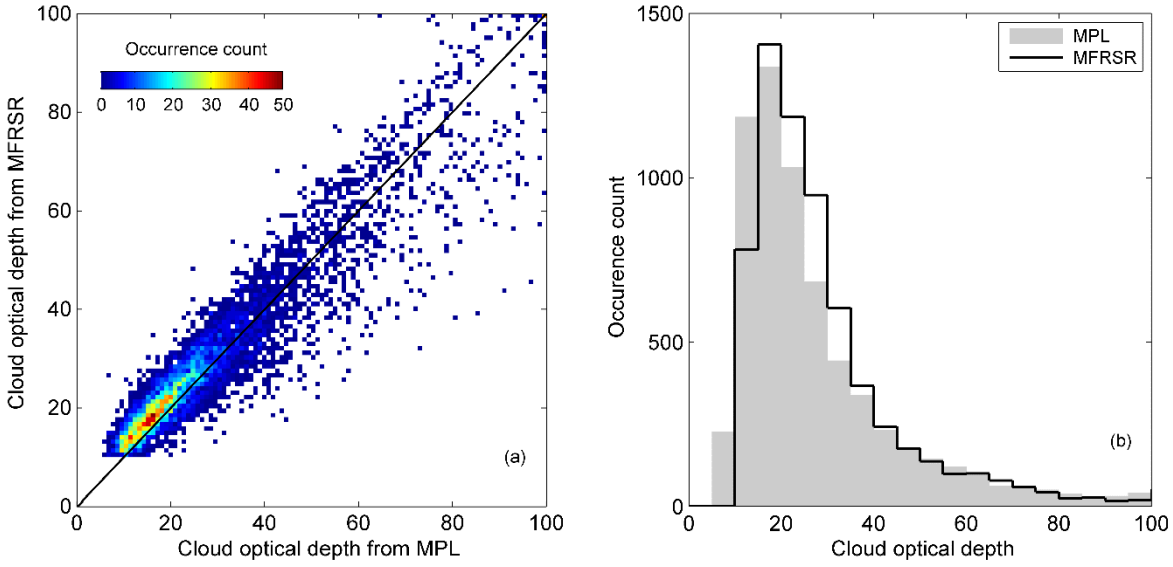

FIGURE 5.3 Scatter plot (a) and histogram (b) of the comparison between the 1-minute cloud optical depth retrievals from solar background signals of the micropulse Lidar (MPL) and from transmittances at 415 nm of the multifilter rotating shadowband radiometer (MFRSR). In (a), the black solid line represents the relation 1:1

The ACI (ACI_{COD}, ACI_{re} and ACI_{Nd}) were calculated from the equations 5.1 - 5.3, using the cloud retrievals (COD_{MPL}, r_e and N_d) and the N_{CCN} at 0.5% supersaturation as aerosol proxy. N_{CCN} was chosen as aerosol proxy because it is the aerosol property that is more linked to cloud droplet formation. Additionally, in stratocumulus clouds of well mixed boundary layers, the N_d throughout the whole depth of the cloud is almost equal to the N_{CCN} below cloud (Martin et al. 1994). The ACI were estimated for data corresponding to LWP values between 50 and 150 g m^{-2} as in McComiskey et al. (2009) to avoid very thin or broken cloud cover, as well as post precipitation conditions (LWP < 50 g m^{-2}), and bulk of precipitating clouds (LWP > 150 g m^{-2}). Applying the same thresholds as McComiskey et al. (2009) for our dataset led to 363 data points (1-minute basis).

Figure 5.4 (a – g) shows a time series of a set of aerosol and cloud properties obtained for 16 August 2015 as an example to illustrate the effect of aerosol on cloud microphysics. All properties (COD_{MPL}, LWP, r_e, N_d, CBH, N_{CCN} and σ_s) are at 1-minute resolution, and the clouds correspond to low clouds with base heights lower than 0.6 km above ground-level [figure 5.4 (e)]. The time series of N_{CCN} and σ_s [figure 5.4 (f - g)] are not continuous because the measurements of N_{CCN} are taken cycling for different values of supersaturations, and for σ_s the measurements are taken oscillating between 1 and 10 µm aerosol diameter size cut. The N_{CCN} values shown here were selected for supersaturations of 0.5 %. The period between 11:00 UTC and 12:00 UTC on 16 August 2015 (figure 5.4) illustrates well the effect of aerosols on cloud microphysics: although the accurate quantification of the albedo effect requires a constant LWP (Twomey 1974), which is not quite the case here since the LWP slightly decreases in this time period, an increase in N_{CCN} is accompanied by a decrease in r_e and an increase in N_d and in COD_{MPL}, which tracks well the LWP evolution. After 12:00 UTC these effects are not so pronounced as before. Still, between 12:00 and 13:00 UTC, a decrease of N_{CCN} corresponds to a decrease of N_d and an increase of r_e, while the LWP maintains approximately constant. Cases like the period between 11:00 and 12:00 UTC exhibit sufficient variability to quantify the ACI. The ACI are quantified here for the data set of non-precipitating water clouds described in the previously.

The frequency histograms of each variable used in ACI calculations are presented in figure 5.5 (a – e), where the error bar above the histograms represents the mean and the standard deviation of the corresponding property. The full data set (363 data points) is

used to obtain the ACI_{COD}, ACI_{re} and ACI_{Nd} values, which are shown in figure 5.6 (a – c). The ACI were obtained from the linear fitting of the logarithm of the cloud properties (COD_{MPL}, r_e and N_d) versus the logarithm of the N_{CCN}, with values for ACI_{COD}, ACI_{re} and ACI_{Nd} of 0.036, 0.027 and 0.086, respectively. The corresponding values of the coefficient of determination (R^2) are 0.004 (ACI_{COD}), 0.002 (ACI_{re}) and 0.002 (ACI_{Nd}). The R^2 values suggest the percentage of variability in cloud properties (COD, r_e and N_d) that can be explained by changes in aerosol concentrations. These results show that there is almost no dependence of cloud properties on aerosols for the data set considered.

Previous findings of ACI from ground-based observations at Graciosa Island for two cases studies of marine stratocumulus (Sarna and Russchenberg 2016) provided values of ACI_{re} ranging from 0.01 to 0.09 for bins of 10 g m^{-2} of LWP between 30 and 90 g m^{-2}, and values of ACI_{Nd} of 0.78 and 1.59 considering the full LWP range. The value for ACI_{re} obtained here is in the range of values obtained by Sarna and Russchenberg (2016) although with a lower value of R^2. Other findings also using ground-based observations (Feingold et al. 2003; Kim et al. 2008; McComiskey et al. 2009) present distinct ACI values from those obtained here, mainly in the case of ACI_{Nd}. Feingold et al. (2003) derived values for ACI_{re} between 0.02 and 0.16 for a set of seven cases studies of single-layer water clouds, using ground-based remote sensing data from Southern Great Plains (SGP) ARM site in Oklahoma (US), a rural continental site. Kim et al. (2008) also for ARM SGP site found values of ACI_{re} between 0.04 and 0.17 for continental stratus clouds for ARM SGP site using 3 years of data. McComiskey et al (2009) reported for non-precipitating coastal stratus clouds (California, US) ACI_{COD} between 0.09 and 0.14, ACI_{re} between 0.10 and 0.14, and a value of 0.48 for ACI_{Nd}.

As discussed in the previous paragraph, the ACI_{Nd} obtained is lower by one order of magnitude when compared with other findings from ground-based observations (Sarna and Russchenberg 2016; McComiskey et al. 2009). Painemal et al. (2015; 2017) used satellite observations combined with *in situ* measurements and reported ACI_{Nd} values larger than those obtained here as well. Painemal et al. (2015) obtained an ACI_{Nd} value of 0.9 using N_d retrievals from GOES-15 and *in situ* aerosol measurements collected during the MAGIC campaign, and Painemal et al. (2017) reported values for ACI_{Nd} of 0.88 (GOES-15) and 0.79 (MODIS) for spring-summer period also for MAGIC campaign. Comparisons with aircraft-based studies (Painemal and Zuidema 2013) also

reveal substantial differences in ACI magnitudes. Painemal and Zuidema (2013) using *in situ* and aircraft observations from VOCALS-Rex campaign (Wood et al. 2011) reported values of ACI_{COD} of 0.33 (for 70 -80 g m^{-2} bin of LWP) and 0.34 (for 50 – 60 g m^{-2} bin of LWP), and ACI_{Nd} of 0.92 estimated from 28 profiles performed during four research flights.

The independent findings mentioned before are based on different temporal and spatial resolutions, and provide values of ACI that are closer in magnitude between them than the values obtained here. Thus, resolution issues cannot justify the ACI obtained. A possible reason for these ACI values can be related with collision-coalescence process. McComiskey et al. (2009) showed that for clouds with LWP lower than 150 g m^{-2}, the ACI decrease with increasing LWP, which is accompanied by an increase in drop collision-coalescence and a reduction in N_d. This process of collision-coalescence likely obscures the magnitude of ACI associated with drop activation at the higher LWP. Rémillard et al. (2012), showed that amounts of LWP greater than 75 – 100 g m^{-2} are sufficient to produce drizzling conditions in stratocumulus, and the non-drizzling distribution peaks around 30 g m^{-2}, which is below the lower bound considered here for LWP (50 – 150 g m^{-2}). Thus, some cases of non-drizzling stratocumulus were probably excluded, and cases of drizzling clouds may exist in the considered data set. In conditions of drizzling clouds, highly variable ACI values may result because of the aerosol scavenging from the atmosphere. However, we do not have evidence at the moment if any of these processes may justify the results shown here, thus further investigation on this is needed.

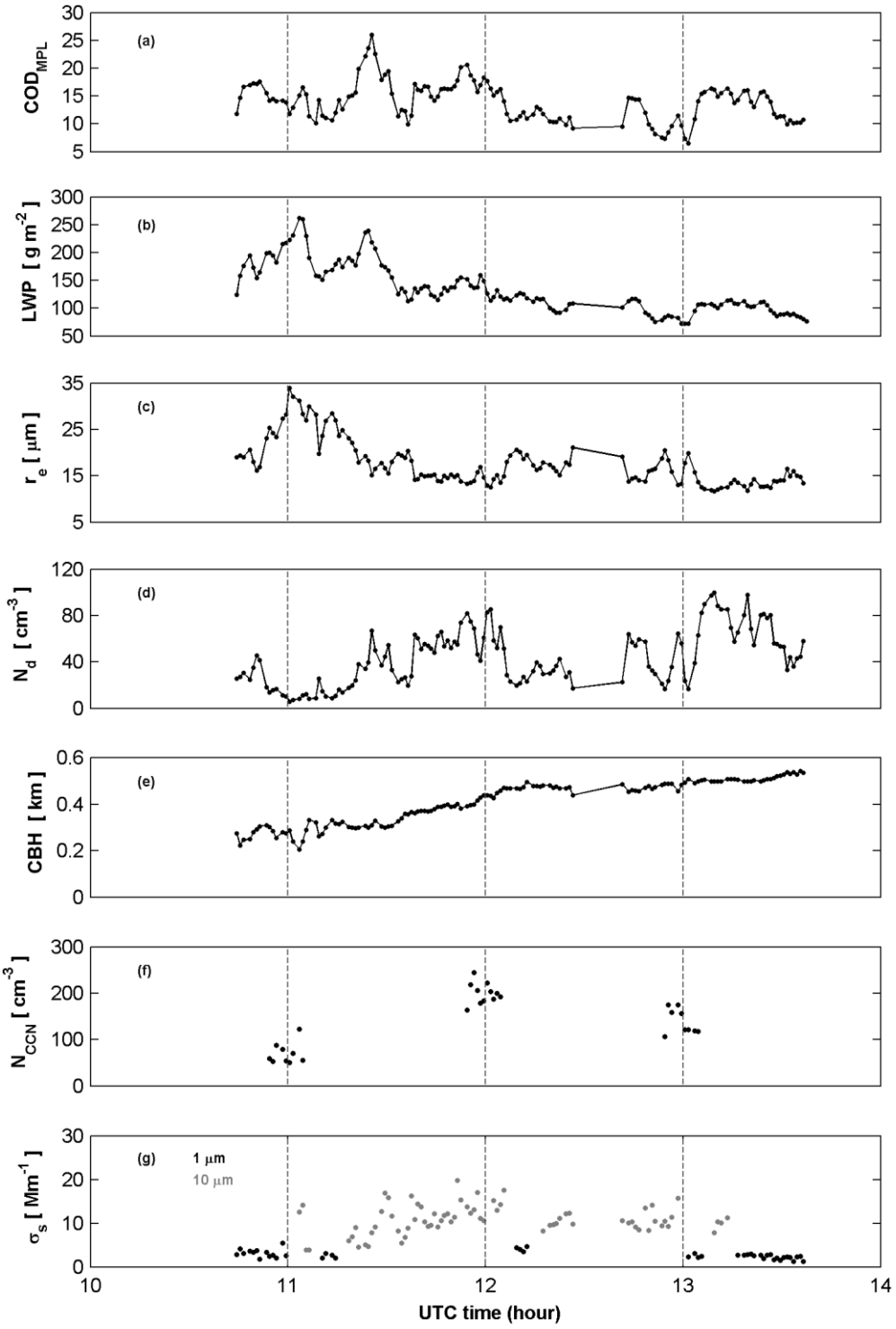

FIGURE 5.4 Time series on 16 August 2015 of (a) COD retrieved from MPL solar background signals, (b) LWP from the MWR3C, (c) r_e from the MPL and MWR3C (equation 5.2), (d) N_d from the MPL and MWR3C (equation 5.1), (e) cloud base height from Ceilometer, (f) N_{CCN} at SS = 0.5 from the CCN counter, and (g) total aerosol scattering coefficient at size cuts 1 and 10 μm from the nephelometer at ENA site. All data are averaged over 1 min time periods.

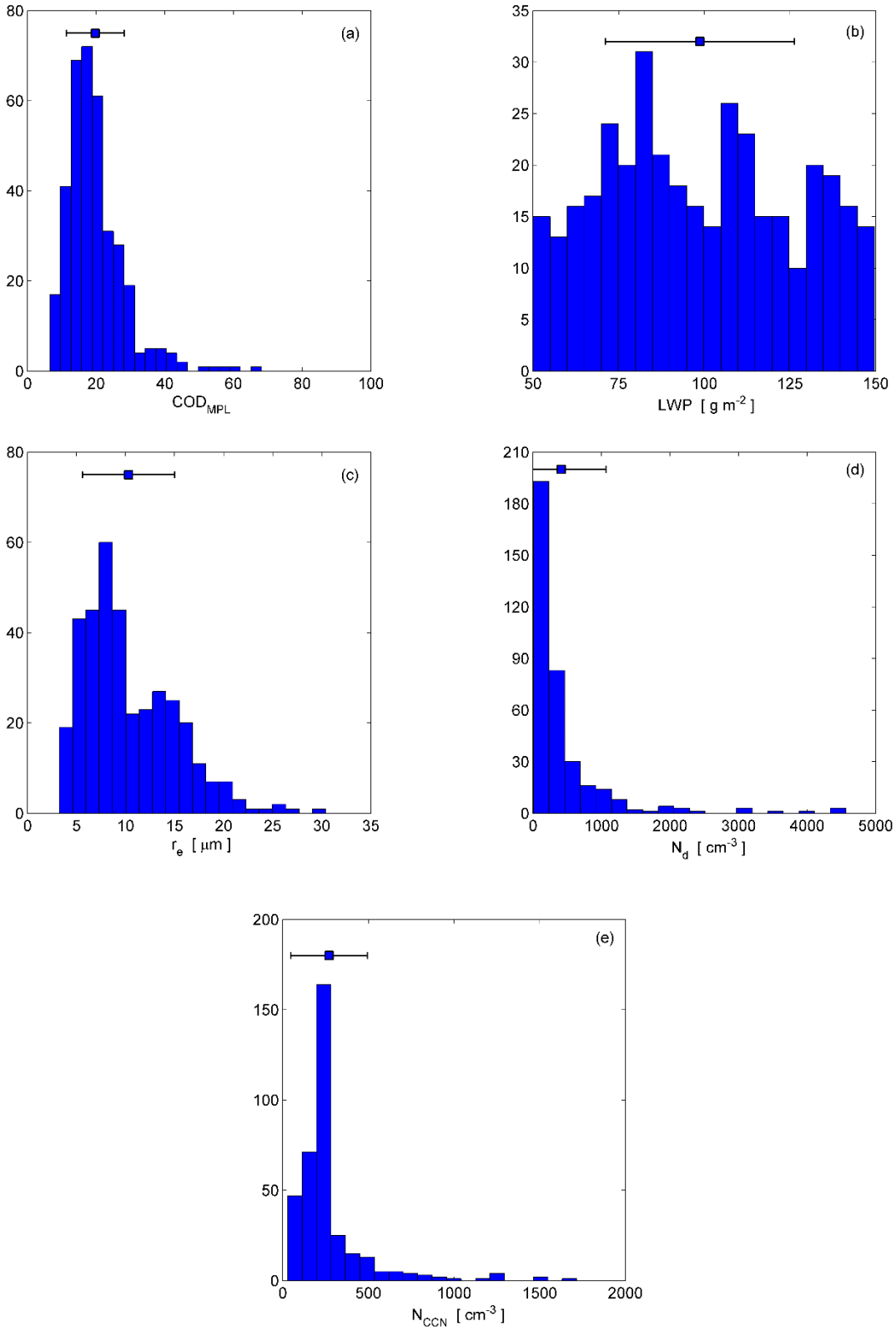

FIGURE 5.5 Histograms of the cloud and aerosol properties used in ACI calculations. The LWP was limited to the range from 50 to 150 g m^{-2} and N_{CCN} corresponds to 0.5 % of supersaturation.

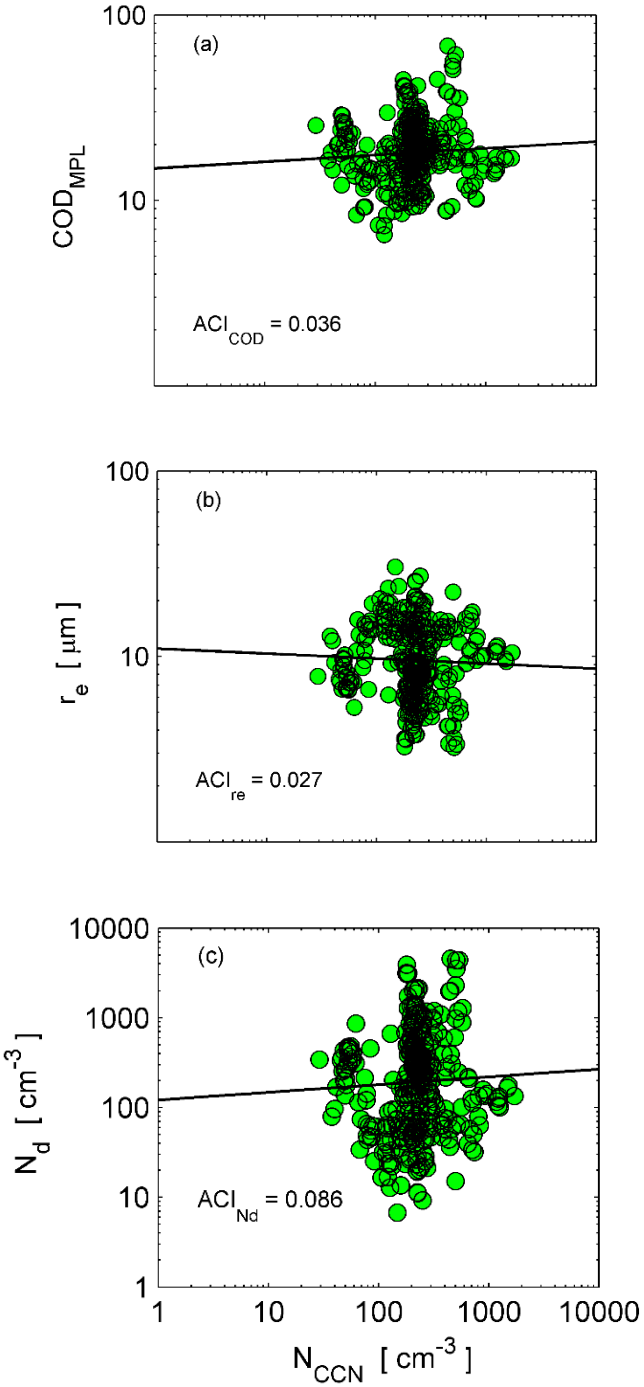

FIGURE 5.6 ACI results obtained from equations 5.1 – 5.3 for LWP ranging from 50 g m^{-2} to 150 g m^{-2}. All properties (COD_{MPL}, r_e, N_d and N_{CCN}) are at 1-minute basis. The N_{CCN} was selected for 0.5 % of supersaturation.

5.4 Summary

In this chapter, a remote sensing method based on MPL solar background signals (Chiu et al. 2007) is applied to retrieve the cloud optical depth from ground-based measurements taken at ENA site (Graciosa Island, Azores) during 2014 – 2015. These retrievals are used together with *in situ* measurements of liquid water path to estimate the corresponding cloud droplet number concentration and effective radius. The estimated properties, only for non-precipitating water clouds, are used together with aerosol *in situ* measurements to quantify the aerosol-cloud interactions.

The cloud optical depth retrievals from MPL are evaluated against the cloud optical depth obtained from MFRSR for non-precipitating water cloud cases. This results in a bias of -1.25 and a correlation coefficient of 0.94, and mean values of cloud optical depth of 27.7 and 28.9 for MPL and MFRSR, respectively. Qualitative comparisons between the cloud optical depth from MPL, MFRSR and AERONET cloud mode also show good agreement between the different data sets.

All data (cloud and aerosols at 1-minute temporal resolution) are selected based on LWP values between 50 and 150 g m^{-2}. For this range of LWP, the ACI are determined using the estimated cloud properties (COD_{MPL}, r_e and N_d) and the measured N_{CCN} at 0.5 % supersaturation, taken as aerosol proxy. The ACI values obtained from the selected data are 0.036 (ACI_{COD}), 0.027 (ACI_{re}) and 0.086 (ACI_{Nd}) with coefficients of determination between 0.002 and 0.004, translating a very low influence of aerosols on clouds. The obtained values for ACI are, in general, lower than ACI from other studies. This is more evident for ACI_{Nd} that presents always lower values by around one order of magnitude when compared with the independent ACI findings. Collision-coalescence process and potential drizzling clouds were indicated as potential reasons for the low ACI values. However, no evidence was found and the question remains. Thus, more work is needed to gain further insights into the reasons that may explain the obtained ACI for ENA site.

Acknowledgements

This work was financed through FCT (the Portuguese Science and Technology Foundation) grant SFRH/BD/88669/2012. I also acknowledge the University of Reading for the provided hosting facilities during my stay there. The data used in this chapter were obtained from the Atmospheric Radiation Measurement (ARM) Climate

Research Facility, a U.S. Department of Energy Office of Science user facility sponsored by the Office of Biological and Environmental Research.

6 CONCLUSIONS AND FINAL REMARKS

The work described in this thesis aimed to study the SW cloud radiative effects (CRE_{SW}) using temporal series of ground-based irradiance measurements taken in Évora, and to do the characterization of cloud properties (microphysical and optical) and of aerosol-cloud interactions using different remote sensing methods based on surface and satellite measurements. It was also aimed to study the relationships between the cloud properties retrieved with the different remote sensing methods used and the corresponding SW cloud radiative effects. These general objectives were achieved by accomplishing the specific objectives, described in the different chapters. The main conclusions of each chapter and how they lead to the next chapter are described following.

In the chapters 2 and 3, data sets of 7 years (2003 – 2010) of SW irradiance observations at Évora site were used to estimate the CRE_{SW}, and to retrieve the cloud optical thickness. These data sets were obtained from two different instruments that cover different fractions of the solar radiation spectrum: 300 – 1100 nm (MFRSR) and 285 – 2800 nm (Eppley pyranometer).

The second chapter was focused on the seasonal variability of the daily-mean CRE_{SW} for all-sky situations in terms of cloud type and fraction. The work described in this chapter allowed to conclude that the CRE_{SW}, with more negative values, is obtained from the Eppley pyranometer due to the larger range of its spectral band; moreover, the springtime values of CRE_{SW} present a larger variability with respect to the other seasons, which can be attributed to the higher variability found in cloud periods also for spring months. The work reported in this chapter attained the first specific objective proposed in this research.

From the second chapter, conclusions about the seasonal variability CRE_{SW} were made and its seasonal behaviour was related with the occurrences of cloud periods in Évora. To improve the understanding of the effect of clouds in attenuating SW radiation in Évora region, the effective cloud optical thickness (ECOT) was retrieved in chapter 3 using ground-based data and related with the corresponding CRE_{SW} obtained in chapter 2 for the same period. Thus, the seasonal variability of the ECOT was presented in chapter 3, as well the relationships between the ECOT of water clouds and the corresponding normalized CRE_{SW} ($NCRE_{SW}$) and $NCRE_{SW}$ efficiency. It was found that

the seasonal variability of the ECOT for all cloud conditions agrees with the seasonal variability of the CRE_{SW}. The relationships found between ECOT of water clouds and the corresponding $NCRE_{SW}$ showed that, in winter season a larger amount of radiation is attenuated with respect to the other seasons. It was also concluded that for high ECOT values, the $NCRE_{SW}$ efficiency becomes less sensitive to changes in ECOT of water clouds. The results obtained in chapter 3 allowed to attain the second objective of this thesis.

To improve and continue the study on CRE_{SW} and their relationship with the cloud properties, a method based on SEVIRI measurements was established and used in chapter 4 to retrieve the cloud properties (COT and r_e) over Évora region. This cloud characterization using SEVIRI measurements is related with CRE_{SW} from hemispherical measurements, complementing the work done in chapter 3 where the cloud characterization was obtained from ground-based data.

Thus, after comparing the satellite retrievals of cloud properties over the Iberian Peninsula with independent cloud products (MODIS and CPP from CM-SAF), it was concluded (chapter 4) that the proposed method performs well to characterize the cloud field in terms of COT and r_e, allowing for successfully reaching the third objective of this thesis. Moreover, the cloud properties retrieved from SEVIRI were also related to the CRE_{SW}, which was obtained from ground-based measurements taken at Évora site during 2015. The relation between the LWP, derived from the cloud properties retrievals, and the CRE_{SW} showed the tendency of water clouds to produce more negative CRE_{SW} with respect to ice clouds in overcast situations. Moreover, the COT retrieved from SEVIRI was related with the cloud modification factor allowing to detect enhancement events associated to satellite classified overcast situations, which are in fact situations of broken clouds (confirmed by the sky camera). A case study demonstrated the good agreement of the time evolution between the satellite retrievals (LWP and COT) and the CRE_{SW}, and allowed to obtain a good LWP closure between the LWP estimated from the satellite retrievals and the LWP measured at the surface. This allowed to attain the fourth objective of this thesis.

In the last year of this research, the opportunity to perform cloud studies using data measurements taken at the Eastern North Atlantic (ENA) site (Azores) came out, allowing to apply different remote sensing methods with respect to those used in chapters 3 and 4 for COT retrievals. Thus, the work described in chapter 5 was focused

on COT retrievals from solar background Lidar signals, and on the quantification of the aerosol-cloud interactions (ACI) at ENA site. Using the Lidar method, a good agreement was found between COT retrievals and the corresponding quantity obtained either from MFRSR ground-based measurements and from AERONET cloud mode data. The COT retrievals were used to estimate the ACI values, which revealed a low influence of aerosols on clouds. The ACI values found are about one order of magnitude lower than ACI from other studies, which needs further investigation. Nevertheless, it can be stated that the objectives proposed in chapter 5 were partially reached.

6.1 Suggestions for future work

The work developed in this thesis allowed to obtain a first climatology of the CRE_{SW} in Évora region, apply remote sensing methods to retrieve cloud properties, and compare the retrievals with CRE_{SW}. In the last part of this thesis (chapter 5), the aerosol-cloud interactions were assessed for Graciosa Island showing very low values when compared with other studies. Some reasons related with collision-coalescence process and precipitation were pointed out as possible explanations for the aerosol-cloud interactions results. Therefore, it is suggested to find evidence of the presented reasons to ensure that the obtained aerosol-cloud interactions values are valid for Graciosa Island.

The remote sensing techniques used in chapter 5 may be also applied to Lidar measurements taken at Évora site. Since Évora site is equipped with several instruments for cloud and aerosols observations (e.g. Vaisala Ceilometer, Microwave radiometer, Lidar Raman, Cimel sunphotometer, MFRSR, and Nephelometer), the aerosol-cloud interactions can be estimated and related with CRE_{SW} calculations contributing for improving the establishment of a cloud climatology in Évora region.

REFERENCES

Albrecht, B. A. 1989. “Aerosols, Cloud Microphysics, and Fractional Cloudiness.” *Science* 245 (4923): 1227–30. doi:10.1126/science.245.4923.1227.

Allan, R. P. 2011. “Combining Satellite Data and Models to Estimate Cloud Radiative Effect at the Surface and in the Atmosphere.” *Meteorological Applications* 18 (3): 324–33. doi:10.1002/met.285.

Anderson, G. P., S. A. Clough, and F. X. Kneizys. 1986. “AFGL Atmospheric Constituent Profiles (0 - 120km).” *Tech. Rep. AFGL-TR-86–0110*, Air Force Geophysics Laboratory, Hanscom Air Force Base, Mass, USA.

Antón, M., L. Alados-Arboledas, J. L. Guerrero-Rascado, M. J. Costa, J. C. Chiu, and F. J. Olmo. 2012. “Experimental and Modeled UV Erythemal Irradiance under Overcast Conditions: The Role of Cloud Optical Depth.” *Atmospheric Chemistry and Physics* 12 (23): 11723–32. doi:10.5194/acp-12-11723-2012.

Barker, H. W., and A. Marshak. 2001. “Inferring Optical Depth of Broken Clouds above Green Vegetation Using Surface Solar Radiometric Measurements.” *Journal of the Atmospheric Sciences* 58 (20): 2989–3006. doi:10.1175/1520-0469(2001)058<2989:IODOBC>2.0.CO;2.

Baum, B. A., and S. Platnick. 2006. “Introduction to MODIS Cloud Products.” *Earth Science Satellite Remote Sensing: Vol. 1: Science and Instruments*. Edited by J. J. Qu, W. Gao, M. Kafatos, R. E. Murphy and V. V. Salomonson, co-published by Tsinghua University Press (Beijing) and Springer-Verlag (Berlin). doi:10.1007/978-3-540-37293-6_5.

Baum, B. A., P. Yang, A. J. Heymsfield, S. Platnick, M. D. King, Y-X. Hu, and S. T. Bedka. 2005b. “Bulk Scattering Properties for the Remote Sensing of Ice Clouds. Part II: Narrowband Models.” *Journal of Applied Meteorology* 44 (12): 1896–1911. doi:10.1175/JAM2309.1.

Baum, B. A., A. J. Heymsfield, P. Yang, and S. T. Bedka. 2005a. “Bulk Scattering Properties for the Remote Sensing of Ice Clouds. Part I: Microphysical Data and Models.” *Journal of Applied Meteorology* 44 (12): 1885–95. doi:10.1175/JAM2308.1.

Belward, A., and T. Loveland. 1996. “The DIS 1km Land Cover Data Set.” *IGBP Global Change Newsletter* 27: 7–9.

Berg, L. K., E. I. Kassianov, C. N. Long, and D. L. Mills. 2011. “Surface Summertime Radiative Forcing by Shallow Cumuli at the Atmospheric Radiation Measurement Southern Great Plains Site.” *Journal of Geophysical Research Atmospheres* 116 (1): 1–13. doi:10.1029/2010JD014593.

Bojanowski, J. S., A. Vrieling, and A. K. Skidmore. 2014. “A Comparison of Data Sources for Creating a Long-Term Time Series of Daily Gridded Solar Radiation for Europe.” *Solar Energy* 99: 152–71. doi:10.1016/j.solener.2013.11.007.

Boucher, O., D. Randall, P. Artaxo, C. Bretherton, G. Feingold, P. Forster, V.-M. Kerminen, Y. Kondo, H. Liao, U. Lohmann, P. Rasch, S.K. Satheesh, S. Sherwood, B. Stevens, and X.Y. Zhang. 2013. “Clouds and Aerosols.” *Climate Change 2013: The Physical Science Basis. Contribution of Working Group I to the Fifth Assessment Report of the Intergovernmental Panel on Climate Change* [Stocker, T.F., D. Qin, G.-K. Plattner, M. Tignor, S.K. Allen, J. Boschung, A. Nauels, Y. Xia, V. Bex and P.M. Midgley (eds.)]. Cambridge, United Kingdom and New York, NY, USA.

Bugliaro, L., T. Zinner, C. Keil, B. Mayer, R. Hollmann, M. Reuter, and W. Thomas. 2011. “Validation of Cloud Property Retrievals with Simulated Satellite Radiances: A Case Study for SEVIRI.” *Atmospheric Chemistry and Physics* 11 (12): 5603–24. doi:10.5194/acp-11-5603-2011.

Calbó, J., D. Pagès, and J.-A. González. 2005. “Empirical Studies of Cloud Effects on UV Radiation: A Review.” *Reviews of Geophysics* 43 (2): 1–28. doi:10.1029/2004RG000155.

Calisto, M., D. Folini, M. Wild, and L. Bengtsson. 2014. “Cloud Radiative Forcing Intercomparison between Fully Coupled CMIP5 Models and CERES Satellite Data.” *Annales Geophysicae* 32 (7): 793–807. doi:10.5194/angeo-32-793-2014.

Cess, R. D., G. L. Potter, J. P. Blanchet, G. J. Boer, S. J. Ghan, J. T. Kiehl, H. Le Treut, Z.-X. Li, X.-Z. Liang, J. F. B. Mitchell, J.-J. Morcretre, D. A. Randall, M. R. Riches, E. Roeckner, U. Schlese, A. Slingo, K. E. Taylor, W. M. Washington, R. T. Wetherald, and I. Yagai. 1989. “Interpretation of Cloud-Climate Feedbacks as

Produced by 14 Atmospheric General Circulation Models." *Science* 245 (4917): 513–16. doi: 10.1126/science.245.4917.513.

Charvát, Z. 2007. "Notes on Calculation of the SEVIRI Band IR3.9 Reflectivity." In Joint 2007 *EUMETSAT Meteorological Satellite Conference and the 15th Satellite Meteorology and Oceanography Conference of the American Meteorological Society*. Amsterdam, Netherlands, EUMETSAT P.50. ISBN 92-9110-079-X.

Chiu, J. C., J. A. Holmes, R. J. Hogan, and E. J. O'Connor. 2014. "The Interdependence of Continental Warm Cloud Properties Derived from Unexploited Solar Background Signals in Ground-Based Lidar Measurements." *Atmospheric Chemistry and Physics* 14 (16): 8389–8401. doi:10.5194/acp-14-8389-2014.

Chiu, J. C., C. H. Huang, A. Marshak, I. Slutsker, D. M. Giles, B. N. Holben, Y. Knyazikhin, and W. J. Wiscombe. 2010. "Cloud Optical Depth Retrievals from the Aerosol Robotic Network (AERONET) Cloud Mode Observations." *Journal of Geophysical Research Atmospheres* 115 (14): 1–12. doi:10.1029/2009JD013121.

Chiu, J. C., A. Marshak, Y. Knyazikhin, W. J. Wiscombe, H. W. Barker, J. C. Barnard, and Y. Luo. 2006. "Remote Sensing of Cloud Properties Using Ground-Based Measurements of Zenith Radiance Source." *Journal of Geophysical Research* 111: D16201. doi:10.1029/2005JD006843.

Chiu, J. C., A. Marshak, W. J. Wiscombe, S. C. Valencia, and E. J. Welton. 2007. "Cloud Optical Depth Retrievals from Solar Background 'signals' of Micropulse Lidars." *IEEE Geoscience and Remote Sensing Letters* 4 (3): 456–60. doi:10.1109/LGRS.2007.896722.

Costa, M. J., E. Cattani, V. Levizzani, and A. M. Silva. 2007. "Cloud Microphysical Properties Retrieval during Intense Biomass Burning Events over Africa and Portugal." In *Measuring Precipitation From Space. Advances In Global Change Research*, edited by V. Levizzani, P. Bauer, and F. J. Turk, 97–111. Springer, Dordrecht. doi:https://doi.org/10.1007/978-1-4020-5835-6_8.

Costa, M. J., R. Salgado, D. Santos, V. Levizzani, D. Bortoli, A. M. Silva, and P. Pinto. 2010. "Modelling of Orographic Precipitation over Iberia: A Springtime Case Study." *Advances in Geosciences* 25: 103–10. doi:10.5194/adgeo-25-103-2010.

Dong, X., B. Xi, and P. Minnis. 2006. "A Climatology of Midlatitude Continental

Clouds from the ARM SGP Central Facility. Part II: Cloud Fraction and Surface Radiative Forcing." *Journal of Climate* 19 (9): 1765–83. doi:10.1175/JCLI3342.1.

EUMETSAT. 2012. "The Conversion from Effective Radiances to Equivalent Brightness Temperatures." Available online at: https://www.eumetsat.int.

Feingold, G., W. L. Eberhard, D. E. Veron, and M. Previdi. 2003. "First Measurements of the Twomey Indirect Effect Using Ground-Based Remote Sensors." *Geophysical Research Letters* 30 (6): 19–22. doi:10.1029/2002GL016633.

Feingold, G., L. A. Remer, J. Ramaprasad, and Y. J. Kaufman. 2001. "Analysis of Smoke Impact on Clouds in Brazilian Biomass Burning Regions: An Extension of Twomey's Approach." *Journal of Geophysical Research: Atmospheres* 106 (D19): 23907–22. doi:10.1029/2001JD000732.

Fung, K. K., and V. Ramaswamy. 1999. "On Shortwave Radiation Absorption in Overcast Atmospheres." *Journal of Geophysical Research* 104 (D18): 22233. doi:10.1029/1999JD900457.

Harrison, E. F., P. Minnis, B. R. Barkstrom, V. Ramanathan, R. D. Cess, and G. G. Gibson. 1990. "Seasonal Variation of Cloud Radiative Forcing Derived from Earth Radiation Budget Experiment." *Journal of Geophysical Research*. doi:10.1029/JD095iD11p18687.

Harrison, L., J. Michalsky, and J. Berndt. 1994. "Automated Multifilter Rotating Shadow-Band Radiometer: An Instrument for Optical Depthand Radiation Measurements." *Applied Optics* 33: 5118–25. doi:10.1364/AO.33.005118.

Holben, B. N., D. Tanre, A. Smirnov, T. F. Eck, I. Slutsker, N. Abuhassan, W. W. Newcomb, et al. 2001. "An Emerging Ground-Based Aerosol Climatology: Aerosol Optical Depth from AERONET." *Journal of Geophysical Research* 106: 12067–12097.

Holben, B.N., T.F. Eck, I. Slutsker, D. Tanré, J.P. Buis, A. Setzer, E. Vermote, J. A. Reagan, Y. J. Kaufman, T. Nakajima, F. Lavenu, I. Jankowiak, and A. Smirnov. 1998. "AERONET—A Federated Instrument Network and Data Archive for Aerosol Characterization." *Remote Sensing of Environment* 66 (1): 1–16. doi:10.1016/S0034-4257(98)00031-5.

Intrieri, J. M., and M. D. Shupe. 2004. "Characteristics and Radiative Effects of

Diamond Dust over the Western Arctic Ocean Region." *Journal of Climate* 17 (15): 2953–60. doi:10.1175/1520-0442(2004)017<2953:CAREOD>2.0.CO;2.

Jolivet, D, and A J Feijt. 2003. "Cloud Thermodynamic Phase and Particle Size Estimation Using the 0.67 and 1.6 µm Channels from Meteorological Satellites." *Atmospheric Chemistry and Physics Discussions* 3: 4461–88. doi: 10.5194/acpd-3-4461-2003.

Kassianov, E., J. Barnard, L. K. Berg, C. N. Long, and C. Flynn. 2011. "Shortwave Spectral Radiative Forcing of Cumulus Clouds from Surface Observations." *Geophysical Research Letters* 38 (7): 1–5. doi:10.1029/2010GL046282.

Kaufman, Y. J., and T. Nakajima. 1993. "Effect of Amazon Smoke on Cloud Microphysics and Albedo - Analysis from Satellite Imagery." *Journal of Applied Meteorology*. doi:10.1175/1520-0450(1993)032<0729:EOASOC>2.0.CO;2.

Kim, B. G., M. A. Miller, S. E. Schwartz, Y. Liu, and Q. Min. 2008. "The Role of Adiabaticity in the Aerosol First Indirect Effect." *Journal of Geophysical Research Atmospheres* 113 (5): 1–13. doi:10.1029/2007JD008961.

King, M., S. Tsay, S. Platnick, M. Wang, and K.-N. Liou. 1997. "Cloud Retrieval Algorithms for MODIS: Optical Thickness, Effective Particle Radius, and Thermodynamic Phase." *MODIS Algorithm Theoretical Basis Document No. ATBD-MOD-05,* MOD06 - Cloud product, versin 5.

Liou, K.N. 1992. *Radiation and Cloud Processes in the Atmosphere, Theory, Observation, and Modeling of Cloud Processes in the Atmosphere*. Oxford Monographs on Geology and Geophysics. Oxford University Press. pp.182-188.

Liu, Y., W. Wu, M. P. Jensen, and T. Toto. 2011. "Relationship between Cloud Radiative Forcing, Cloud Fraction and Cloud Albedo, and New Surface-Based Approach for Determining Cloud Albedo." *Atmospheric Chemistry and Physics* 11 (14): 7155–70. doi:10.5194/acp-11-7155-2011.

Long, C. N., and T. P. Ackerman. 2000. "Identification of Clear Skies from Broadband Pyranometer Measurements and Calculation of Downwelling Shortwave Cloud Effects." *Journal of Geophysical Research* 105 (D12): 15609. doi:10.1029/2000JD900077.

Mace, G. G., S. Benson, K. L. Sonntag, S. Kato, Q. Min, P. Minnis, C. H. Twohy, M.

Poellot, X. Dong, C. Long, Q. Zhang, and D. R. Doelling. 2006. “Cloud Radiative Forcing at the Atmospheric Radiation Measurement Program Climate Research Facility: 1. Technique, Validation, and Comparison to Satellite-Derived Diagnostic Quantities.” *Journal of Geophysical Research Atmospheres* 111 (11): 1–28. doi:10.1029/2005JD005921.

Martin, G. M., D. W. Johnson, and A. Spice. 1994. “The Measurement and Parameterization of Effective Radius of Droplets in Warm Stratocumulus Clouds.” *Journal of the Atmospheric Sciences*. doi:10.1175/1520-0469(1994)051<1823:TMAPOE>2.0.CO;2.

Mateos, D., M. Antón, A. Valenzuela, A. Cazorla, F. J. Olmo, and L. Alados-Arboledas. 2014a. “Efficiency of Clouds on Shortwave Radiation Using Experimental Data.” *Applied Energy* 113: 1216–19. doi:10.1016/j.apenergy.2013.08.060.

Mateos, D., G. Pace, D. Meloni, J. Bilbao, A. di Sarra, A. de Miguel, G. Casasanta, and Q. Min. 2014b. “Observed Influence of Liquid Cloud Microphysical Properties on Ultraviolet Surface Radiation.” *Journal of Geophysical Research Atmospheres* 119: 2429–40. doi:10.1002/2013JD020309.

Mateos, D., M. Antón, A. Valenzuela, A. Cazorla, F. J. Olmo, and L. Alados-Arboledas. 2013. “Short-Wave Radiative Forcing at the Surface for Cloudy Systems at a Midlatitude Site.” *Tellus, Series B: Chemical and Physical Meteorology* 65 (1): 1–12. doi:10.3402/tellusb.v65i0.21069.

Mayer, B., and A. Kylling. 2005. “Technical Note: The libRadtran Software Package for Radiative Transfer Calculations – Description and Examples of Use.” *Atmospheric Chemistry and Physics Discussions* 5 (2): 1319–81. doi:10.5194/acpd-5-1319-2005.

McBride, P. J., K. S. Schmidt, P. Pilewskie, A. S. Kittelman, and D. E. Wolfe. 2011. “A Spectral Method for Retrieving Cloud Optical Thickness and Effective Radius from Surface-Based Transmittance Measurements.” *Atmospheric Chemistry and Physics Discussions* 11: 1053 – 1041. doi: 10.5194/acpd-11-1053-2011.

McClatchey, R. A., W. Fenn, J. E. A. Selby, F. E. Volz, and J. S. Garing. 1971. “Optical Properties of the Atmosphere.” *Environ. Res. Papers, 354, Air Force Cambridge Research Laboratories*. L. G. Hanscom Field, Bedford, Massachusetts.

McComiskey, A., G. Feingold, A. S. Frisch, D. D. Turner, M. A. Miller, J. C. Chiu, Q. Min, and J. A. Ogren. 2009. "An Assessment of Aerosol-Cloud Interactions in Marine Stratus Clouds Based on Surface Remote Sensing." *Journal of Geophysical Research Atmospheres* 114 (9): 1–15. doi:10.1029/2008JD011006.

Meirink, J. F. 2013. "Algorithm Theoretical Basis Document, Cloud Physical Products, SEVIRI." EUMETSAT Satellite Application Facility on Climate Monitoring. Available online at: www.cmsaf.eu. doi: 10.5676/EUMETSAT_SAF_CM/CLAAS/V001.

Menzel, W. P., R. Frey, and B. Baum. 2010. "Cloud Top Properties and Cloud Phase Algorithm Theoretical Basis Document." Products: 06_L2 (CT), 2010.

Min, Q., and L. C. Harrison. 1996. "Cloud Properties Derived from Surface MFRSR Measurements and Comparison with GOES Results at ARM SGP Site." *Geophysical Research Letters* 23 (13): 1641–44.

Min, Q., E. Joseph, Y. Lin, L. Min, B. Yin, P. H. Daum, L. I. Kleinman, J. Wang, and Y. N. Lee. 2012. "Comparison of MODIS Cloud Microphysical Properties with in-Situ Measurements over the Southeast Pacific." *Atmospheric Chemistry and Physics* 12 (23): 11261–73. doi:10.5194/acp-12-11261-2012.

Min, Q., E. Joseph, and M. Duan. 2004. "Retrievals of Thin Cloud Optical Depth from a Multifilter Rotating Shadowband Radiometer." *Journal of Geophysical Research* 109 (D2): D02201. doi:10.1029/2003JD003964.

Myhre, G., D. Shindell, F.-M. Bréon, W. Collins, J. Fuglestvedt, J. Huang, D. Koch, J.-F. Lamarque, D. Lee, B. Mendoza, T. Nakajima, A. Robock, G. Stephens, T. Takemura and H. Zhang. 2013. "Anthropogenic and Natural Radiative Forcing." *Climate Change 2013: The Physical Science Basis. Contribution of Working Group I to the Fifth Assessment Report of the Intergovernmental Panel on Climate Change*, [Stocker, T.F., D. Qin, G.-K. Plattner, M. Tignor, S.K. Allen, J. Boschung, A. Nauels, Y. Xia, V. Bex and P.M. Midgley (eds.)]. Cambridge University Press, Cambridge, United Kingdom and New York, NY, USA.

Nakajima, T. Y., and T. Nakajma. 1995. "Wide-Area Determination of Cloud Microphysical Properties from NOAA AVHRR Measurements for FIRE and ASTEX Regions." *Journal of the Atmospheric Sciences*. doi:10.1175/1520-

0469(1995)052<4043:WADOCM>2.0.CO;2.

Nakajima, T., and M. D. King. 1990. “Determination of the Optical Thickness and Effective Particle Radius of Clouds from Reflected Solar Radiation Measurements. Part I: Theory.” *Journal of the Atmospheric Sciences*. doi:10.1175/1520-0469(1990)047<1878:DOTOTA>2.0.CO;2.

Oreopoulos, L., and W. B. Rossow. 2011. “The Cloud Radiative Effects of International Satellite Cloud Climatology Project Weather States.” *Journal of Geophysical Research Atmospheres* 116 (12): 1–22. doi:10.1029/2010JD015472.

Painemal, D., J. C. Chiu, P. Minnis, C. Yost, X. Zhou, M. Cadeddu, E. Eloranta, E. R. Lewis, R. Ferrare, and P. Kollias. 2017. “Aerosol and Cloud Microphysics Covariability in the Northeast Pacific Boundary Layer Estimated with Ship-Based and Satellite Remote Sensing Observations.” *Journal of Geophysical Research: Atmospheres* 122 (4): 2403–18. doi:10.1002/2016JD025771.

Painemal, D., P. Minnis, and M. Nordeen. 2015. “Aerosol Variability, Synoptic-Scale Processes, and Their Link to the Cloud Microphysics over the Northeast Pacific during MAGIC.” *Journal of Geophysical Research Atmospheres* 120: 5122–39. doi:10.1002/2015JD023175.

Painemal, D., and P. Zuidema. 2011. “Assessment of MODIS Cloud Effective Radius and Optical Thickness Retrievals over the Southeast Pacific with VOCALS-REx in Situ Measurements.” *Journal of Geophysical Research Atmospheres* 116 (24): 1–16. doi:10.1029/2011JD016155.

Painemal, D., and P. Zuidema. 2013. “The First Aerosol Indirect Effect Quantified through Airborne Remote Sensing during VOCALS-REx.” *Atmospheric Chemistry and Physics* 13 (2): 917–31. doi:10.5194/acp-13-917-2013.

Piedehierro, A. A., M. Antón, A. Cazorla, L. Alados-Arboledas, and F. J. Olmo. 2014. “Evaluation of Enhancement Events of Total Solar Irradiance during Cloudy Conditions at Granada (Southeastern Spain).” *Atmospheric Research* 135–136:1–7. doi:10.1016/j.atmosres.2013.08.008.

Pierluissi, J. H., and G.-S. Peng. 1985. “New Molecular Transmission Band Models for LOWTRAN.” *Optical Engineering* 24: 541–47. doi:10.1117/12.7973523.

Pyrina, M., N. Hatzianastassiou, C. Matsoukas, A. Fotiadi, C. D. Papadimas, K. G.

Pavlakis, and I. Vardavas. 2015. “Cloud Effects on the Solar and Thermal Radiation Budgets of the Mediterranean Basin.” *Atmospheric Research* 152: 14–28. doi:10.1016/j.atmosres.2013.11.009.

Raes, F., T. Bates, F. McGovern, and M. van Liedekerke. 2000. “The Second Aerosol Characterization Experiment (ACE 2): General Overview and Main Results.” *Tellus* 52B: 111–25. doi:10.1034/j.1600-0889.2000.00124.x.

Ramanathan, V., R. D. Cess, E. F. Harrison, P. Minnis, B. R. Barkstrom, E. Ahmad, and D. Hartmann. 1989. “Cloud-Radiative Forcing and Climate: Results from the Earth Radiation Budget Experiment.” *Science* 243 (4887): 57–63. doi:10.1126/science.243.4887.57.

Rémillard, J., P. Kollias, E. Luke, and R. Wood. 2012. “Marine Boundary Layer Cloud Observations in the Azores.” *Journal of Climate* 25 (21): 7381–98. doi:10.1175/JCLI-D-11-00610.1.

Ricchiazzi, P., S. Yang, C. Gautier, and D. Sowle. 1998. “SBDART: A Research and Teaching Software Tool for Plane-Parallel Radiative Transfer in the Earth’s Atmosphere.” *Bulletin of the American Meteorological Society* 79: 2101–2114. doi:10.1175/1520-0477(1998)079<2101:SARATS>2.0.CO;2.

Roebeling, R. A., A. J. Feijt, and P. Stammes. 2006. “Cloud Property Retrievals for Climate Monitoring: Implications of Differences between Spinning Enhanced Visible and Infrared Imager (SEVIRI) on METEOSAT-8 and Advanced Very High Resolution Radiometer (AVHRR) on NOAA-17.” *Journal of Geophysical Research Atmospheres* 111 (20): 1–16. doi:10.1029/2005JD006990.

Rose, T., S. Crewell, U. Lohnert, and C. Simmer. 2005. “A Network Suitable Microwave Radiometer for Operational Monitoring of the Cloudy Atmosphere.” *Atmospheric Research* 75: 183–200. doi:10.1016/j.atmosres.2004.12.005.

Rosenfeld, D., E. Cattani, S. Melani, and V. Levizzani. 2004. “Considerations on Daylight Operation of 1.6-versus 3.7μm Channel on NOAA and METOP Satellites.” *Bulletin of the American Meteorological Society* 85 (6): 873–81. doi:10.1175/BAMS-85-6-873.

Salgueiro, V., M. J. Costa, A. M. Silva, and D. Bortoli. 2014. “Variability of the Daily-Mean Shortwave Cloud Radiative Forcing at the Surface at a Midlatitude Site in

Southwestern Europe." *Journal of Climate* 27 (20): 7769–80. doi:10.1175/JCLI-D-13-00696.1.

Salgueiro, V., M. J. Costa, A. M. Silva, and D. Bortoli. 2016. "Effects of Clouds on the Surface Shortwave Radiation at a Rural Inland Mid-Latitude Site." *Atmospheric Research* 178–179. Elsevier B.V.: 95–101. doi:10.1016/j.atmosres.2016.03.020.

Salgueiro, V., M. J. Costa, A. M. Silva, C. Lanconelli, and D. Bortoli. 2017. "Cloud Parameter Retrievals from Meteosat and Their Effects on the Shortwave Radiation at the Surface." *International Journal of Remote Sensing* 38 (4). Taylor & Francis: 1137–61. doi:10.1080/01431161.2017.1280630.

Salgueiro, V. 2011. "Simulações de Transferência Radiativa Em Atmosferas Com Nuvens: Comparação Entre Diferentes Aproximações." Tese de Mestrado, Universidade de Évora. pp. 1-92.

Santos, D., M. J. Costa, and A. M. Silva. 2008. "Direct SW Aerosol Radiative Forcing over Portugal." *Atmospheric Chemistry and Physics* 8 (19): 5771–86. doi: 10.5194/acp-8-5771-2008.

Santos, D., M. J. Costa, A. M. Silva, and R. Salgado. 2013. "Modeling Saharan Desert Dust Radiative Effects on Clouds." *Atmospheric Research* 127: 178–94. doi:10.1016/j.atmosres.2012.09.024.

Sarna, K., and H. W. J. Russchenberg. 2016. "Ground-Based Remote Sensing Scheme for Monitoring Aerosol-Cloud Interactions." *Atmospheric Measurement Techniques* 9 (3): 1039–50. doi:10.5194/amt-9-1039-2016.

Schiffer, R.A., and W.B. Rossow. 1983. "The International Satellite Cloud Climatology Project (ISCCP) - The First Project of the World Climate Research Programme." *Bulletin of the American Meteorological Society* 64 (7): 779–84. doi:10.1175/1520-0477(1991)072<0002:ICDP>2.0.CO;2.

Schmetz, J., P. Pili, S. Tjemkes, D. Just, J. Kerkmann, S. Rota, and A. Ratier. 2002. "An Introduction to Meteosat Second Generation (MSG)." *Bulletin of the American Meteorological Society* 83 (7): 977–92. doi:10.1175/1520-0477(2002)083<0977:AITMSG>2.3.CO;2.

Schulz, J., P. Albert, H.-D. Behr, D. Caprion, H. Deneke, S. Dewitte, B. Dürr, P.Fuchs, A.Gratzki, P. Hechler, R. Hollmann, S. Johnston, K.-G. Karlsson, T. Manninen,

R.Muller, M.Reuter, A.Riihela, R. Roebeling, N. Selbach, A. Tetzlaff, W. Thomas, M. Werscheck, E. Wolters, and A. Zelenka. 2009. "Operational Climate Monitoring from Space: The EUMETSAT Satellite Application Facility on Climate Monitoring (CM-SAF)." *Atmospheric Chemistry and Physics* 9: 1687-1709.

Sengupta, M., E. E. Clothiaux, and T. P. Ackerman. 2004. "Climatology of Warm Boundary Layer Clouds at the ARM SGP Site and Their Comparison to Models." *Journal of Climate* 17 (24): 4760–82. doi:10.1175/JCLI-3231.1.

Shettle, E. P. 1989. "Models of Aerosols, Clouds and Precipitation for Atmospheric Propagation Studies." In *Proc. AGARD Conf. CP No. 454, Atmospheric Propagation in the UV, Visible, IR and Mm-Wave Region and Related System Aspects*. Copenhagen, Denmark: Advisory Group for Aerospace Research and Development.

Shupe, M. D., J. S. Daniel, G. de Boer, E. W. Eloranta, P.s Kollias, C. N. Long, E. P. Luke, D. D. Turner, and J. Verlinde. 2008. "A Focus on Mixed-Phase Clouds." *Bulletin of the American Meteorological Society* 89 (10): 1549–62. doi:10.1175/2008BAMS2378.1.

Silva, A. M., M. L. Bugalho, M. J. Costa, W. Von Hoyningen-Huene, T. Schmidt, J. Heintzenberg, and S. Henning. 2002. "Aerosol Optical Properties from Columnar Data during the Second Aerosol Characterization Experiment on the South Coast of Portugal." *Journal of Geophysical Research Atmospheres* 107 (22): 1–11. doi:10.1029/2002JD002196.

Song, K., and S. S. Yum. 2012. "Anthropogenic Radiative Forcing of Marine Stratocumulus Clouds under Different Thermodynamic Conditions-An LES Model Study." *Atmospheric Research* 118: 370–89. doi:10.1016/j.atmosres.2012.07.018.

Stamnes, K., S.-C. Tsay, W. Wiscombe, and I. Laszlo. 2000. "DISORT a General-Purpose Fortran Program for Discrete-Ordinate Method Radiative Transfer in Scattering and Emitting Layered Media: Documentation of Methodology." NASA Tech. Rep., 112 pp.

Stengel, M. S., A. K. Kniffka, J. F. M. Meirink, M. L. Lockhoff, J. T. Tan, and R. H. Hollmann. 2014. "CLAAS: The CM SAF Cloud Property Data Set Using

SEVIRI." *Atmospheric Chemistry and Physics* 14 (8): 4297–4311. doi:10.5194/acp-14-4297-2014.

Stephens, G. L. 1978. "Radiation Profiles in Extended Water Clouds. II: Parameterization Schemes." *Journal of the Atmospheric Sciences* 35: 2123–2132. doi:10.1175/1520-0469(1978)035<2123: RPIEWC>2.0.CO;2.

Twomey, S. 1974. "Pollution and the Planetary Albedo." *Atmospheric Environment* 8: 1251–56.

Twomey, S. 1977. "The Influence of Pollution on the Shortwave Albedo of Clouds." *Journal of the Atmospheric Sciences*. 34(7): 1149-52. doi:10.1175/1520-0469(1977)034<1149:TIOPOT>2.0.CO;2.

Wacker, S., J. Gröbner, D. Nowak, L. Vuilleumier, and N. Kämpfer. 2011. "Cloud Effect of Persistent Stratus Nebulosus at the Payerne BSRN Site." *Atmospheric Research* 102 (1–2): 1–9. doi:10.1016/j.atmosres.2011.06.007.

Wood, R., C. R. Mechoso, C. S. Bretherton, R. A. Weller, B. Huebert, F. Straneo, B. A. Albrecht, R. H. Coe, G. Allen, G. Vaughan, P. Daum, C. Fairall, D. Chand, L. Gallardo Klenner, R. Garreaud, C. Grados, D. S. Covert, T. S. Bates, R. Krejci, L. M. Russell, S. de Szoeke, A. Brewer, S.E. Yuter, S. R. Springston, A. Chaigneau, T. Toniazzo, P. Minnis, R. Palikonda, S.J. Abel, W. O. J. Brown, S.Williams, J. Fochesatto, J. Brioude, and K. N. Bower. 2011. "The VAMOS Ocean-Cloud-Atmosphere-Land Study Regional Experiment (VOCALS-REx): Goals, Platforms, and Field Operations." *Atmospheric Chemistry and Physics* 11 (2): 627–54. doi:10.5194/acp-11-627-2011.

Wood, R., M. Wyant, C. S. Bretherton, J. Rémillard, P. Kollias, J. Fletcher, J. Stemmler, S. De Szoeke, S. Yuter, M. Miller, D. Mechem, G. Tselioudis, J. C. Chiu, J. Mann, E. J. O'Connor, R. J. Hogan, X. Dong, M. Miller, V. Ghate, A. Jefferson, Q. Min, P. Minnis, R. Palikonda, B. Albrecht, E. Luke, C. Hannay, Y. Lin. 2015. "Clouds, Aerosols, and Precipitation in the Marine Boundary Layer: An Arm Mobile Facility Deployment." *Bulletin of the American Meteorological Society* 96 (3): 419–39. doi:10.1175/BAMS-D-13-00180.1.

Wood, R., and D, L. Hartmann. 2006. "Spatial Variability of Liquid Water Path in Marine Low Cloud: The Importance of Mesoscale Cellular Convection." *Journal*

of Climate 19 (9): 1748–64. doi:10.1175/JCLI3702.1.

Zeng, S., C. Cornet, F. Parol, J. Riedi, and F. Thieuleux. 2012. "A Better Understanding of Cloud Optical Thickness Derived from the Passive Sensors MODIS/AQUA and POLDER/PARASOL in the A-Train Constellation." *Atmospheric Chemistry and Physics* 12 (23): 11245–59. doi:10.5194/acp-12-11245-2012.

Zhang, Z., and S. Platnick. 2011. "An Assessment of Differences between Cloud Effective Particle Radius Retrievals for Marine Water Clouds from Three MODIS Spectral Bands." *Journal of Geophysical Research Atmospheres* 116 (20): 1–19. doi:10.1029/2011JD016216.

UNIVERSIDADE DE ÉVORA
INSTITUTO DE INVESTIGAÇÃO
E FORMAÇÃO AVANÇADA

Contactos:

Universidade de Évora

Instituto de Investigação e Formação Avançada - IIFA

Palácio do Vimioso | Largo Marquês de Marialva, Apart. 94

7002-554 Évora | Portugal

Tel: (+351) 266 706 581

Fax: (+351) 266 744 677